ABSTRACT

Title of Document:	MAPPING PREFERENTIAL FLOW PATHWAYS IN A RIPARIAN WETLAND USING GROUND-PENETRATING RADAR
	Kevin Hill Gormally, PhD, 2009
Directed By:	Professor Marla McIntosh, Plant Science and Landscape Architecture

Preferential flow of water through channels in the soil has been implicated as a vehicle for groundwater and surface water contamination in forested riparian wetland buffers. Water conducted through these by-pass channels can circumvent interaction with wetland biota, biomass, and soils, thereby reducing the buffering capacity of the riparian strips for adsorption and uptake of excess nutrient loads from neighboring agricultural fields and urbanized lands. Models of riparian function need to account for preferential flow to accurately estimate nutrient flux to stream channels, but there are currently no methods for determining the form and prevalence of these pathways outside of extensive destructive sampling.

This research developed, tested, and validated a new application of non-invasive ground-penetrating radar technology (GPR) for mapping the three-dimensional structure of near-surface (0-1 m) lateral preferential flow channels. Manual and automated detection methodologies were created for analyzing GPR scan data to locate the channels

in the subsurface. The accuracy of the methodologies was assessed in two field test plots with buried PVC pipes simulating the riparian channels. The manual methodology had a 0% Type I error rate and 8% Type II error rate; the automated version had a <1% Type I error rate and 29% Type II error rate. An automated mapping algorithm was also created to reconstruct channel geometries from the scan data detections. The algorithm was shown to robustly track the connectivity of PVC pipe segments arranged in a branching structure hypothesized to exist in the riparian soils. These methods and algorithms were then applied at a riparian wetland study site at USDA Beltsville Agricultural Research Center in Beltsville, MD. The predicted structure of preferential flow channels in the wetland was validated by transmission of tracer dye through the study site and ground truth generated from soil core samples (92% accurate).

These GPR tools will enable researchers to efficiently and effectively characterize lateral preferential flow without negatively impacting environmentally sensitive wetland areas. Scientists can now directly study these flow mechanisms to investigate the effects of by-pass pathways on nutrient fate in riparian buffers and the interactions of preferential flow with plant and animal systems.

MAPPING PREFERENTIAL FLOW PATHWAYS IN A RIPARIAN WETLAND USING GROUND-PENETRATING RADAR

By

Kevin Hill Gormally

Dissertation submitted to the Faculty of the Graduate School of the
University of Maryland, College Park, in partial fulfillment
of the requirements for the degree of
Doctor of Philosophy
2009

Advisory Committee:
Professor Marla McIntosh, Chair
Associate Professor Patrick Kangas
Dr. Gregory McCarty
Dr. Anthony Mucciardi
Associate Professor Joseph Sullivan
Professor Claire Welty

© Copyright by
Kevin Hill Gormally
2009

Dedication

To my mom, dad, sister, and the Hill and Gormally families.

Acknowledgements

This work would not have been possible without the time and energy devoted to it by my committee. Thanks go to Dr. Marla McIntosh and Dr. Anthony Mucciardi for connecting the dots between science and engineering and for supporting and challenging me to do the same; all students should be so lucky to have mentors with their vision, enthusiasm, and endless supplies of red ink; to Dr. Gregory McCarty, Dr. David Tilley, and Dr. Claire Welty for lending their considerable expertise to this interdisciplinary study; and to Dr. Patrick Kangas and Dr. Joseph Sullivan for graciously agreeing to join the defense committee at the last minute and gamely assessing the technological and ecological implications of my research.

Thanks also to Dr. Jonathon Angier and Dr. Megan Lang for their help at OPE^3, and to my employers at the Johns Hopkins University Applied Physics Laboratory for their financial support.

Finally, thanks to my dad for being the true home depot of tools I needed to overcome obstacles encountered in the field and to my mom for surviving the equations and proof reading this paper. They were and are my inspiration.

Table of Contents

List of Tables

List of Figures

Chapter 1: Introduction

1.1 Problem Statement

Riparian wetlands are complex ecosystems that can buffer waterways from the contaminated runoff of neighboring agricultural fields and urbanized lands. Environmental regulations mandate the creation and preservation of riparian areas in the Chesapeake Bay watershed (Alliance for the Chesapeake Bay, 2004) because of their capacity to reduce surface runoff, bind pollutants to the soil, and remove nutrients through plant uptake.

Recent research, however, has suggested that the riparian buffering capability can be subverted by preferential flow of water through the riparian soils (Angier et al., 2005; Bohlke et al., 2007). Preferential flow is the non-uniform and often rapid movement of water and its constituents. Elemental adsorption and uptake are reduced when water is preferentially conducted in by-pass channels, increasing the likelihood of groundwater and surface water contamination.

Vertical preferential flow of water into the soil has been studied and its effects have been quantified in the field and modeled in laboratory experiments (Morris and Mooney, 2004; Nobles et al., 2004; Pierret et al., 2002b; Weiler, 2005). Conversely, the form, prevalence, and impact of lateral preferential flow through channels, also known as macropores and soil pipes, are still largely unresolved (Weiler et al., 2003) despite recent intense research scrutiny (Angier et al., 2005; Holden, 2005; Sidle et al., 2001).

This knowledge gap poses a critical hurdle to understanding the nitrogen and phosphorous loads entering the headwater streams of the Chesapeake Bay drainage area. Research tools are needed to determine the density and structure of the by-pass channels in buffer areas so that these measurements can be integrated into models of riparian hydrology and contaminant fate (Lin et al., 1999; Vogel and Roth, 2003).

1.2 Research Objective

This dissertation research fits within a broader effort to understand the behaviors of mid-Atlantic riparian wetland groundwater and determine delivery mechanisms of nitrate and phosphorous from agricultural uplands to stream channels.

The research culminated at a riparian area in the USDA Beltsville Agricultural Research Center (USDA/ARS BARC) north of Washington, D.C. in Beltsville, MD. The Optimizing Production Inputs for Economic and Environmental Enhancement (OPE^3) research site is located in an agricultural watershed with a first order riparian stream that has been continuously monitored for several ongoing environmental studies (Angier et al., 2002; Gish et al., 2005). Further description of the site will be presented in Chapter 5.

Researchers have proposed two alternatives for conceptual models of the groundwater flow through the OPE^3 riparian buffer (Angier and McCarty, 2008). The first is a traditional model commonly cited in riparian denitrification studies (Fig. 1 a). It posits that waters infiltrate the upland agricultural soils, travel laterally and fairly uniformly through the matrix, and are discharged into the stream channel after long residence times.

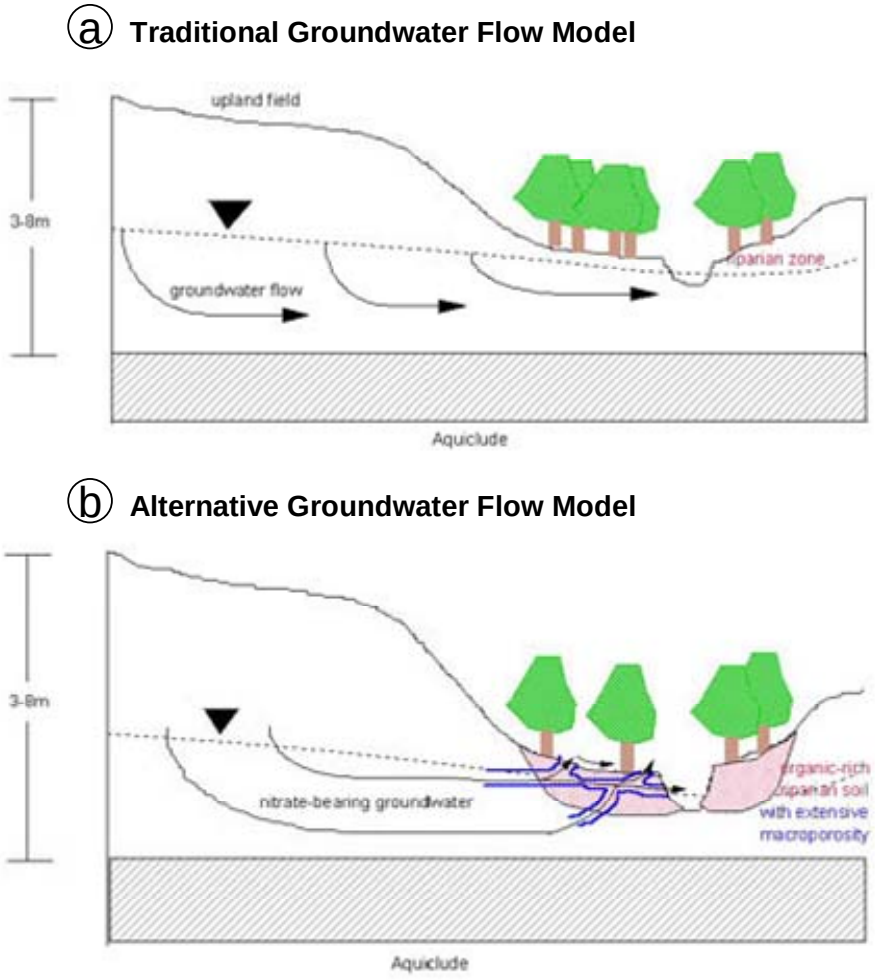

Figure 1. Traditional and alternative groundwater flow models governing transport of contaminants from adjacent agricultural fields through the OPE^3 riparian buffer (Angier and McCarty, 2008).

The researchers assert that this model is oversimplified and leads to the errant assumption that riparian biogeochemical conditions predominantly regulate denitrification processes (Angier and McCarty, 2008).

An alternative conceptual model (Fig. 1 b) incorporates preferential flow of water through the wetland to account for large nutrient fluxes to the stream channel that are not explained by the traditional model. It posits that by-pass mechanisms allow much of the groundwater to move rapidly through a relatively small volume of matrix, reducing denitrification rates (Angier and McCarty, 2008). This model is bolstered by indirect and direct evidence of preferential flow in OPE^3 (Angier et al., 2005), but the locations and extent of the flow channels are unknown.

The primary purpose of this research was to develop procedures and tools for mapping lateral preferential flow channels using ground-penetrating radar (GPR) technology. Manual and automated field GPR detection methods were defined for locating preferential flow channels and a process was created to map the three-dimensional structure of the channels based on the detections. These procedures were developed in field test plots with buried pipes simulating preferential flow channels and then validated at a study site in OPE^3. The resulting procedures and tools can be used to refine the alternative conceptual groundwater flow model and enhance the understanding of contaminant fate in mid-Atlantic riparian wetlands.

1.3 Description of Experiments

A series of experiments was conducted to develop, test, and validate procedures for detecting and mapping preferential flow channels in a riparian wetland using GPR. The three experiments are pictured with their layouts in Fig. 2.

In Experiment I, a field test plot was created to develop generalized methods for detecting channel-like objects. Sixteen PVC pipes simulating channels with different sizes and fill media were buried in four parallel rows (Fig. 2 a). Manual and automated detection methods were applied to locate the pipes from radar scan data collected at different orientations with respect to the plot layout.

In Experiment II, a field test plot was created to test the detection methodologies from Experiment I and to develop an algorithm for connecting the resulting detections into a three-dimensional prediction of the buried objects' geometries (Fig. 2 b). A nearest neighbor mapping algorithm was used to construct the three-dimensional shape of a connected PVC pipe structure simulating branching preferential flow channels.

In Experiment III, the methods and algorithms developed in Experiments I and II were applied at an experimental study site in the OPE^3 riparian wetland to detect and map preferential flow channels (Fig. 2 c). Predicted flow channel locations between 15 cm and 65 cm in depth were ground truthed using observation of preferential tracer dye transmission through the study site and evaluation of soil core samples.

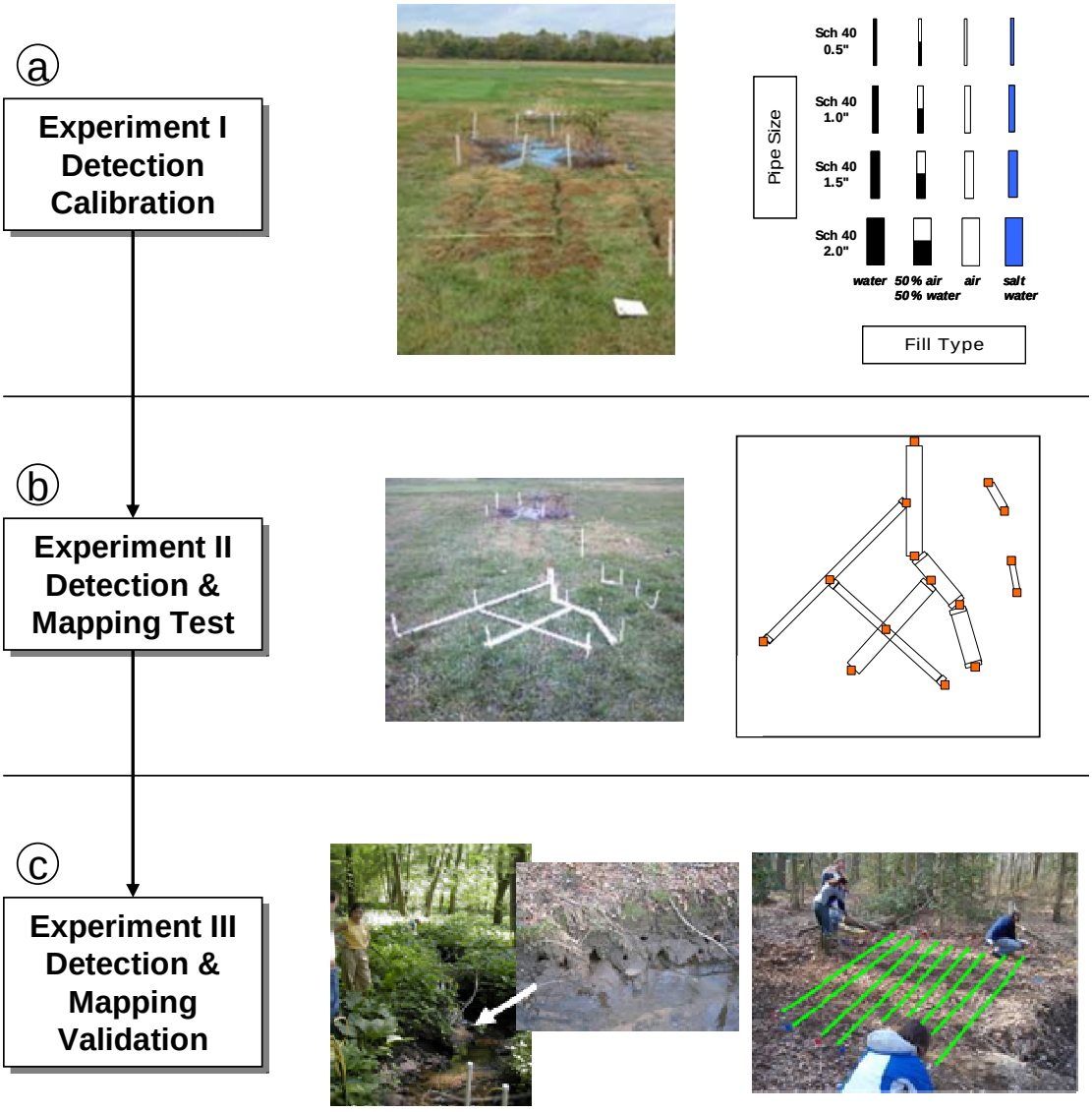

Figure 2. Experiments to (a) develop, (b) test, and (c) validate a GPR methodology for mapping preferential flow channels in a riparian wetland buffer.

1.4 Literature Review

1.4.1 Riparian Wetland Forest Nutrient Cycling and Hydrology

Riparian ecosystems can reduce nitrate loading from human sources to surface and ground waters because of their ability to influence nutrient cycles. The prevailing paradigm is that contaminant concentrations are reduced because: (1) deep-rooting woody vegetation act as nutrient sinks; (2) above-ground biomass slows runoff and increases sedimentation rates; and (3) the oxidation/reduction potential of the wetland soil results in denitrification. Furthermore, biota feedbacks to the ecosystem hydrology and physiochemistry increases nutrient cycling along with species richness, primary productivity, and organic matter accumulation rates (Lowrance et al., 1984; Mitsch and Gosselink, 2000; Naiman and Décamps, 1997; Peterjohn and Correll, 1984).

Buffering capacity can vary, however, depending on the riparian soil structure and the hydrologic flow pathways through the buffer (Angier et al., 2005). A meta-analysis showed that buffer width is an important factor but not the sole determinant of nitrogen removal. Soil type, subsurface biogeochemistry, and subsurface hydrology (including groundwater flow paths) also influence nutrient cycling rates (Mayer et al., 2007).

Water moves through a riparian area along a wide range of different flow pathways (Fig. 3). Discharge to a stream channel is generated from water running along the ground surface (overland flow) and infiltrating the ground and moving through the soil matrix (throughflow, interflow, and groundwater flow).

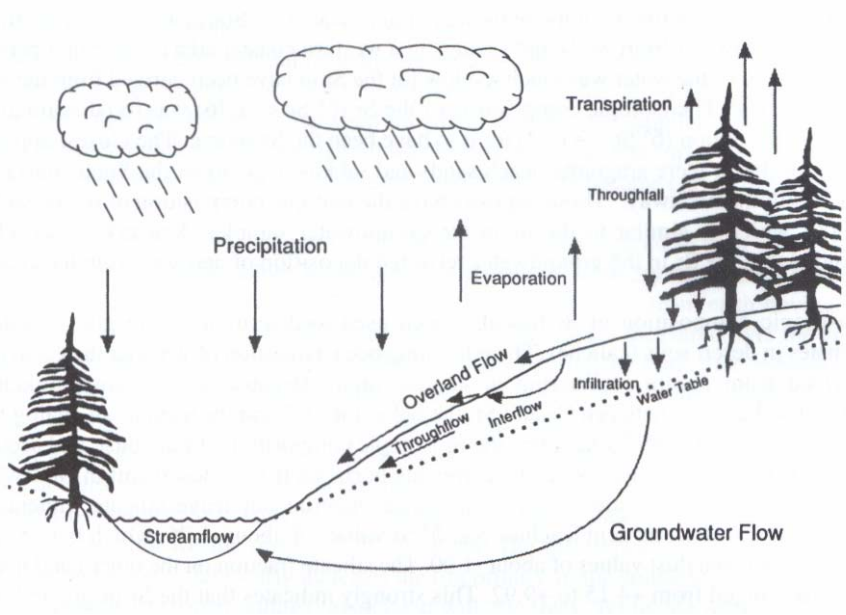

Figure 3. Components of the hydrologic cycle through a catchment (Kendall and McDonnell, 1998).

The flow rate of water moving through the ground is determined by the size and interconnectedness of the pores in the matrix. Macropores (Fig. 4), openings in the matrix larger than 3 mm (Germann and Beven, 1981), can form preferential flow channels with rapid flow rates. These openings vary from fractures to wormholes, fauna tunnels, voids from decayed roots, and soil pipes.

Preferential flow was first described by J.B. Lawes, J.H. Gilbert, and R. Warington (1882). The authors distinguished between preferential and matrix flows during field drainage experiments. Preferential flow was characterized by regions of enhanced flux where only a small fraction of the soil was involved with most of the flow. Conversely, matrix flow was characterized by relatively slow and even movement of water and solutes.

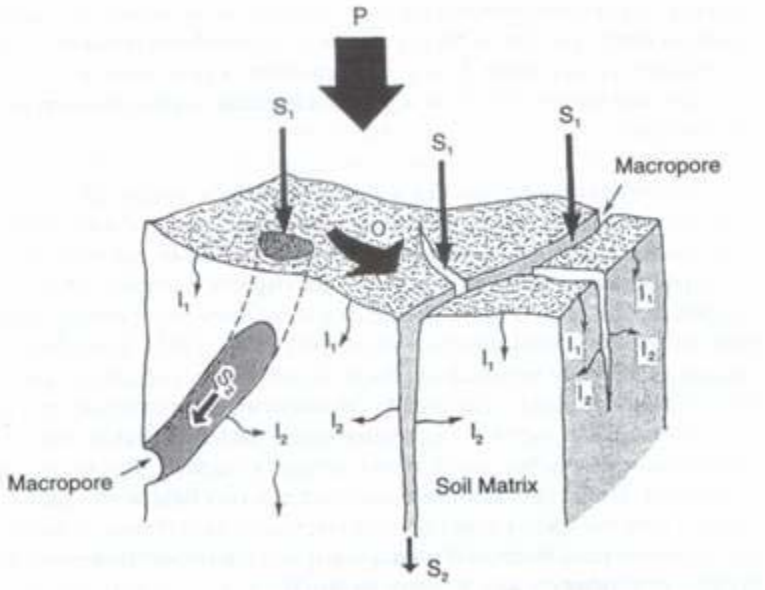

Figure 4. Schematic of flow in soil containing macropores: water inputs (P), overland flow (O), micropore infiltration (I_1, I_2), and macropore infiltration (S_1) and flow (S_2) (Kendall and McDonnell, 1998).

The relative distribution of water flowing through matrix and preferential pathways is a critical factor in the rate and amount of nitrate delivered to stream channels because it can contribute a disproportionately substantial percentage of the water transmitted through the watershed (Angier et al., 2005; Bohlke et al., 2007). Holden and Burt (2002) reported that as much as 30 percent of streamflow in a catchment in England, and 10 percent on average, was generated through preferential pathways.

1.4.2 Ground-Penetrating Radar

GPR is the general term for non-invasive sensing technologies that employ electromagnetic radiation to detect targets in the ground. A GPR antenna sends an electromagnetic pulse, typically in the 50 to 1500 MHz frequency range, through the

earth and senses reflections of that energy off of discontinuities in the medium. It can be performed from the ground surface, under the surface from a borehole, or far above the ground from aircraft.

Interpretation of GPR scan data yields information about objects buried in the earth as well as characteristics of the soil itself, such as the density and water content. The ability to detect a given subsurface target depends upon the electrical and magnetic contrast between the target and the surrounding media, and the target's geometric orientation with respect to the antenna (Daniels, 2004). A comprehensive introduction to the technology is given in Chapter 2.

GPR was first used in 1929 to determine the depth of a glacier in Austria (Olhoeft, 1996). The technology was rediscovered in the 1960s and numerous additional applications were developed, from mapping soil structures to detecting buried utilities and directing archaeological excavations (Annan, 2001; Conyers, 2004; Daniels, 2004).

Two recent studies (Gish et al., 2005; Holden et al., 2002) have shown that GPR can be used to successfully detect preferential flow structures. Gish et al. (2005) used GPR to predict the subsurface topography of a clay lens preferential flow structure underlying the agricultural fields in OPE^3. The depth of the clay layer was mapped from scans recorded with a low frequency sensor (150 MHz). These measurements were combined with digital elevation maps of the surface to identify potential locations of the flow pathways. A network of soil moisture probes independently verified that these layers act as subsurface water conveyances. This experimental design provides a model for ground truthing the results of a GPR

analysis, but the target detection methodology is not directly transferable for wetland channels.

Holden et al. (2002) detected soil pipes greater than 10 cm in diameter on hill slopes and peat lands using 100 and 200 MHz GPR sensors. The researchers scanned known locations of pipes from previous manual surveys and determined which of those targets were observed in the scan data. This study showed that GPR energy does reflect off of preferential flow channels but does not provide a generalized methodology for detecting them without *a priori* knowledge of their locations or a process for mapping their geometries.

1.4.2.1 Subsurface Target Detection

Many studies have shown that buried pipes and pipe-like targets can be located using GPR technology. Methods have been described for detecting utilities and pipes (Allred et al., 2004; Park et al., 2003; Zarkhidze and Lemenager, 2004) as well as tree roots (Barton and Montagu, 2004; Butnor et al., 2001; Cox et al., 2005; Hruska and Cermak, 1999; Stover et al., 2007) within 1 m of the soil surface using high frequency antennae (400 – 1500 MHz). These methods provide a basis for the definition of a manual target detection methodology.

Designing a computer algorithm to automatically detect targets using GPR is a more difficult challenge, one that has been the subject of many studies by researchers in engineering disciplines. Various procedures have been reported ranging from simple algorithms to complex approaches based on image processing and statistical scene analysis. Examples of rudimentary techniques include an additive counter designed to find the rising edge of a hyperbola in a B-scan (Nagashima et al., 1995)

and a thresholding and clustering algorithm used to find small metal objects buried in a sand box (Herman and Singh, 1995). More sophisticated recent approaches have used: (1) neural networks to detect targets by segmenting and classifying regions of interest within the B-scan (Al-Nuaimy et al., 2002; Shihab et al., 2003; Youn and Chen, 2002); (2) the Hough Transform, a method for finding lines in an image, to detect the positions of different buried objects in laboratory tests (Capineri et al., 1998); and (3) an iterative approach applying principle component analysis to detect targets as anomalies in sonar imagery (Goldman and Cohen, 2004).

Although the reports of these myriad algorithms claimed success detecting targets, there are several issues that preclude their use for analyzing riparian area data: (1) many reports failed to provide sufficient detail to evaluate the merit of the algorithm designs; (2) common metrics have not been defined to measure the performance of the algorithms and compare approaches; (3) different data was used in each report so the published results, if any, cannot be visually compared; and (4) many reports highlighted examples with synthetic or uncluttered B-scan data and robust target reflections (i.e., from metal pipes) that are not realistic for a riparian area application. These approaches may inspire features of an automated preferential flow channel detection algorithm but cannot be directly applied to this problem.

1.4.2.2 Automated Target Geometry Reconstruction

Designing a computer algorithm to not only identify the presence of a target but also to map its three-dimensional geometry is an even more challenging research problem. There are few reported methods for constructing geometries out of the two-dimensional slices of the earth provided by a GPR scan.

Two research groups have used the Hough Transform to link reflected energy from simple pipe structures into linear segments across the GPR data scans (Al-Nuaimy et al., 2002; Dell'Acqua et al., 2004). Dell'Acqua et al. (2004) described an intriguing iterative algorithm that successively detected targets with a likelihood criterion and removed the related energy before the next iteration. The report stated that results for a "variety" of synthetic and real data sets with utility pipes were "robust" but these claims were not detailed.

Tomographic analyses traditionally used in biomedical applications (i.e., CAT-scans) have been applied to generate very high resolution three-dimensional images of vertical macropore structures in soil cores (Perret et al., 1999; Pierret et al., 2002a). These techniques have been combined with GPR for non-invasive target reconstruction (Wielopolski et al., 2002) but the algorithms require impractically high numbers of data samples, and have not been tested in non-laboratory conditions or with target structures larger than 3 mm in diameter.

This review suggests that there are no existing practical non-invasive tools for detecting and reconstructing the three-dimensional structures of preferential flow channels in riparian wetlands. This research will develop and validate methods to map flow channels and other similar subsurface structures detected in GPR scan data.

Chapter 2: Ground-Penetrating Radar First Principles

2.1 Overview

A GPR system detects discontinuities in the soil by transmitting electromagnetic pulses into the ground and receiving the energy reflected off of those discontinuities. The amplitudes of the received data are digitized and stored for display (Fig. 5). By collating the data records, the researcher can image the three-dimensional volume of the discontinuities over an area.

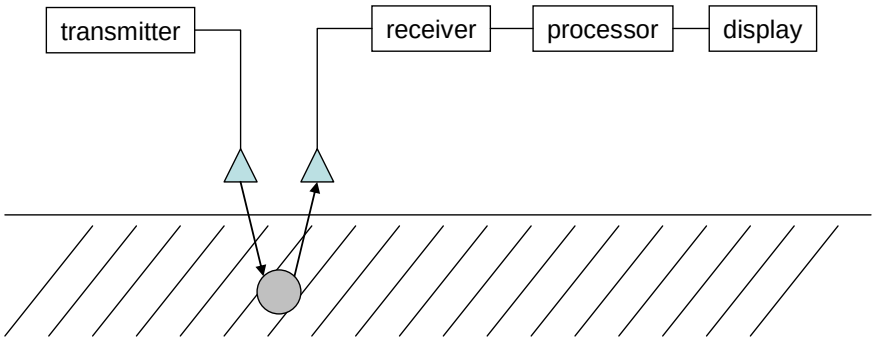

Figure 5. Generalized block diagram of a GPR system (Daniels, 2004).

A digitized recording of the reflections from a single transmission is called a waveform or A-scan. The depth (d) to a given reflector is determined from the two-way travel time (t) for the pulse to travel to the discontinuity and back and the velocity (v) of the pulse through the medium (Eq. [2-1]). Travel time is on the order of nanoseconds.

$$d = \frac{vt}{2} \qquad [2\text{-}1]$$

As the user moves the antenna along the ground, a computer control unit triggers transmissions at a regular distance interval. The set of A-scans collected along a transect, called a B-scan, forms a two-dimensional profile of the subsurface. This "virtual trench" is plotted with two-way travel time or depth on the vertical axis and distance (antenna position on the surface) on the horizontal axis (Fig. 6). B-scan transects are set in a closely-spaced grid to systematically sample a study site.

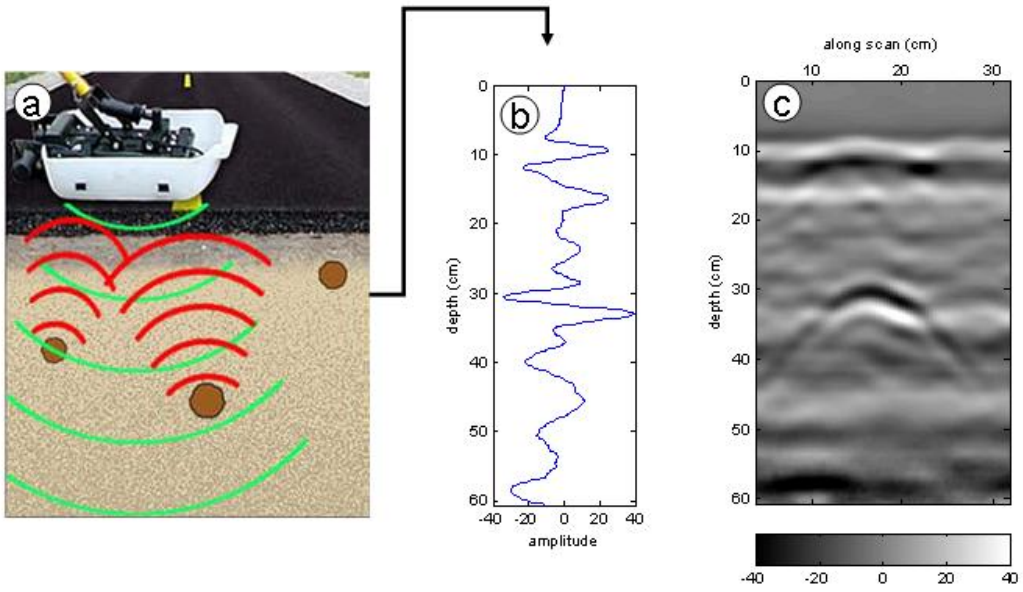

Figure 6. A GPR B-scan is constructed from a series of successive A-scans. (a) The antenna transmits energy (green arcs) and target reflections (red arcs) are (b) recorded in an A-scan waveform; (c) A-scans are compiled to display a soil cross section.

The position (p) within a B-scan (comprised of n_A A-scans) is a function of the waveform number ($wvfm$) and distance between successive waveforms (Δd):

$$p = (wvfm_i - 1) * \Delta d \; ; \quad i = 1,...,n_A \qquad [2\text{-}2]$$

Depth from the surface to a reflector (d) within a waveform that is comprised of n_s samples is given in Eq. [2-3] by the sample number (s_j) and the waveform sample rate (fs) based on the analytic form in Eq. [2-1]. A constant (Δg) accounts for the distance between the antenna and the ground surface.

$$d = \frac{vs_j}{2fs} - \Delta g \; ; \quad j = 1,...,n_s \qquad [2\text{-}3]$$

2.2 Radar Energy Reflection from Subsurface Targets

Radar energy reflects off of discontinuities in electrical conductivity, called dielectric permittivity (k), in a propagating medium. Values of dielectric for different materials are listed in Table 1.

Table 1. Dielectric (k) values of common materials (Conyers, 2004).

Material	k
Air	1
Dry sand	3-5
Dry silt	3-30
Ice	3-4
Asphalt	3-5
Limestone	4-8
Granite	4-6
Permafrost	4-5
Shale	5-15
Clay	5-40
Concrete	6
Saturated silt	10-40
Dry sandy coastal land	10
Average organic-rich surface soil	12
Marsh or forested land	12
Organic-rich agricultural land	15
Saturated sand	20-30
Fresh water	80
Sea water	81-88

The amplitude of a reflection is determined by the contrast in dielectric between the discontinuity and surrounding matrix. One approximation for the relative contrast between two materials (k_1, k_2) is the coefficient of reflection (R) defined in Eq. [2-4]. A pulse propagating through dry sand that encounters water results in a very strong reflection ($R = 0.63$) relative to a pulse moving from dry sand to limestone ($R = 0.10$).

$$R = \frac{\sqrt{k_1} - \sqrt{k_2}}{\sqrt{k_1} + \sqrt{k_2}} \qquad [2\text{-}4]$$

The form of a reflection across a B-scan depends on the orientation of the discontinuity with respect to the scan direction (Al-Nuaimy et al., 2004; Conyers, 2004). The reflection from a pipe that is parallel to the scan and a planar surface such as a stratigraphic boundary, soil horizon, or water table will appear as a horizontal band of energy in the B-scan (Fig. 7 a, c). Conversely, the reflection from a point target like an air void, rock, or pipe perpendicular to the scan will appear as a "reflection hyperbola" (Fig. 7 b, d).

The inverted "U" shape of the hyperbola is due to the conical spreading of radar energy with depth. The upward leg of the hyperbola appears in the B-scan when the radar's wavefront encounters the target. As the antenna is moved towards the target, the two-way travel time of the energy reflected from the target decreases until the antenna is positioned directly above; this is typically the highest point (apex) of the "U" and the reflection with the highest amplitude. Travel time increases as the antenna moves away from the target.

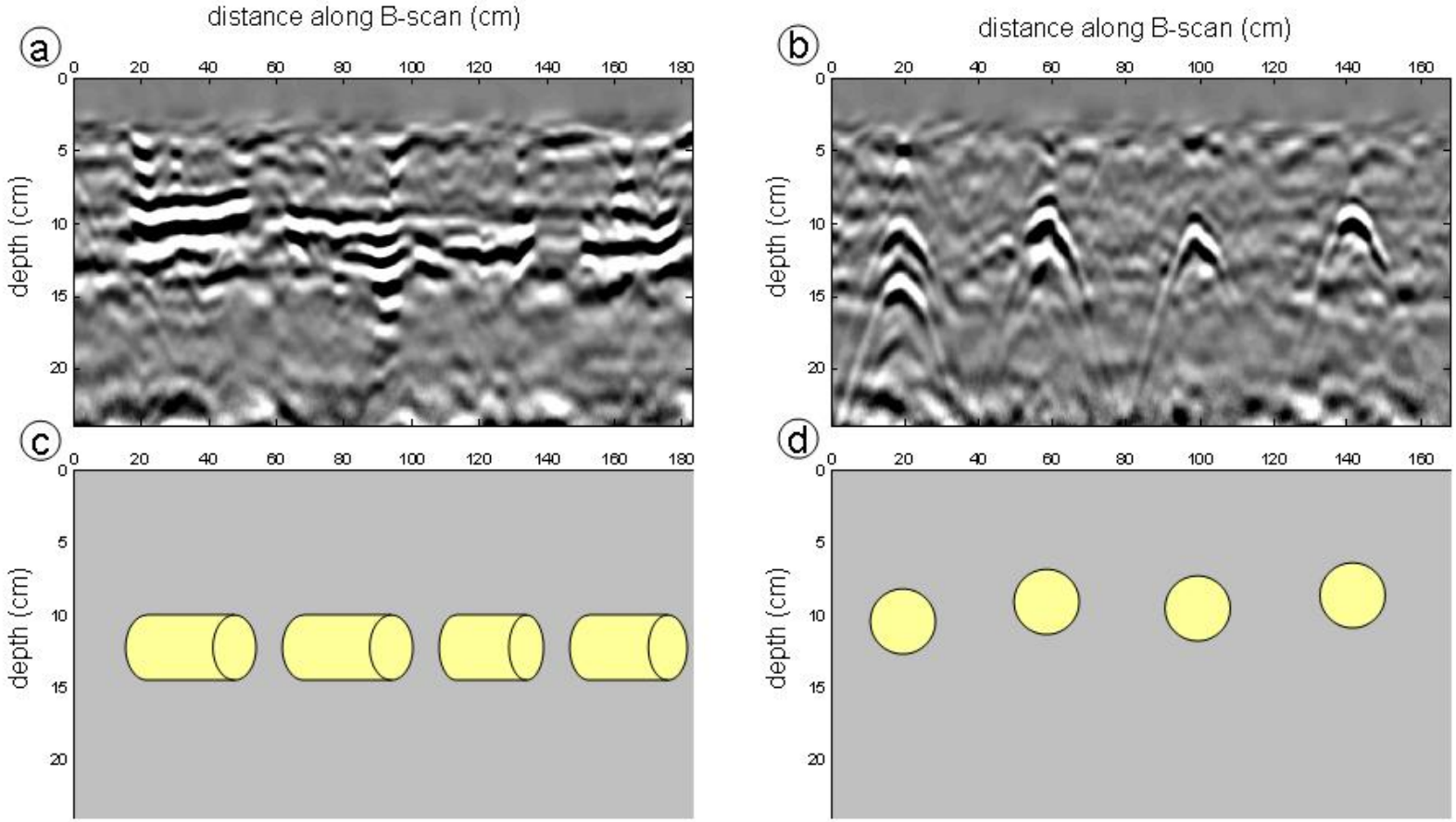

Figure 7. B-scan images for two pipe target orientations relative to the scan line. (a) Constant bands of reflected energy and (b) hyperbola reflections corresponding to pipe targets oriented (c) parallel to the scan line and (d) perpendicular to the scan line.

An A-scan is a composite of many reflections from planar and point reflectors intersected at various angles (Fig. 8). Detection methodologies are designed to parse through this complex composite data and identify only those reflections that correspond to the target objects. To be successful, the methodologies require that reflections from the target are present and have sufficient amplitude. These requirements are met by employing a sensor with adequate resolution, establishing an appropriate scan line layout, and applying signal processing tools that filter out unwanted clutter from the data and enhance the target reflections.

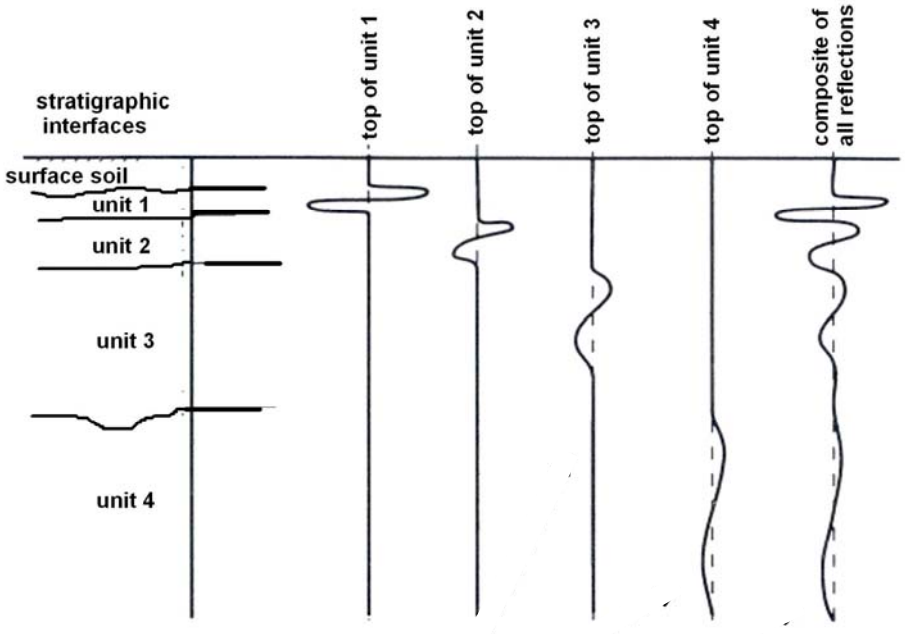

Figure 8. An example A-scan (at far right) is a composite of many subsurface reflections. The radar signal attenuates and its wavelength gets progressively longer with depth (Conyers, 2004).

2.3 Fundamentals of Target Detection

2.3.1 Antenna Transmission Frequency and Resolution

2.3.1.1 Antenna Center Frequency

The antenna center frequency is chosen to ensure that radar energy penetrates deep enough into the soil to reach the target's depth; lower frequency energy penetrates deeper due to the properties of electromagnetic attenuation. However, there is a critical tradeoff between penetration depth and the sensitivity of the sensor to detect discontinuities. A higher frequency antenna can detect smaller targets. Table 2 lists the antenna center frequencies that are recommended based on depth of penetration.

Table 2. Antenna center frequency (f_c) recommendations for various depths of penetration (GSSI Inc. www.geophysical.com).

Depth (m)	f_c (MHz)
0 – 0.5	1600
0 – 1	900
0 – 4	400
0 – 9	200
0 – 30	100
> 30	< 80

2.3.1.2 Discrete Target Resolution

The GPR sensor's resolution, the size of the discrete targets (e.g., pipes) that it can detect, is determined by a number of factors, including the antenna's frequency response, the characteristics of the propagating media compared to the targets, and the post-processing system used to analyze the data. Most importantly, however, target detection is a function of the radar pulse's wavelength. One rule of thumb is that the

minimum resolvable object size is approximately 50% of the radar signal's wavelength at the object depth.

Wavelength (λ) is defined in Eq. [2-5] as a function of the radar wave's velocity (v) and the frequency of the pulse generated by the antenna ($f = f_c$). Velocity is defined in Eq. [2-6] based on the velocity of the radar signal in air (v_{Air}) and the dielectric of the medium (k). Wavelength is depicted in Fig. 9 for different frequencies and dielectrics.

$$\lambda = \frac{v}{f} \qquad [2\text{-}5]$$

$$v = \frac{v_{Air}}{\sqrt{k}} = \frac{0.3m/n\sec}{\sqrt{k}} \qquad [2\text{-}6]$$

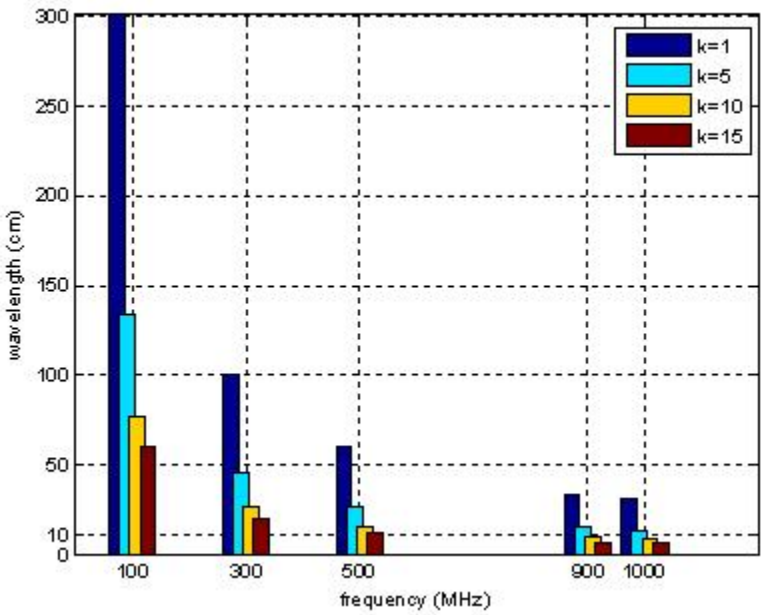

Figure 9. Wavelengths at selected frequencies between 100 and 1000 MHz and dielectrics (k) between 1 and 15.

The most accurate estimate of the minimum resolvable object size is determined based on the wavelength, not at the antenna center frequency, but instead

at the upper end of the GPR pulse's frequency bandwidth. GPR transmissions are Ultra-Wideband (UWB) signals with a bandwidth that is approximately 100% of the center frequency. For example, laboratory measurements have shown that the significant frequency response of a 500 MHz antenna is in the range of approximately 250-700 MHz (Conyers, 2004). In the course of this research, the minimum resolvable object size was estimated based on an *in situ* measurement of the GPR antenna's bandwidth.

2.3.1.3 Adjacent Target Resolution

A second component of target resolution is the separation of adjacent reflectors in depth. The minimum resolvable distance is a full wavelength (i.e., Fig. 10 medium frequency). Otherwise, constructive and destructive interference will corrupt the composite waveform and complicate analysis (Fig. 10 low frequency).

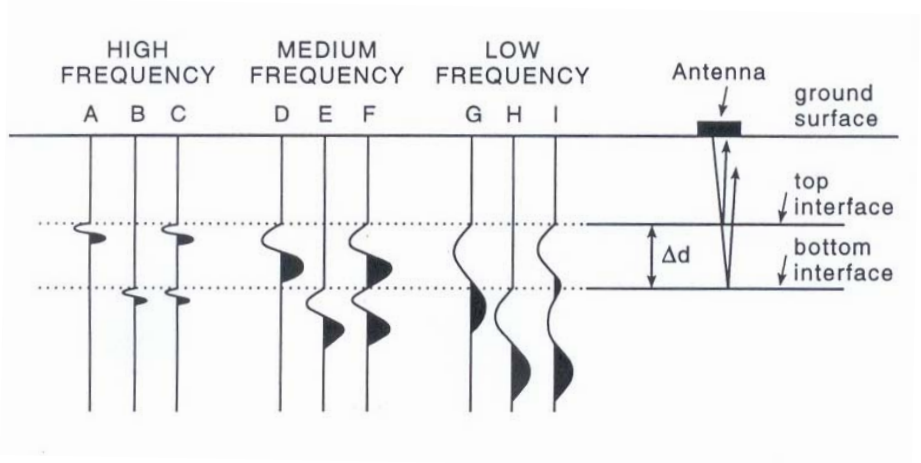

Figure 10. Schematic of the resolution of two vertically-aligned interfaces using high, medium, and low frequency GPR antennae. Reflections from the top (A, D, G) and bottom (B, E, H) interfaces are shown along with the composite (C, F, I) (Conyers, 2004).

2.3.2 Scan Line Layout

A GPR survey is designed with a B-scan line layout and spacing set to maximize the potential for detecting the targets in the study site. Transects should be established perpendicular to the trend or orientation of the target features to maximize the reflection of radar energy. Transect spacing should be set relative to the target length. For detection of point targets (e.g., golf balls), the spacing of the scan lines needs to be smaller than the "footprint" of the sensor's transmission into the ground (Fig. 11). For detection of objects that extend much farther than the footprint of the sensor (e.g., long pipe segments), the foremost consideration for scan spacing should be to capture the degree of variation along the trend direction (i.e., its orientation relative to the scans and tortuosity).

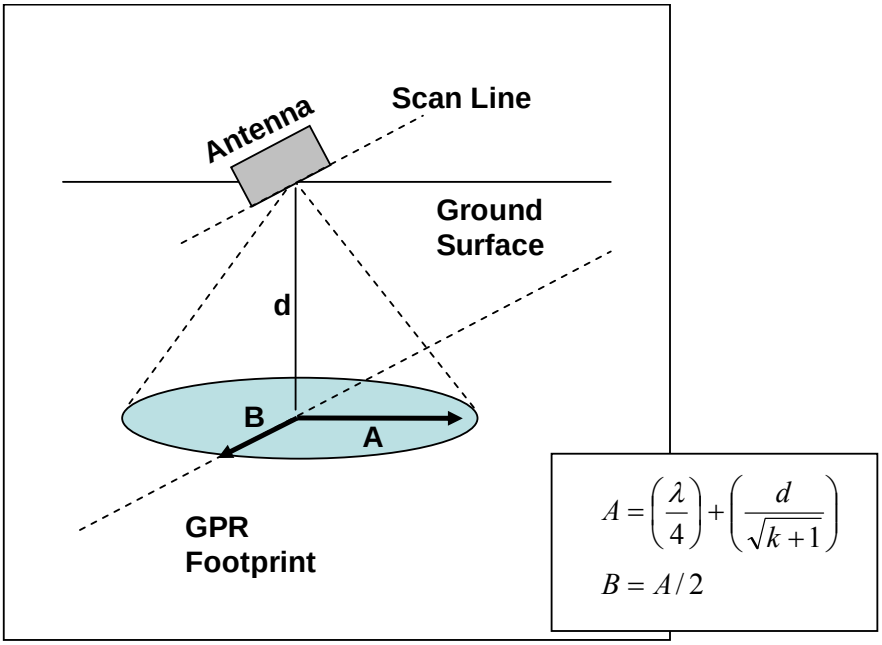

Figure 11. Elliptical GPR footprint with major axis *A* and minor axis *B* at a depth *d*.

The footprint's shape is elliptical with a major axis (A) that is twice the length of the minor (B) axis. The axes lengths are a function of the sensor's wavelength (λ) at its center frequency, the dielectric (*k*) of the medium, and depth (*d*):

$$A = \left(\frac{\lambda}{4}\right) + \left(\frac{d}{\sqrt{k+1}}\right) \qquad [2\text{-}7]$$

$$B = A/2 \qquad [2\text{-}8]$$

2.3.3 Signal Processing Algorithms

Signal processing tools enhance the appearance of target reflections by filtering out confusing and masking energy in the B-scan image. Many techniques were originally developed for applications in the geotechnical sciences (Annan, 2001; Conyers, 2004; Daniels, 2004). One example is the background removal filter that eliminates constant bands of reflected energy (Fig. 12). The use of these filters is subjective and varies depending on the detection problem and the researchers employing them.

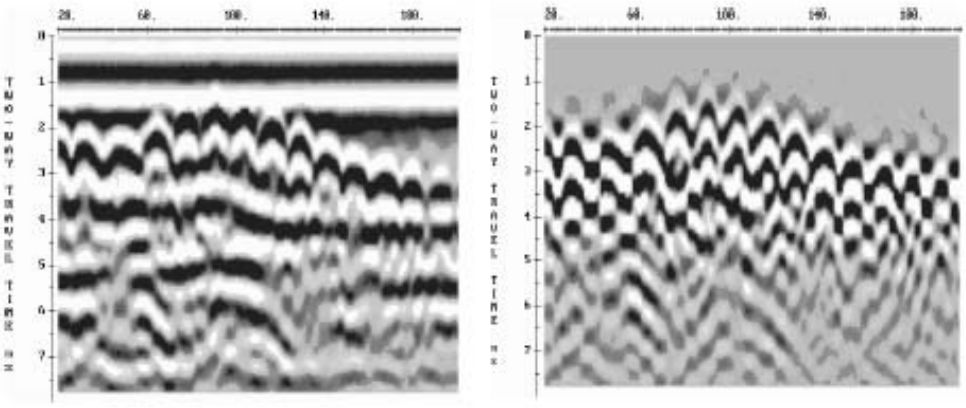

Figure 12. Example of GPR B-scan data before and after a background removal filter is applied. Constant bands (at 0-2 ns, 5 ns) are eliminated (Annan, 2001).

Chapter 3: Experiment I Detection Calibration

3.1 Introduction

Experiment I was conducted as the first step towards developing a generalized field detection procedure for identifying the location of riparian lateral preferential flow channels. A study plot was created with polyvinyl chloride (PVC) pipe targets simulating different sized channels with a variety of contents. GPR reflections from a factorial combination of four pipe diameters (between 1.85 and 5.64 cm) filled with various parts air, fresh water, and salt water were detected using manual and automated analysis methods for scans perpendicular, parallel, and at oblique angles to the orientation of the pipes. The different pipe diameters were used to assess the sensor's ability to resolve various target sizes and to separate the top and bottom interfaces of the pipes. The different scan line orientations were used to determine the ability of the methodologies to detect a target regardless of the angle of intersection.

The goals of the experiment were to: (1) bound the spatial resolution of the GPR sensor; (2) develop manual and automated methodologies for predicting the location of subsurface pipe targets based on a corresponding reflection in a B-scan image; (3) assess the relative performance of the detection methodologies for different scan line orientations; and (4) compare the relative performance of the automated and manual methodologies.

Experiment I included:

1. Creating a field test plot of buried PVC pipe targets with a factorial combination of four pipe diameters and four fill media;

2. Collecting GPR data along scan lines perpendicular to, parallel to, and at 45 degree angles to the targets in the test bed;
3. Developing a manual detection methodology for analyzing the scan data to find reflections from the targets based on "echo-dynamic" characteristics;
4. Developing an automated detection methodology based on the manual methodology using image segmentation techniques from the field of image processing; and
5. Assessing the detection results of the manual and automated detection methodologies using performance metrics including Type I and Type II error rates.

3.2 Description of Experimental Site and Treatment Design

A 4.3 m by 3.0 m field test plot was established in October 2007 at the University of Maryland (UMD) Paint Branch Turfgrass Research Facility in College Park, MD. Sixteen PVC pipes simulating riparian channels filled with different ratios of air and water were buried at a depth of 16.0 cm +/- 1.5 cm in a silt-loam soil. PVC was used because radar energy is almost completely transmitted through plastic and only its contents cause reflections.

Two factors (pipe diameter and fill type) were represented in the test plot. Four nominal pipe sizes (0.5, 1.0, 1.5, and 2.0) of schedule 40 PVC and four fill media (100% fresh water, 50% fresh water 50% air, 100% air, and 100% salt water containing 22 mg/cm^3 iodized sea salt) were used in factorial combination. Nominal pipe size (NPS) and schedule are unitless quantities defined by the American Society of Mechanical Engineers to standardize cross-sectional size (Table 3). The salt water

treatment was included as a fill type although it does not occur in the fresh water riparian wetlands.

Table 3. Outer diameter (OD), wall thickness, and inner diameter (ID) for the nominal pipe sizes (NPS) of schedule 40 pipes used in this study.

NPS	OD (cm)	Wall Thickness (cm)	ID (cm)
0.5	2.13	0.28	1.85
1.0	3.34	0.34	3.00
1.5	4.83	0.37	4.46
2.0	6.03	0.39	5.64

The pipes were laid out in a systematic design with NPS as rows and fill type as columns (Fig. 13). The pipes were centered in trenches and set parallel to the ground surface. Excavated soil was hand packed into the trenches under and around each pipe to prevent the introduction of voids in the surrounding soil matrix. The turf was replaced and the soil was tamped down. Non-target reflectors like tree roots or large rocks were not observed in the profile during excavation.

The pipe length (91 cm) and distance between pipes (102 cm – 117 cm) were set to avoid artifacts that could arise from interactions with the leading edge of the GPR pulses.

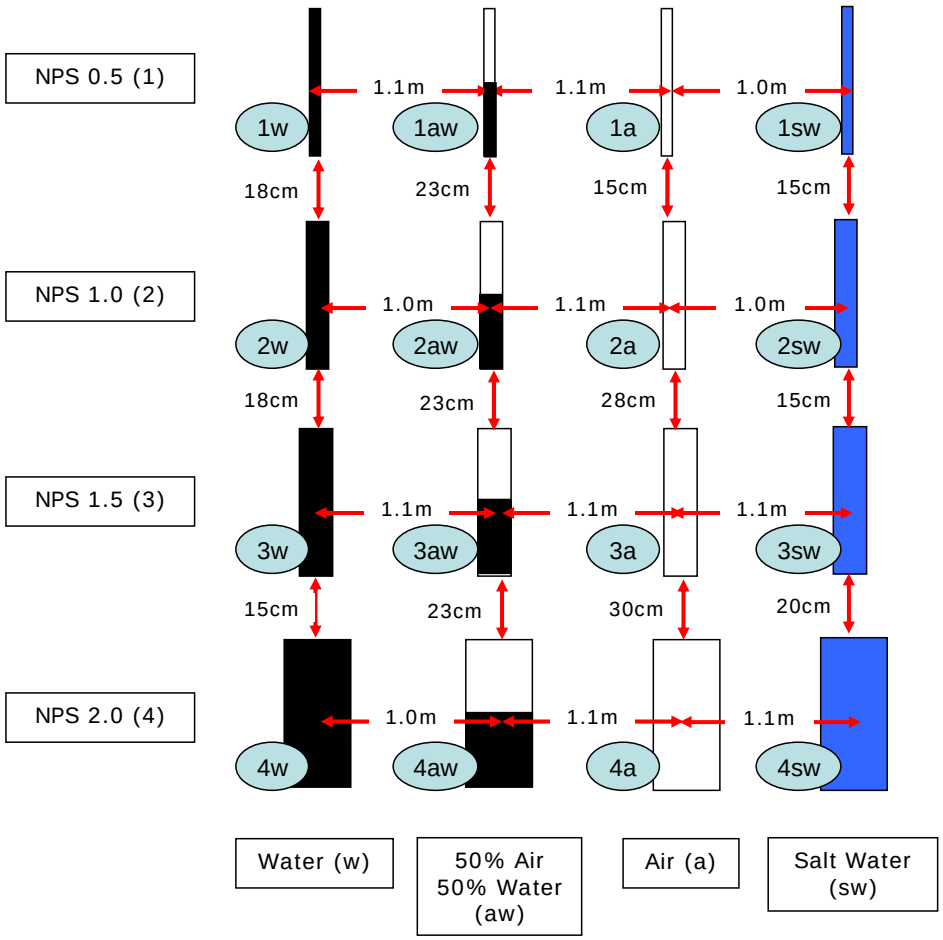

Figure 13. Experiment I schematic with nominal pipe size (NPS) and pipe fill type.

3.3 GPR Data Collection

GPR scan data were collected in November 2007 using a Geophysical Survey Systems Inc. (GSSI) portable TerraSIRch Subsurface Interface Radar system (SIR-3000, Salem, NH). A 900 MHz antenna center frequency was used because it is recommended for detection of targets within 1 m of the surface (Table 2). Transects for the GPR scan lines were set perpendicular, parallel, and at 45 degree angles to the grid of buried pipes (Fig. 14, 15).

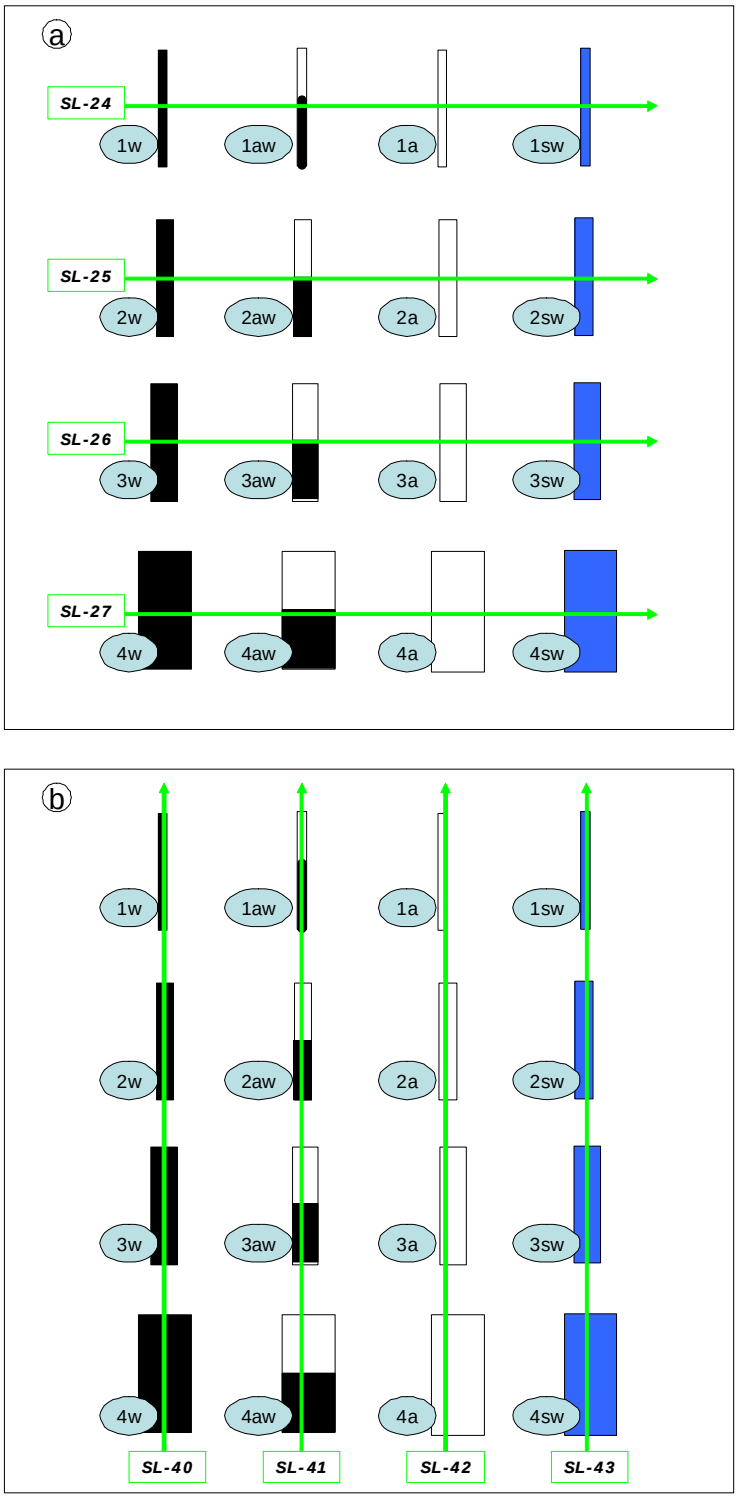

Figure 14. Experiment I GPR scan lines (SL) (a) perpendicular (SL 24-27) and (b) parallel (SL 40-43) to the pipe grid. Green arrows indicate scan direction.

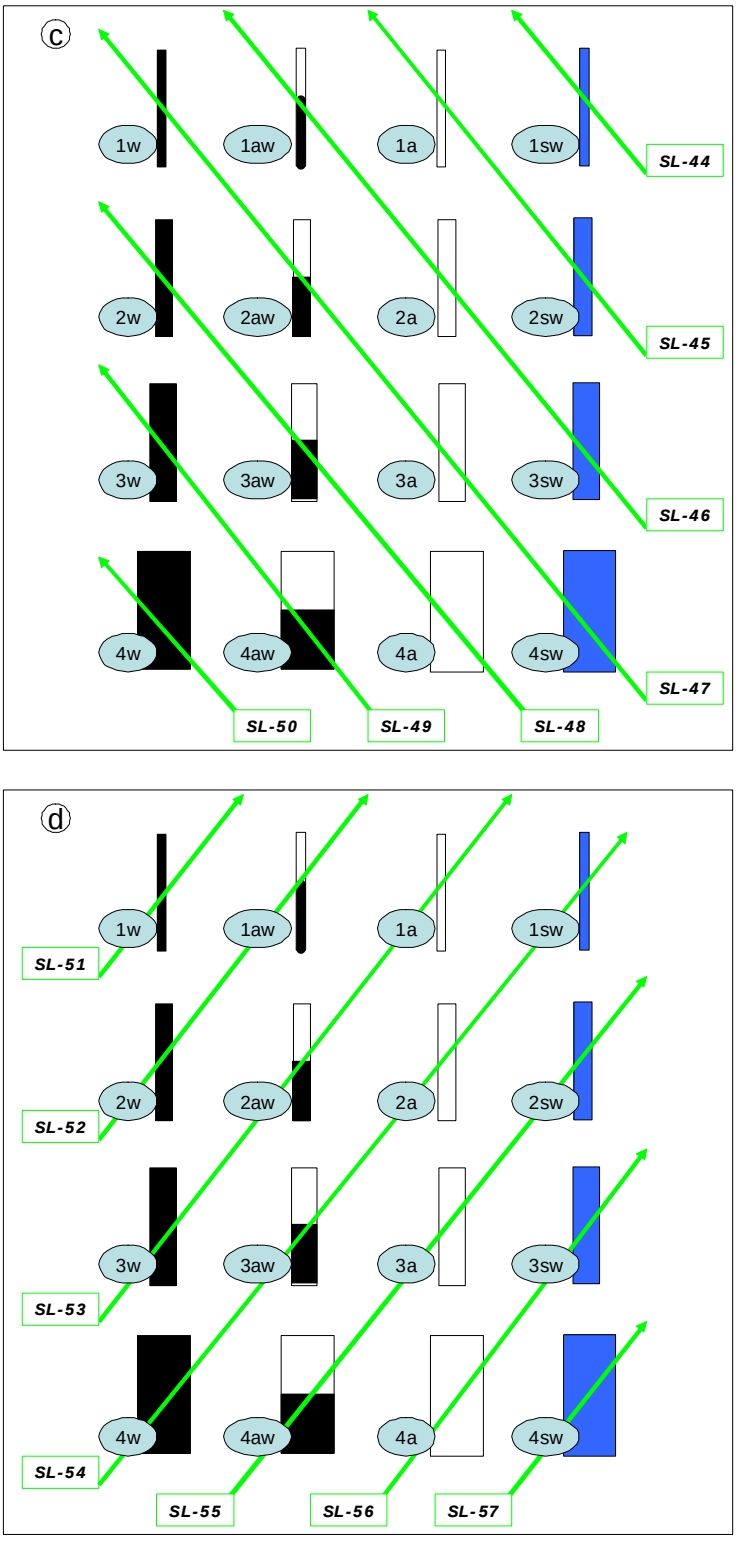

Figure 15. Experiment I GPR scan lines at 45 degrees to the pipe grid, both (c) right-to-left (SL 44-50) and (d) left-to-right (SL 51-57). Green arrows show scan direction.

A survey cart was used to transport the antenna and data acquisition computer over each study transect (Fig. 16). The antenna was carried in a plastic tub that was transparent to the radar energy. A-scans were digitized and saved to a compact flash memory card and transferred to a personal computer. The distance between B-scan samples along the ground (Δd) was 5 mm and the A-scan sample rate (fs) was 30.1 samples/nsec (Eqs. [2-2] and [2-3]).

Figure 16. GPR data collection equipment. The arrow indicates the scanning direction. A = the GPR antenna housed in an orange casing within the white plastic tub; B = B-scan starting point; and C = GPR control unit and computer.

Propagation velocity was calibrated to synchronize the known pipe depths to the depths indicated in the real-time A-scan readout at the first half-cycle of the reflection hyperbola peak. A time-varying gain profile, used to compensate for the exponential attenuation of the radar energy over depth, was calibrated automatically by the GPR computer to control the dynamic range of the recordings. The five points that made up the gain curve (9, 9, 25, 25, and 41) were set based on reflections from a 0.5 NPS pipe.

During data collection, the pipe locations within each scan were noted by triggering electronic markers that were saved with each of the B-scans data files. For the perpendicular and angled scan lines, the data were marked each time the center of the antenna housing was directly above a pipe. For the parallel scan lines, the data were marked each time the center of the antenna housing was at the end point of a pipe.

3.4 GPR Sensor Parameter Estimation

3.4.1 Discrete Target Resolution

The minimum resolvable object size was estimated for the 900 MHz antenna center frequency to compare against observed detection performance in the field test plot. Given an estimated value of the dielectric for an average silt-loam soil (k = 15), velocity was calculated from Eq. [2-6] as:

$$v = \frac{v_{Air}}{\sqrt{k}} = \frac{0.3\, m/n\sec}{\sqrt{15}} = 0.077\, m/n\sec$$

For this velocity and center frequency, the corresponding wavelength (λ) was calculated from Eq. [2-5] as:

$$\lambda = \frac{0.077\, m/n\sec}{0.9} = 8.6cm$$

The frequency bandwidth of the 900 MHz UWB antenna was measured *in situ* by analyzing recorded A-scan data (Fig. 17). Log-scaled amplitude was calculated as a function of frequency (*f*) with the absolute value of the Fast Fourier Transform (FFT) after a hamming window (*hamm*) was applied to the input data (*x*) (Eq. [3-1]).

$$amplitude(f) = 20 * \log_{10}\left|FFT(hamm * x)\right| \qquad [3\text{-}1]$$

The bandwidth was measured for amplitudes 3 dB and 6 dB below the peak (0 dB). The 6 dB bandwidth was 400-1250 MHz.

The wavelength at the upper bound of the bandwidth, 1250 MHz, was calculated from Eq. [2-5] as:

$$\lambda = \frac{0.077\, m/n\sec}{1.25} = 6.2cm$$

Therefore, the minimum resolvable object size was estimated as 3.1 cm (λ/2) and the minimum spatial resolution of adjacent reflectors was estimated as 6.2 cm (λ). These estimates were compared to the range of target sizes detected in the test plot.

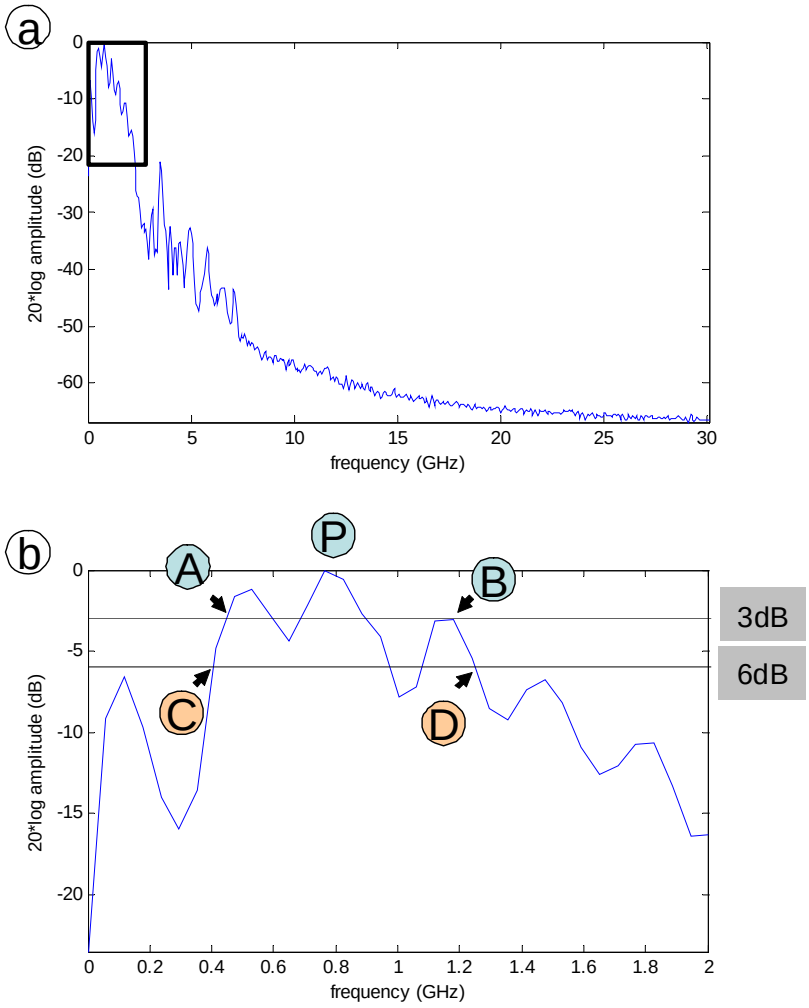

Figure 17. Average 900 MHz antenna frequency response (n=283 A-scans) across (a) the full frequency band (0-30 GHz) and (b) a narrow region around the peak (0-2 GHz). P = peak response = 0 dB at 766 MHz; [A, B] = [lower, upper bounds] of 3 dB bandwidth = [430, 1180] MHz; and [C, D] = 6 dB bandwidth = [400, 1250] MHz.

3.4.2 GPR Footprint

The major axis (A) of the 900 MHz GPR transmission footprint ($\lambda = 8.6$ cm) given the depth of objects to detect ($d = 0.5$ m), and average soil dielectric ($k = 15$), was calculated from Eq. [2-7] as:

$$A = \left(\frac{0.086m}{4}\right) + \left(\frac{0.5m}{\sqrt{15+1}}\right) = 15cm$$

At the upper bound of the sensor bandwidth ($\lambda = 6.3$ cm) and a depth of 0.5 m, the major axis was:

$$A = \left(\frac{0.063m}{4}\right) + \left(\frac{0.5m}{\sqrt{15+1}}\right) = 14cm$$

This footprint size ensured that there would not be artifacts due to the pipe length (91 cm) and distance between pipes (102 cm – 117 cm).

3.5 GPR Data Analysis

3.5.1 Filtering

The GPR scan data were analyzed using software filters and visualization tools created with the MATLAB software package (Ver. 7.3.0, R2006b, Natick, MA).

A background removal filter was used to enhance target reflections by removing constant bands of clutter energy. The filter subtracted background noise models (BM) from each of the n_A A-scans (indexed by p) that made up the B-scan data (Y):

$$YBR_p = Y_p - BM\ ;\quad p = 1,...,n_A \qquad [3\text{-}2]$$

The background model was calculated for each of the n_s depth samples (indexed by d) as the mean amplitude across all A-scans at that depth:

$$BM_d = \frac{\sum_{p=1}^{nA} Y_{p,d}}{n_A}; \quad d = 1,...,n_s \qquad [3\text{-}3]$$

A moving window average filter, a slight variant of background removal, subtracted a background noise model (BMMW) calculated across local neighborhoods *mwl* scan lines long from each A-scan (indexed by p):

$$YMW_p = Y_p - BMMW_p; \quad p = 1,...,n_A \qquad [3\text{-}4]$$

The noise model was calculated for each depth sample (indexed by d) as the mean amplitude across *mwl* A-scans at that depth:

$$BMMW_{p,d} = \frac{\sum_{pp=p-mwl/2}^{pp+mwl} Y_{pp,d}}{mwl}; \quad d = 1,...,n_s \qquad [3\text{-}5]$$

3.5.2 Manual Target Detection Methodology

The manual target detection methodology consisted of a visual search of the B-scan images for the energy reflected from a target. Sufficient amplitude was required to discern a proper reflection (as determined from the reflection's shape) above background amplitude fluctuations.

Background removal and moving window average filters were applied to the raw scan data and I examined the result for the coherent "echo-dynamic" patterns of a reflection hyperbola (Fig. 7 b) or bands from a pipe oriented parallel to the scan direction (Fig. 7 a). "Echo-dynamics" describes the amplitude characteristic of a reflection: increasing as the sensor approaches the target and decreasing as it moves

away. Diffuse reflections from clutter sources should not exhibit these dynamics or have sufficient amplitude and coherent shapes.

Pipe locations were predicted two different ways to assess differences, if any: at the apex of the reflection hyperbola and at the position of maximum absolute amplitude in the first half-cycle of the reflection.

An example shows the position-depth (Fig. 18 a) and position-amplitude (Fig. 18 b) characteristic of reflection hyperbola echo-dynamics. The true position of the pipe is plotted on top of the scan data.

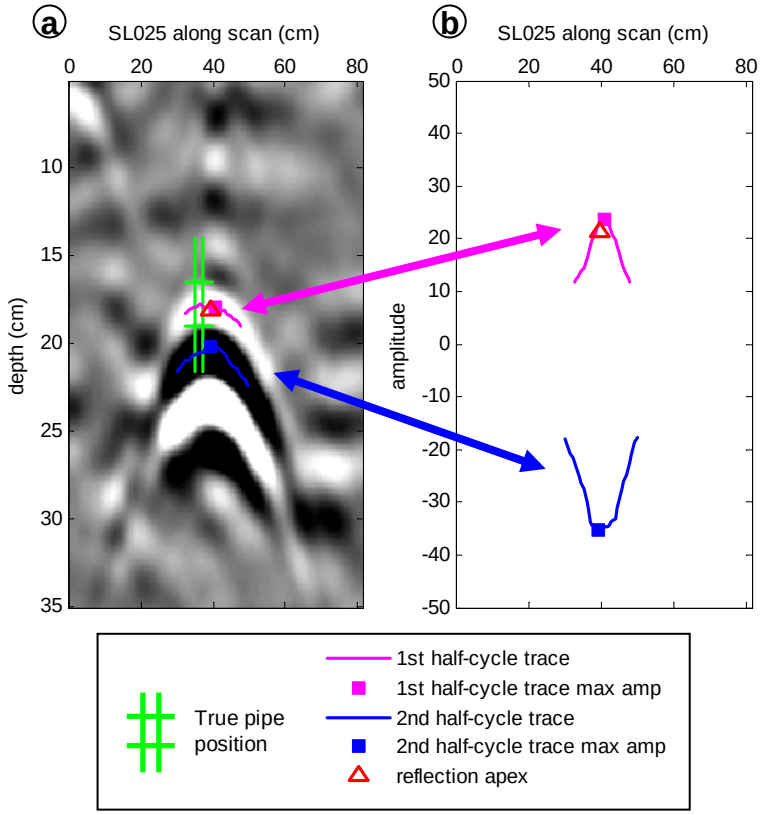

Figure 18. Reflection hyperbola "echo-dynamics" for a perpendicular target intersection in (a) position-depth and (b) position-amplitude.

The maximum half-cycle amplitude was located by tracing the extent of the reflection. Points neighboring the response apex in depth and along the B-scan were searched. The search was terminated at the half-cycle's 3 dB amplitude contour; a point was considered part of that boundary when the amplitude no longer exceeded half the magnitude of the overall maximum. The trace tracked the depth of the local maximum amplitudes at each position sample within the boundary. The overall peak amplitude was recorded as the position with the largest absolute amplitude along the trace.

3.5.3 Automated Target Detection Methodology

A computerized target detection methodology I have named the Automated GPR Target Detection (AGTD) algorithm was created based on the manual detection procedure. AGTD identifies target reflections in B-scan data by conditioning the input data, searching for the echo-dynamics of individual half-cycle responses, and linking those characteristic responses over depth (Fig. 19).

The algorithm was designed based on the following assumptions: (1) target reflections have echo-dynamic characteristics, (2) target reflections include multiple half-cycles with alternating sign (i.e., +/-/+ or -/+/-), (3) the peak amplitudes of each alternating half-cycle occur at a common position along the scan, and (4) the half-cycle trace bandwidth is at least 11.43 cm.

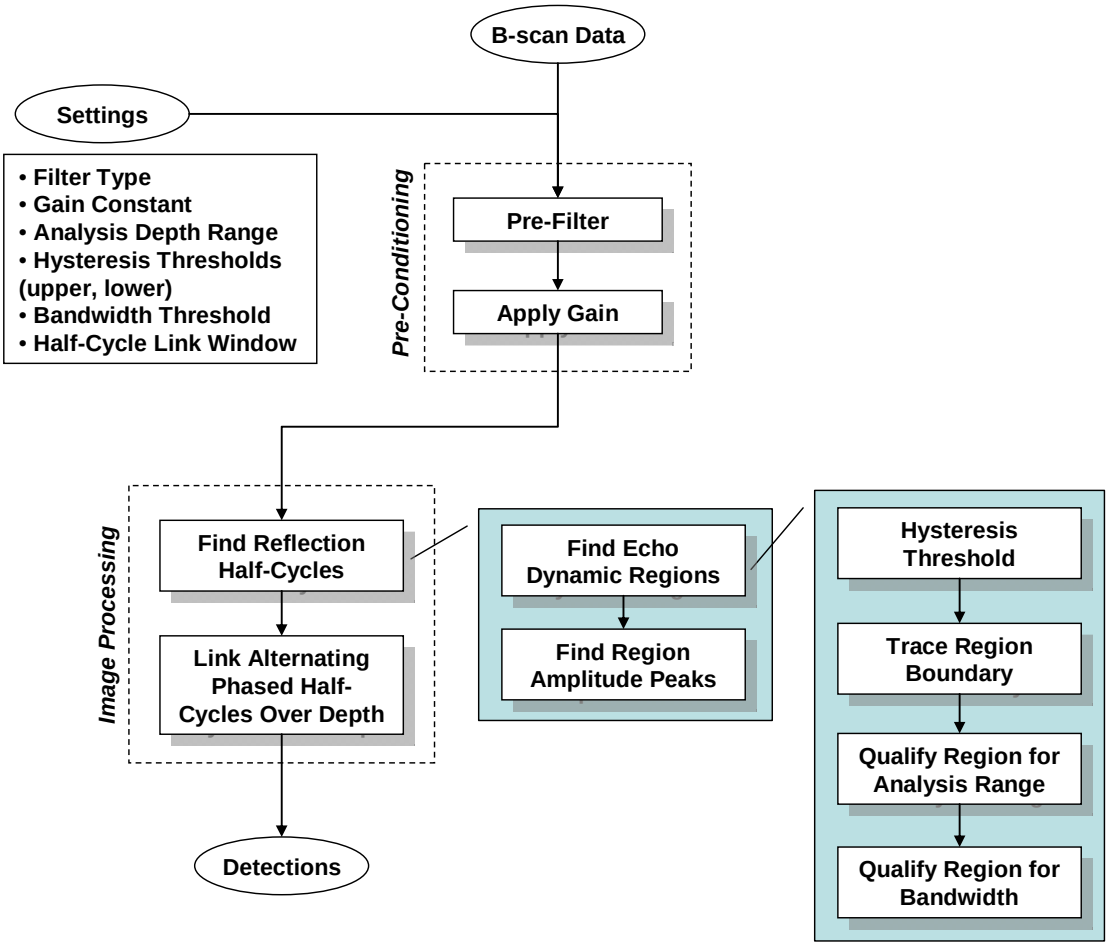

Figure 19. Automated GPR Target Detection (AGTD) algorithm block diagram. The input data is conditioned and image processing analyses are performed according to the supplied settings.

The process is initialized with a pre-filter (moving window average) to eliminate constant band responses. An analysis depth window is set with the range of depths over which the process segments the image into candidate reflection half-cycles (by default, between the ground surface and the maximum recorded depth).

Boundaries of echo-dynamic response are isolated within the analysis depth range using a hysteresis thresholding process; points in the B-scan are found that exceed an upper amplitude threshold level and regions are formed with all the neighboring points that exceed a lower threshold. This segmentation operator is similar to that used by Al-Nuaimy et al. (2002) and Shihab et al. (2003) as a precursor to their neural net-based automated detection algorithm.

Response regions are considered potential half-cycles of a target reflection provided that the minimum bandwidth requirement (width along the scan > 11.43 cm) is satisfied (Fig. 20 a). The peak within the region is set as a centroid based on amplitude (Fig. 20 b). Targets are predicted at locations where alternating phased peaks are found that stack within a window of depth and position (Fig. 20 c).

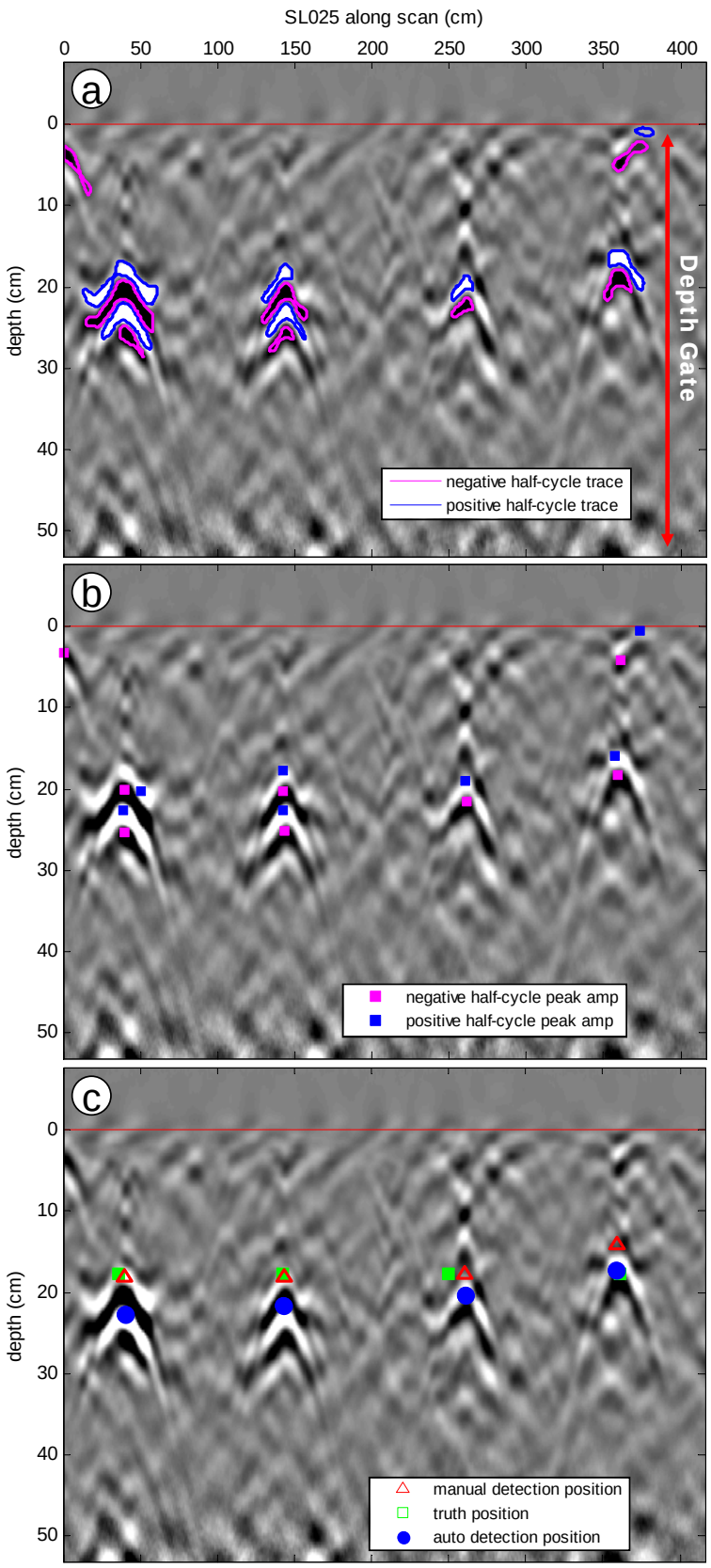

Figure 20. Example application of AGTD for all depths below the ground surface of a B-scan (depth gate). (a) Boundaries of positive and negative regions isolated by hysteresis thresholding, (b) centroid peak amplitude positions, and (c) automated detections compared with manual identified reflection apexes and truth target locations.

3.6 Detection Accuracy Assessment Methods

The accuracy of the manual and automated detection methodologies was assessed by calculating (1) the numbers of valid detections and dismissals as well as Type I and Type II error rates and (2) position and depth prediction errors.

3.6.1 Detection Error Rates

The components used to calculate the Type I and Type II error rates were: (1) possible detections, (2) correct detections, (3) incorrect detections, (4) missed detections, and (5) parts of the scans with no targets and no detections.

The set of all possible detections, *P*, was comprised of the *p* intersections of scan lines with pipes. The set of correct detections, *D*, was comprised of the *d* analysis detections that corresponded to true pipe locations. Perfect detection performance would entail the complete intersection of *D* and *P*. The set of incorrect detections (Type I errors), called false alarms, *FA*, consisted of the *fa* detections that did not correspond to truth. The set of missed detections (Type II errors), *ND*, were the *nd* possible detections that were not contained within the correct detections set. Finally, the set *NP* consisted of the *np* samples where there were no possible detections and no detections were found.

To calculate *NP*, the area of each B-scan below the ground surface was divided into a grid of possible detection cells. The number of grid cells without a member of *P* (*ngc*) and the number of those cells without a *FA* (*np*) was counted and summed across all scan lines. The size of the grid cells was set based on an average assumed reflection hyperbola size: 22.86 cm along the scan and 12.4 cm deep.

The following metrics were calculated based on these components:

$$truePositiveRate = \frac{d}{p} \quad [3\text{-}6]$$

$$trueNegativeRate = \frac{np}{ngc} \quad [3\text{-}7]$$

$$typeIErrorRate = \frac{fa}{np} \quad [3\text{-}8]$$

$$typeIIErrorRate = \frac{nd}{p} = 1 - \frac{d}{p} \quad [3\text{-}9]$$

$$precision = \frac{d}{d + fa} \quad [3\text{-}10]$$

$$totalAccuracy = \frac{d + np}{d + np + nd + fa} \quad [3\text{-}11]$$

An example scan line (Fig. 21) intersecting four pipes ($p = 4$) had 105 total grid cells (21 along the scan by 5 deep) and four valid detections ($d = 4$, $fa = 0$). The detections were valid because they occurred in grid cells neighboring the true pipe locations. Therefore, *ngc* was 101 (105-4), *np* was 101 (*ngc*-0), the true negative rate was 100.0% (101/101), and the Type I and II error rates were zero.

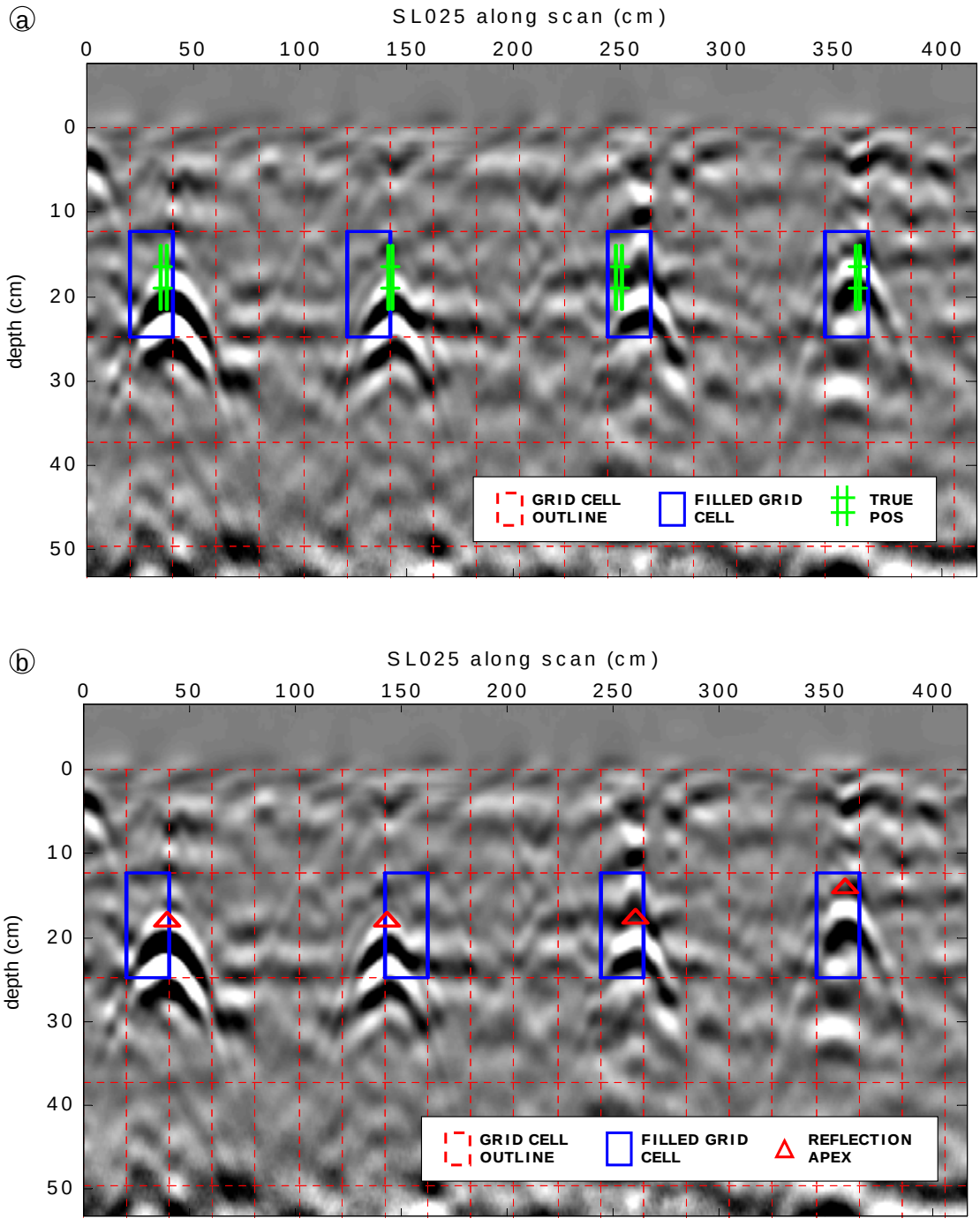

Figure 21. Example B-scan data with the potential detection grid overlaying the (a) truth pipe positions and (b) manually estimated pipe positions.

3.6.2 Position and Depth Prediction Errors

Position error (P_e) was defined as the difference between the position prediction along the scan (P_p) and truth position along the B-scan (P_t):

$$P_e = P_p - P_t \qquad [3\text{-}12]$$

Depth error (D_e) was defined as the difference between the depth at the prediction position (D_p) and truth depth (D_t):

$$D_e = D_p - D_t \qquad [3\text{-}13]$$

3.7 Results

3.7.1 Manual Target Detection Accuracy

3.7.1.1 Detection Error Rates

There were 64 detection opportunities ($p = 64$) of the 16 pipes at the 4 angles of intersection (including the scan lines parallel to the pipes); 59 were correctly identified ($d = 59$). Five of the 0.5 NPS pipe intersections (1w, 1w, 1aw, 1sw, and 1sw) at 45 degree angles were not detected ($nd = 5$) because of insufficient amplitude (Fig. 22). There were no false alarms ($fa = 0$). Of 2210 total grid cells, no targets were present in 2146 ($ngc = 2146$) and no pipes were predicted to be present in any of those 2146 ($np = 2146$).

The B-scan image from scan line 25 is given as a representative example of the effects of data conditioning and the results of the detection analysis (Fig. 23).

Performance metrics are listed in Table 4. The complete set of B-scan data images and detection results for each scan line is given in Appendix A and an in-depth examination of reflection hyperbola properties is provided in Appendix B.

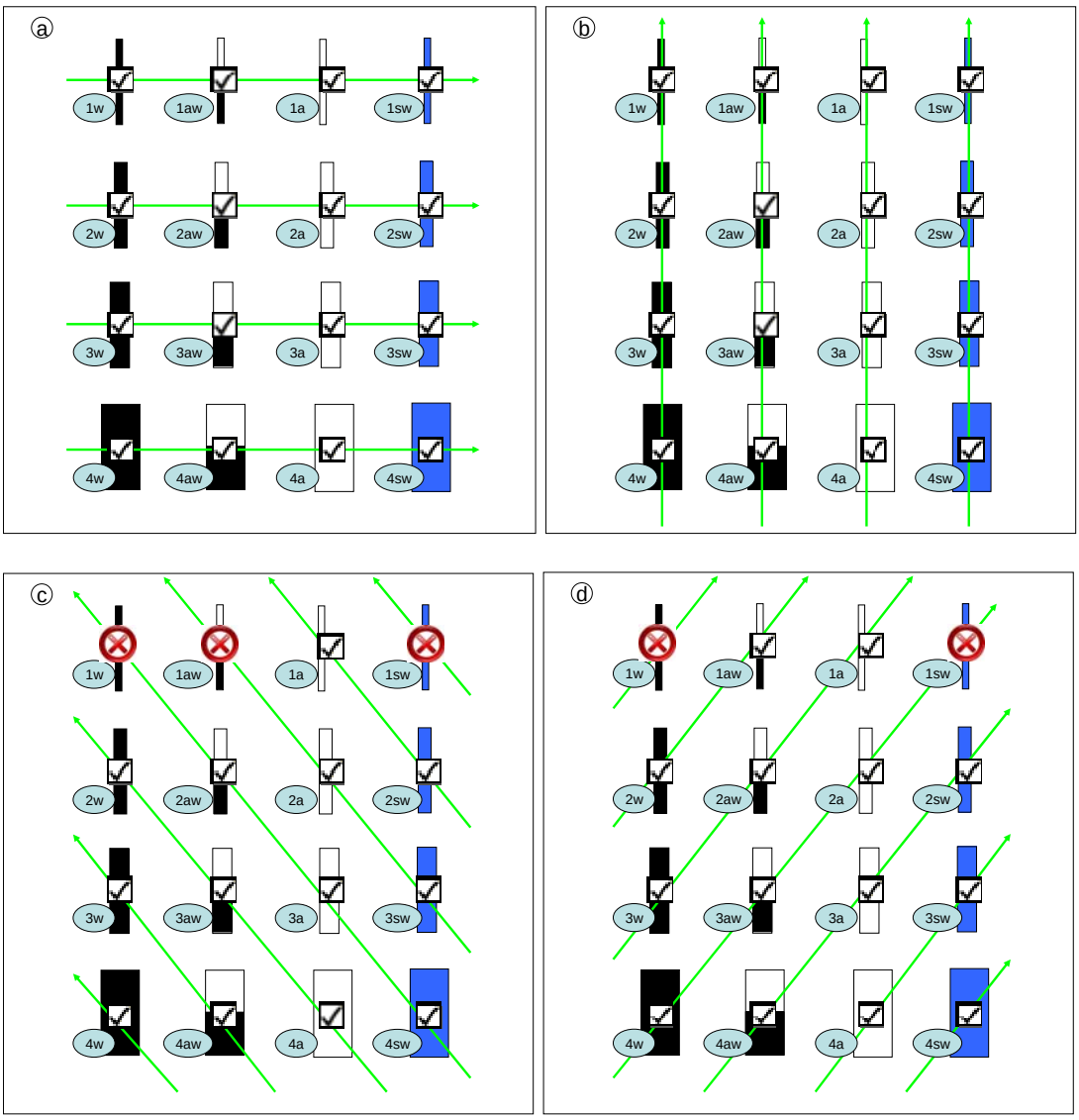

Figure 22. Experiment I manual detection results by scan line orientation: (a) perpendicular intersection, (b) parallel intersection, (c) right-to-left angled intersection, and (d) left-to-right angled intersection. Check marks indicated the pipe was detected, X's indicated the pipe was not detected.

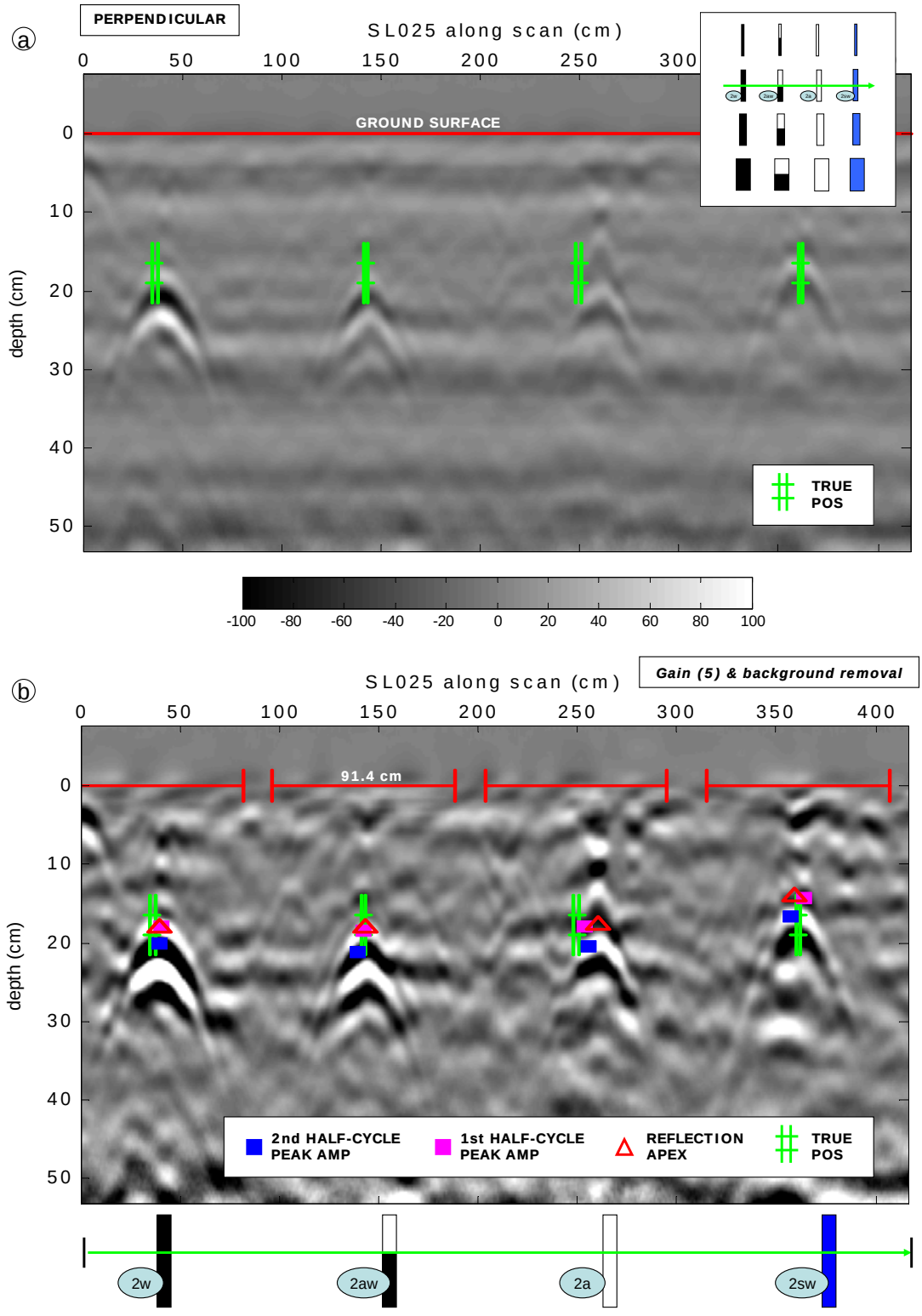

Figure 23. Representative scan line data (SL-25) (a) before and (b) after data conditioning. True and predicted positions are noted.

Table 4. Experiment I manual detection performance metrics.

Detection Performance Metric	Manual Procedure Result
Total Grid Cells	2210
Grid Cells Not Containing Truth	2146
Empty Grid Cells Predicted Empty	2146
Potential Detections	64
Accurate Detections	59
False Alarms (Type I Errors)	0
Missed Detections (Type II Errors)	5
True Positive Rate	92.2%
True Negative Rate	100%
Type I Error Rate	0%
Type II Error Rate	7.8%
Precision	100%
Total Accuracy	99.8%

3.7.1.2 Position and Depth Prediction Errors

Box plots of the position (P_e) and depth (D_e) prediction errors were created from the apex of the response hyperbolas (Fig. 24 a, c) and from the locations of the maximum amplitudes in the first reflection half-cycle (Fig. 24 b, d).

The position errors were almost entirely greater than zero and were highest for the angled pipe intersections, meaning that the predictions consistently over-estimated the target's position (from the reflection apex: mean P_e = 11.1 cm**,** standard deviation = 8.0 cm; from peak amplitude: mean P_e = 12.9 cm**,** standard deviation = 9.1 cm).

The depth estimates (from the reflection apex: mean D_e = -0.6 cm, standard deviation = 1.8 cm; from peak amplitude: mean D_e = -0.3 cm, standard deviation = 1.8 cm) were generally accurate within 4 cm (46% of the wavelength at the antenna center frequency and 65% of the wavelength at the upper bound of the antenna frequency response). There were negligible differences between the position and depth errors for estimates based on the reflection apexes versus the half-cycle maximum amplitude.

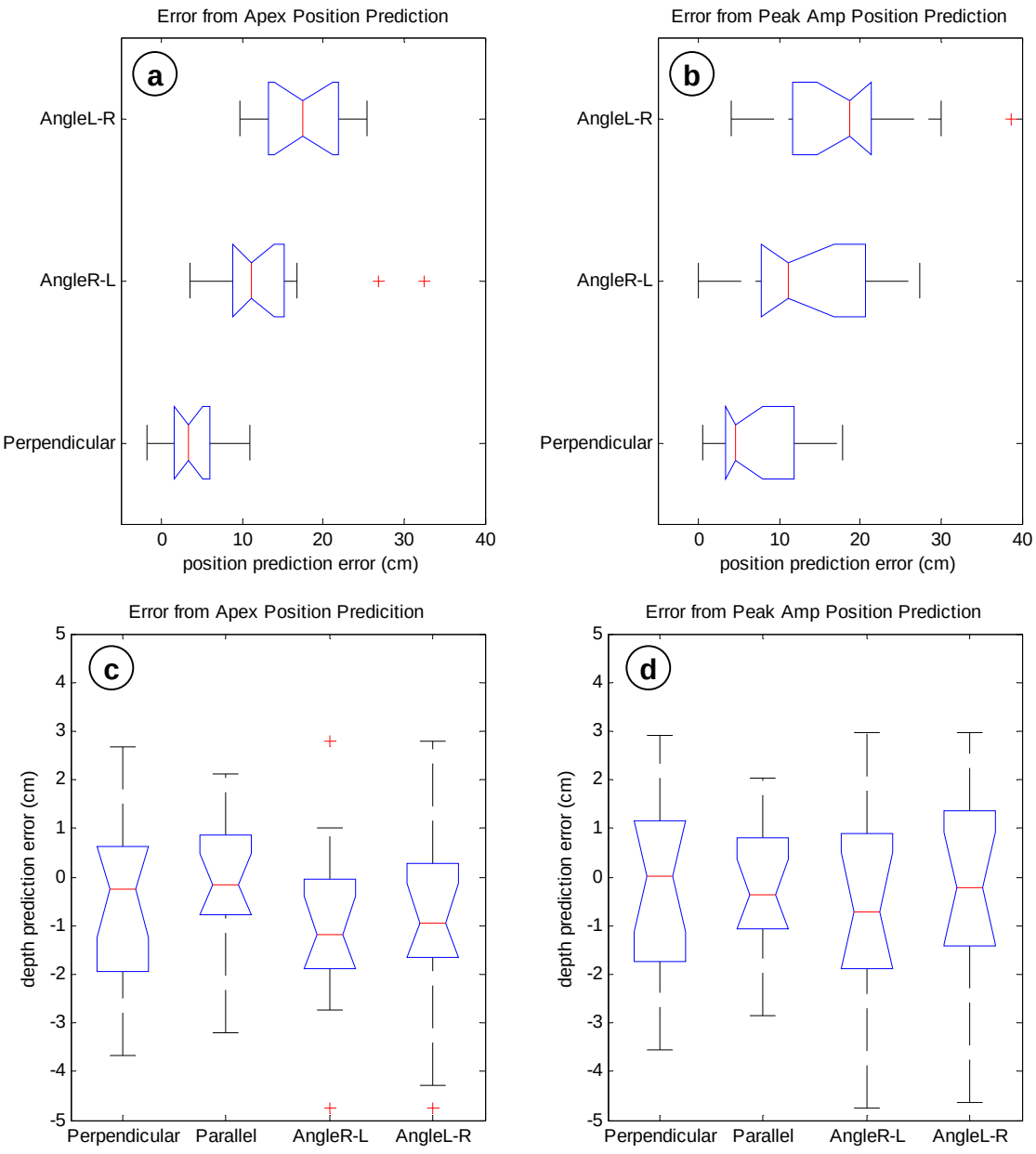

Figure 24. Box plots of the (a, b) position prediction errors across all levels and factors (difference between prediction and truth, Eq. [3-12]), and (c, d) depth prediction errors across all levels and factors (difference between prediction and truth, Eq. [3-13]). The detection position was set (a, c) at the apex of the first half-cycle response and (b, d) at the maximum amplitude of the first half-cycle response.

3.7.2 Automated Target Detection Accuracy

The detection results of the AGTD algorithm are summarized in Table 5 and Fig. 25 (refer to Appendix A for the detailed results for each scan line). A higher relative fraction of detections were missed along angled scan lines (11 of 32) as compared to perpendicular scans (4 of 16). The overall performance was not as good as the manual detection process, with a higher number of both Type I (42 versus 0) and Type II errors (19 versus 5).

The higher Type I error rate was largely artificial. Most of the false alarms occurred within 5 cm of the soil surface above truth target positions, indicating that they likely corresponded to air gaps in the disturbed soil and turf introduced by digging the pipe trenches. Disregarding this depth range (0-5cm), the detection rate remains unchanged but the Type I error rate drops to 0.7% which is comparable to the manual procedure.

Position and depth prediction errors were not calculated because the locations of the automated detections matched those of the manual procedure set based on the maximum half-cycle amplitude. Therefore, the automated procedure's location prediction errors can be referenced from Fig. 24 b, d.

Table 5. Experiment I automated detection performance metrics for the full depth range and after eliminating false alarms from surface artifacts by considering only a subset of depth below 5 cm.

Metric	Automated Procedure (Full Depth Range)	Automated Procedure (Depth Subset)
Total Grid Cells	2210	1768
Grid Cells Not Containing Truth	2146	1704
Empty Grid Cells Predicted Empty	2103	1693
Potential Detections	64	64
Accurate Detections	45	45
False Alarms (Type I Errors)	42	8
Missed Detections (Type II Errors)	19	19
True Positive Rate	70.3%	70.3%
True Negative Rate	98.0%	99.3%
Type I Error Rate	2.0%	0.7%
Type II Error Rate	29.7%	29.7%
Precision	51.7%	84.9%
Total Accuracy	97.2%	98.4%

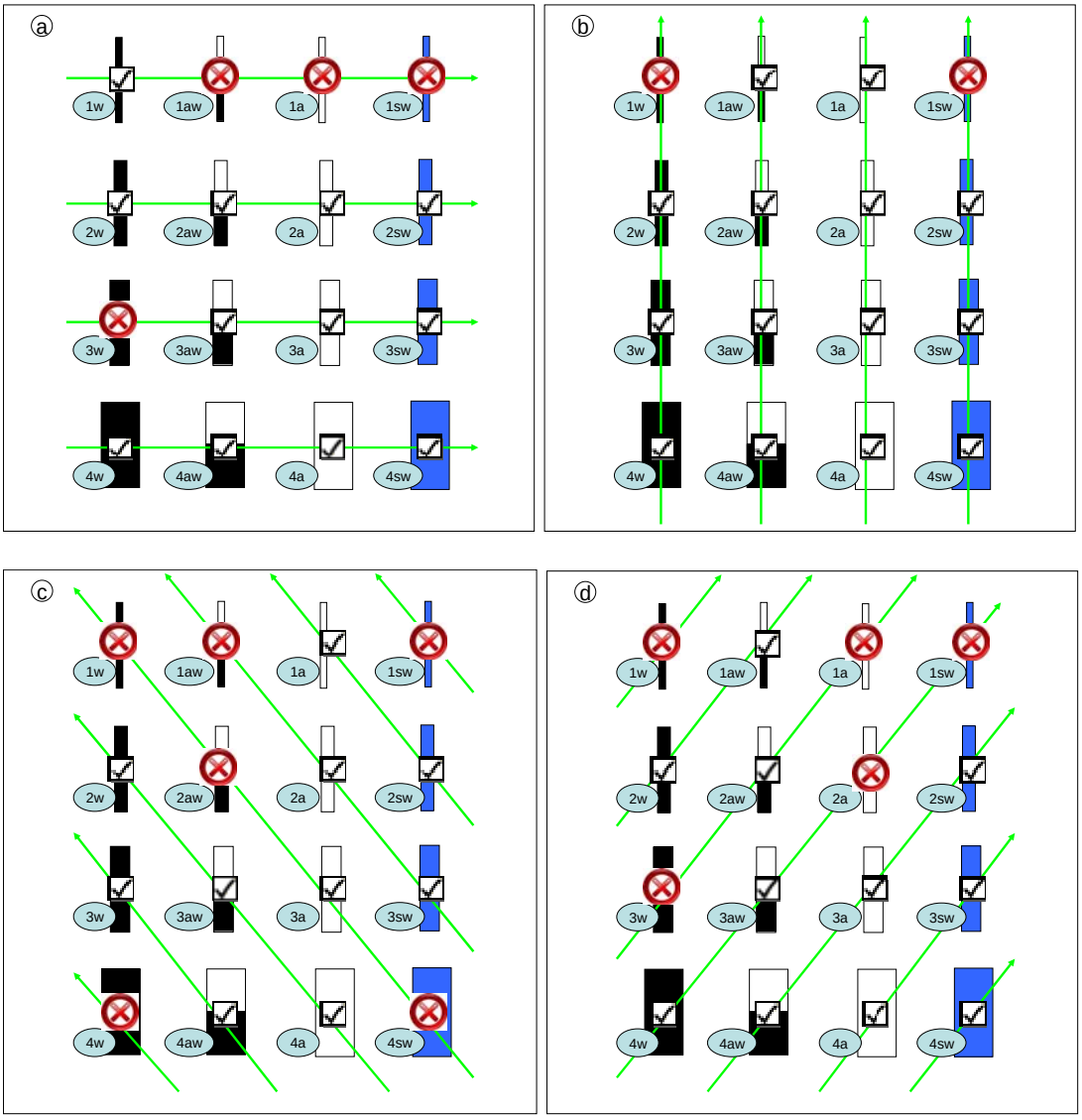

Figure 25. Experiment I auto-detection results by scan line orientation: a) perpendicular intersection, b) parallel intersection, c) right-to-left angled intersection, and d) left-to-right angled intersection. Check marks indicated the pipe was detected, X's indicated the pipe was not detected.

3.8 Conclusion

GPR detection methodologies were developed that effectively detected a variety of PVC pipes buried within a meter of the ground surface. The manual procedure had a high detection rate (92.2%) and low false alarm rate (0%) in the relatively uncluttered silt-loam test plot soil. Positions and depths were successfully predicted regardless of the scan orientation for pipes bigger than 0.5 NPS.

Position estimate errors (mean P_e from the reflection apex = 11.1 cm**,** standard deviation = 8.0 cm) were generally higher than the depth errors (mean D_e from the reflection apex = -0.6 cm, standard deviation = 1.8 cm). There are at least two reasons for this disparity. First, the truth target positions (P_t) should not be referenced from the center of the antenna housing. It should be referenced from a point offset from the center at a distance roughly equal to the median error observed for the perpendicular scan line intersections (3.4 cm). Secondly, most of the higher position errors occurred with angled scan line intersections, indicating the presence of sensor squint where the radar beam is angled off the center axis.

The manual detection results provided rough bounds for sensor resolution in the Turfgrass Research Facility soils. The minimum resolvable object size across all target orientations relative to the scan lines was the inner diameter of the 1.0 NPS pipe (3.00 cm) given that 0.5 NPS pipes 1aw, 1w, and 1sw were not detected in the angled scan lines. This agrees very well with estimates based on wavelength at the upper bound of the antenna's bandwidth (3.1 cm). The resolution for the perpendicular intersections was better (all 0.5 NPS pipes, ID = 1.85 cm, were detected), as expected, but a lower limit could not be determined. This finding affirms

the importance of establishing GPR scan line grids to increase the likelihood of intersecting targets at a perpendicular angle.

The spatial resolution of two adjacent interfaces could not be determined. In theory, the top and bottom of an object would need to be separated by a distance exceeding one wavelength at the upper bound of the bandwidth (6.2 cm). No pipe had a reflection with completely separable responses from the top and bottom, but 4w (2.0 NPS with OD 6.03 cm and ID 5.64 cm) did have reflections in the perpendicular and angled scan lines that resembled the barely resolved case in Fig. 10 (waveform F).

The manual detection procedure had a higher true positive rate than that of the automated detection algorithm, AGTD (92.2% to 70.3%). This was primarily due to the superior abilities of the human brain to analyze features in images but also to shortcomings in the algorithm's design. Detection performance could potentially be improved by employing adaptive amplitude thresholding techniques based on gray-level histograms (Otsu, 1979; Yang and Gupta, 1993), more robust segmentation techniques (Malik et al., 2001; Pal and Pal, 1993; Svensson, 2008), or an iterative methodology (Dell'Acqua et al., 2004; Goldman and Cohen, 2004).

Chapter 4: Experiment II Detection and Mapping Test

4.1 Introduction

Experiment II was conducted as the second step towards developing generalized field procedures for detecting and mapping the structure of riparian wetland lateral preferential flow channels. The detection methodologies developed in Experiment I were applied to locate buried PVC pipes connected to simulate branching flow channels and a novel algorithm named the Macropore Morphology Mapping Algorithm (M^3A) was developed to predict the shape of that branching structure from the resulting detections.

The goals of the experiment were to (1) assess the accuracy of the manual and automated detection methodologies for locating the positions of the buried branching pipe structure, (2) develop a technique to extrapolate the structure of targets using a convolution operation, (3) develop an automated procedure (M^3A) to predict the three-dimensional structure of buried targets by linking detections of those targets across scan lines, and (4) qualitatively assess the effectiveness of M^3A by applying the algorithm to map the structure of the buried pipes.

Experiment II included:

1. Creating a field test plot of buried PVC pipe targets arranged in a branching structure;
2. Collecting GPR data along 12 parallel scan lines oriented perpendicular to the trend of the pipe target structure;

3. Applying the manual and automated detection methodologies to identify the locations of the pipe targets;
4. Assessing the detection results of the manual and automated detection methodologies using performance metrics including Type I and Type II error rates;
5. Developing a visualization technique to extrapolate the target structure using a convolution operation;
6. Developing an automated mapping procedure (M^3A) to link a set of target detections into a three-dimensional structure; and
7. Assessing the results of the mapping procedure with qualitative comparisons of the predictions to the true buried pipe structure.

4.2 Description of Experimental Site

A study plot was established in November 2007 at the UMD Paint Branch Turfgrass Research Facility in College Park, MD. Air-filled pipes were buried in a network with multiple bifurcating segments extending from a single source (Fig. 26). The design incorporated features from schematics of manually mapped preferential flow channels (Holden et al., 2002; Sidle et al., 2000; Sidle et al., 2001; Terajima et al., 2000). Schedule 40 pipes with sizes ranging between 0.5 and 2.0 NPS were buried in trenches at depths between 8 and 33 cm (Fig. 27). Excavated soil was hand packed into the trenches under and around each pipe.

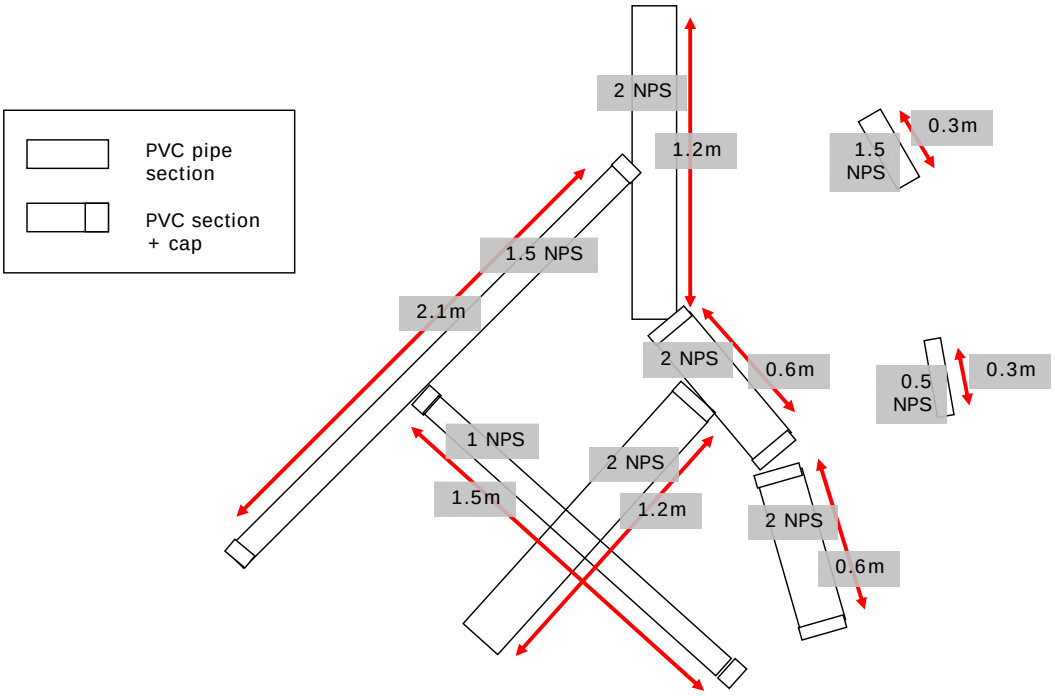

Figure 26. Schematic of the Experiment II pipe layout showing the size (NPS = nominal pipe size) and length of each PVC section.

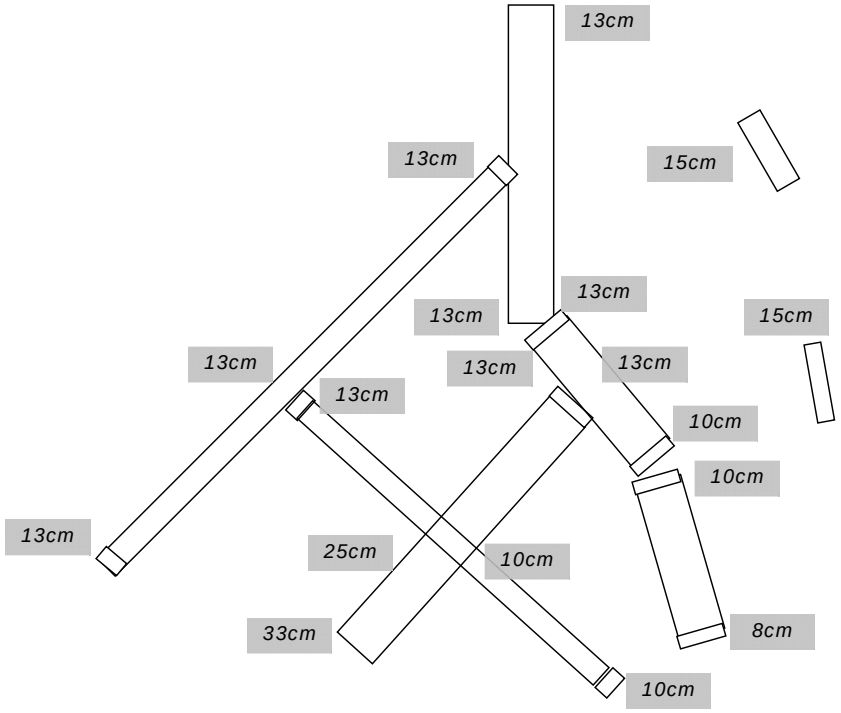

Figure 27. Experiment II pipe layout depths measured at junction points and segment end points from the top of the pipe to the ground surface.

4.3 GPR Data Collection

GPR data were collected in November 2007 along parallel scan lines laid out perpendicular to the central axis of the pipe structure (Fig. 28). The same calibration settings were used as in Experiment I. During data collection, the true pipe locations within each scan were noted by triggering electronic markers that were saved with each of the B-scans data files. The data were marked each time the center of the antenna housing was directly above a pipe.

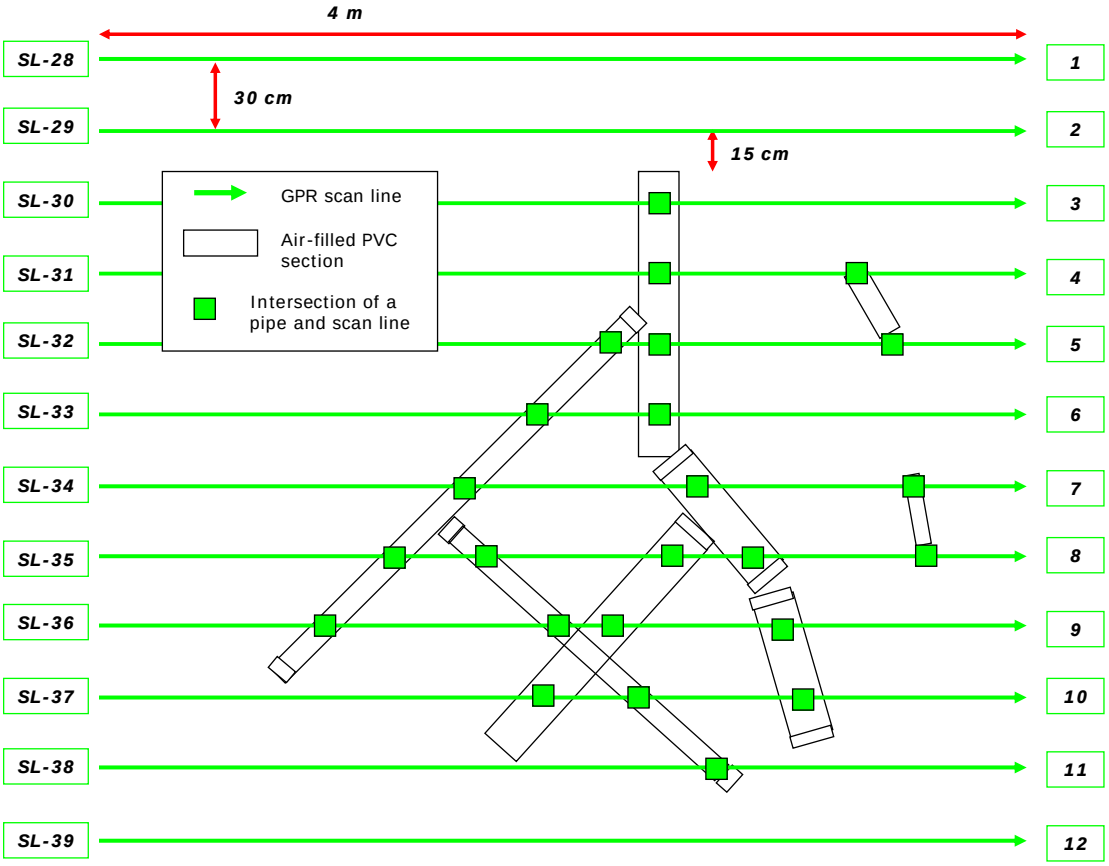

Figure 28. Schematic of the 12 Experiment II GPR scan lines (SL-28 thru SL-39). The scan lines were parallel, equally-spaced, and oriented perpendicular to the trend of the structure. Truth locations within the B-scans are annotated as squares at the intersections of scan lines and pipe segments.

4.4 GPR Data Analysis and Detection Accuracy Assessment Methods

Data from each scan line were analyzed using the manual and automated procedures developed in Experiment I to detect reflections from pipes.

The accuracy of the detection model was assessed as in Experiment I by calculating (1) the numbers of valid detections and dismissals as well as Type I and Type II errors and (2) position and depth prediction errors.

4.5 Target Structure Extrapolation Method Using a Convolution

Prior to mapping the detections into a three dimensional structure, an intermediate visualization technique was developed to extrapolate the shape of the pipe structure. The visualization used a convolution operation with structuring elements (shape templates) to project the form of the pipe layout from the set of detections.

Convolutions are used in a variety of image processing applications. It is a mathematical operation defined as the integral of the product of two functions (f, g) after one is reversed and shifted:

$$Y = f * g \qquad [4\text{-}1]$$

The two-dimensional form (i.e., for a plane of scan lines, n_1, and positions, n_2) is:

$$Y(n_1, n_2) = \sum_{m_1=-\infty}^{\infty} \sum_{m_2=-\infty}^{\infty} f(m_1, m_2) g(n_1 - m_1, n_2 - m_2) \qquad [4\text{-}2]$$

The depth dimension of the manually identified detections was eliminated, leaving a plane of detection data the length and width of the study site. Using Eq. [4-

2], the detection plane was convolved with three shape templates (SE1, SE2, and SE3): straight lines that were perpendicular to the scan grid (SE1), and rotated 45˚ (SE2) and -45˚ (SE3). The lines were 0.9 scan lines long and 3 cm wide. By matching the templates to the true orientation of the pipes with respect to the scan lines, the convolution operation extrapolated the shape of the pipe segments from the set of location predictions on the detection plane.

4.6 Target Structure Mapping – M^3A

An algorithm I have named the Macropore Morphology Mapping Algorithm (M^3A) was created to map subsurface target structures using the results of the GPR scan data analysis and nearest neighbor association rules. The computer algorithm automatically links a set of target detections into a three-dimensional structure of connected linear segments.

4.6.1 Mapping Algorithm Definition

The algorithm connects detections from one scan line to the next by comparing their locations within the scan lines. Connections are made between detections separated by distances (in position and depth) under specified thresholds using a coding device called an "extrapolation box." A data structure for the macropore connectivity (*MP*) is maintained with pointers between connected detections.

The algorithm was designed based on the following assumptions: (1) GPR data was collected along scan lines that formed a discrete grid across the study area, (2) the scan lines were sufficiently closely spaced to adequately sample the

subsurface morphology and allow for nearest neighbor connections of detections from one scan line to the next (as the spacing increases, the accuracy of the nearest neighbor predictions decreases exponentially), (3) the detections from the scan analysis procedure corresponded to the targeted subsurface structures (i.e., minimal Type I error), and (4) the scan analysis resulted in a nearly complete set of detections for the structure (i.e., minimal Type II error).

Each detection on each scan line is considered in turn (Fig. 29). Potential matches of detections to existing *MP* segments are evaluated by checking whether the detection falls within the extrapolations of those *MP* to the current scan line. If no match is found, a new *MP* is initialized with the detection as the root node. If a match is found, the detection is connected as a branch to that *MP*. If multiple matches are found, the detection is connected to the *MP* with the best fit according to a nearest neighbor principle. After all detections on the scan line are considered, extrapolation boxes are created on the next available scan line for all the active *MP* branches. After all scan lines are completed, suggestions are made to close gaps between *MP* segments due to false dismissals in the analysis. The connectivity links are used in plotting functions to construct a visualization of the target structures.

Additional detail and extension to a circular scan line layout is given in Appendix C.

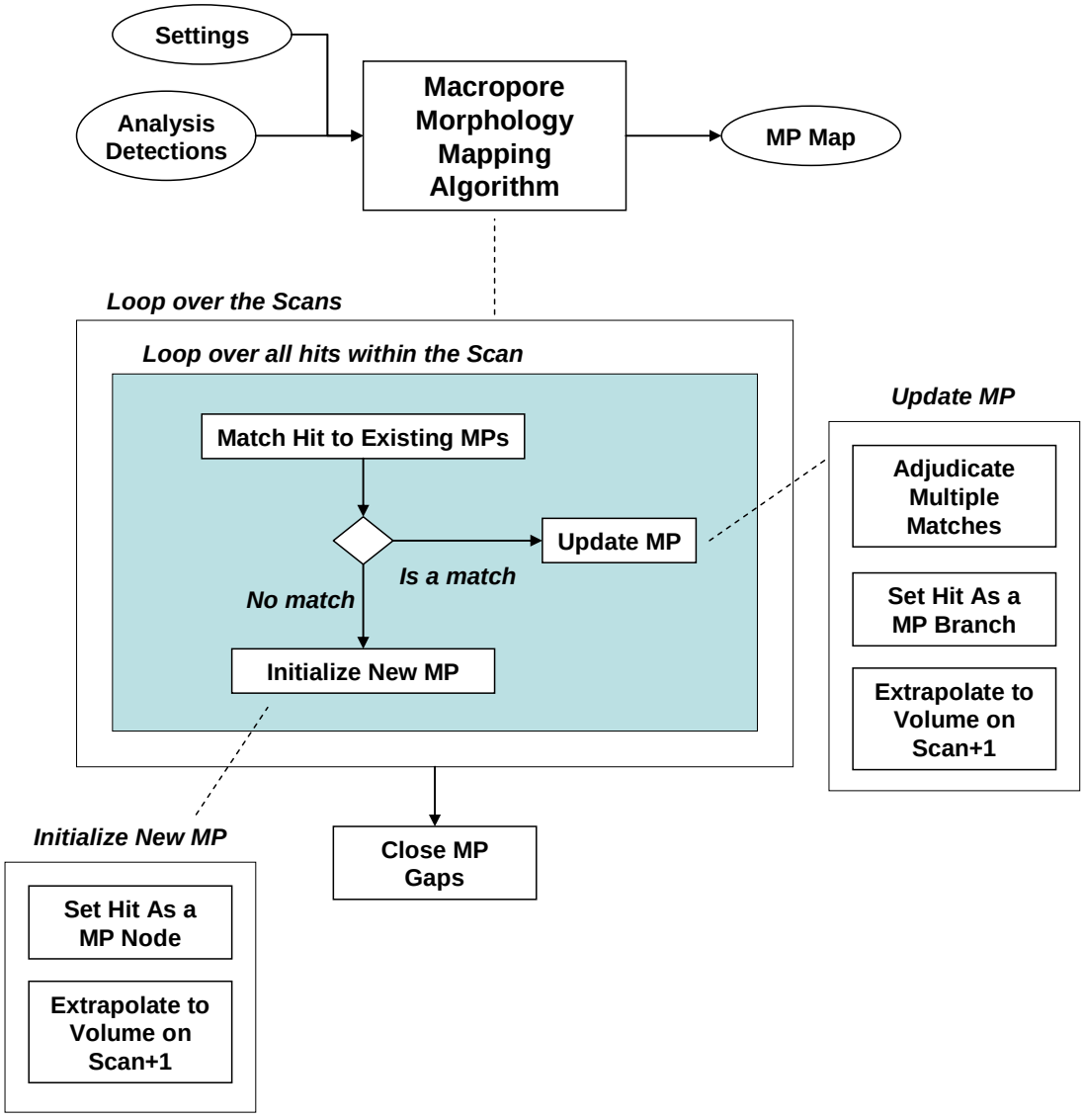

Figure 29. Macropore Morphology Mapping Algorithm (M^3A) for predicting the connectivity between target detections.

4.6.2 M^{3}A Application Example

A hypothetical target structure is used to demonstrate the algorithm's basic functionality. The simulated example (Fig. 30) has two channels scanned with three parallel equally-spaced scan lines (SL-0, SL-1, and SL-2). Perfect detection performance is assumed prior to applying M^{3}A, so the mapping procedure operated on the set of seven intersections of scan lines with channels (Fig. 31).

The algorithm considers the scan line detection data starting with SL-0 and ending at SL-2. At the beginning of the analysis, there are no *MP*s so there are no possible matches for the SL-0 detections. Therefore, they are set as root nodes of two new *MP*s, MP1 and MP2 (Fig. 32). Extrapolation volumes are projected outward from the SL-0 nodes onto SL-1 (Fig. 33). The two SL-1 detections fall into these extrapolation boxes and are associated to their respective MPs (D3 to MP1 and D4 to MP2). Similarly, extrapolation volumes are projected from the SL-1 node positions onto SL-2 and the three SL-2 detections are associated (Fig. 34). Two are associated as branches of MP1 (D5 and D6) and the nearest neighbor tie-breaking logic is employed to associate D7 to MP2 (it falls within both the MP1 and MP2 extrapolations but is closer to MP2). The final predicted links (Fig. 35) are:

MP1 = D1 → D3 → D5, D6

MP2 = D2 → D4 → D7

The predicted target map (Fig. 36) generally matches the middle extents of the two simulated targets. Small errors in the prediction are due to the scan line spacing, including the beginning and ending of segments that fall outside of the scan grid and the position of the true branching point of channel 1 between SL-1 and SL-2.

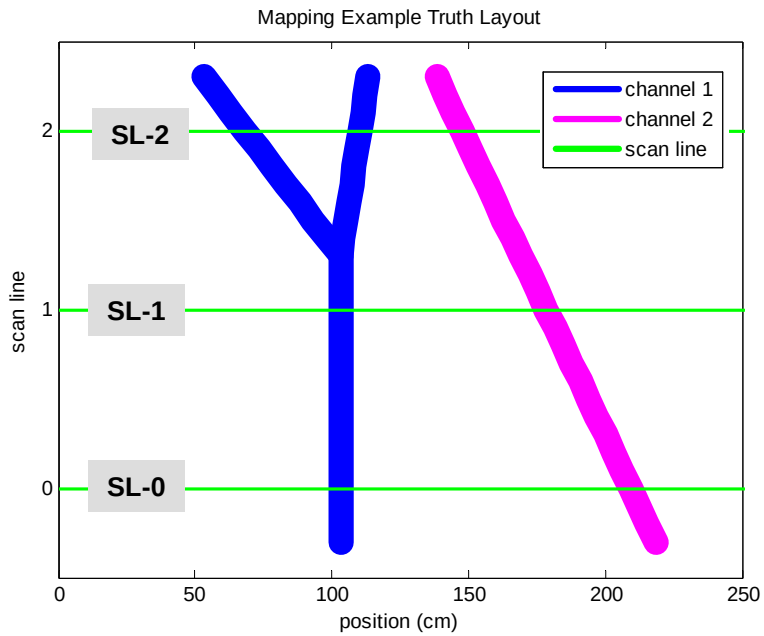

Figure 30. Morphology mapping algorithm example. A simulated subsurface structure is scanned with three parallel B-scan lines (SL-0, SL-1, SL-2).

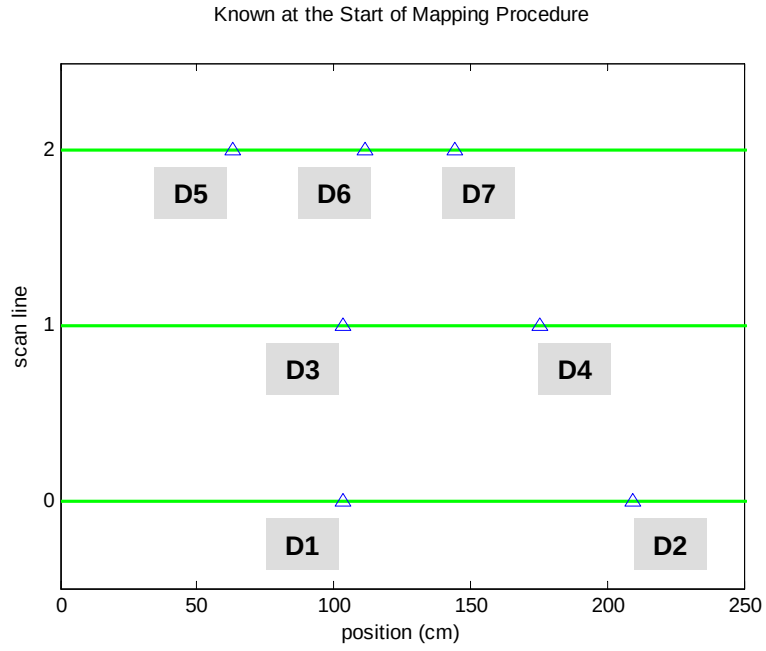

Figure 31. Known information at the start of the mapping procedure: 7 detections (D1-D7) on the three scan lines (perfect detection performance is assumed).

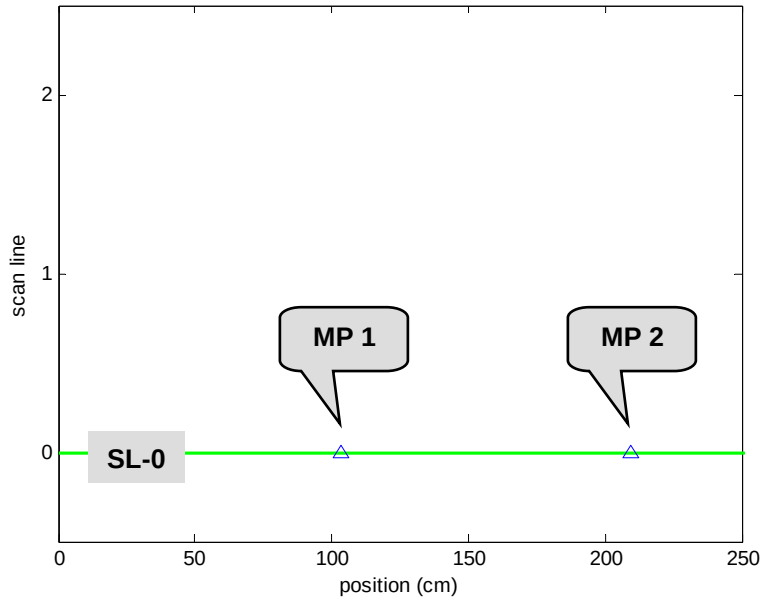

Figure 32. Mapping algorithm application starting with scan line 0 (SL-0). Each SL-0 detection was initialized as the first node of an MP.

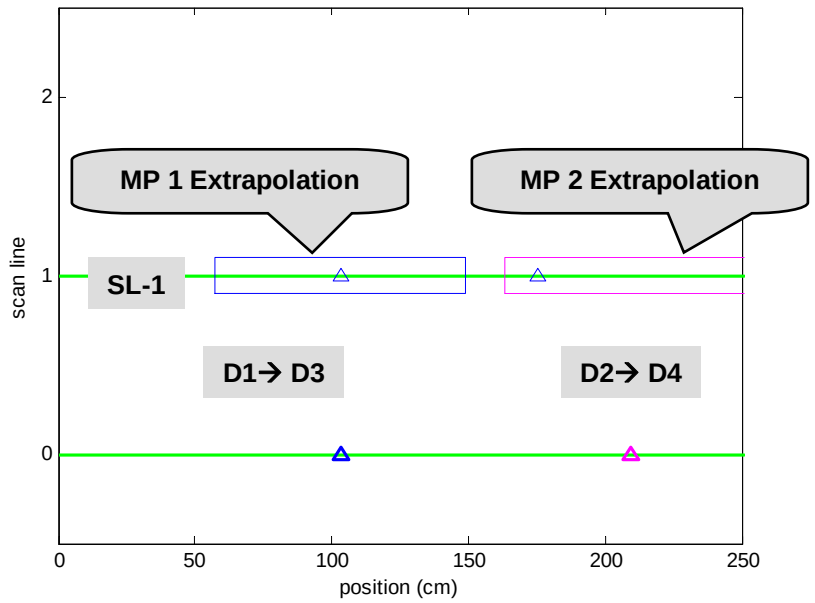

Figure 33. Mapping algorithm application on scan line 1 (SL-1). Extrapolation volumes were projected to SL-1 based on SL-0 information and SL-1 detections were matched to the extrapolations.

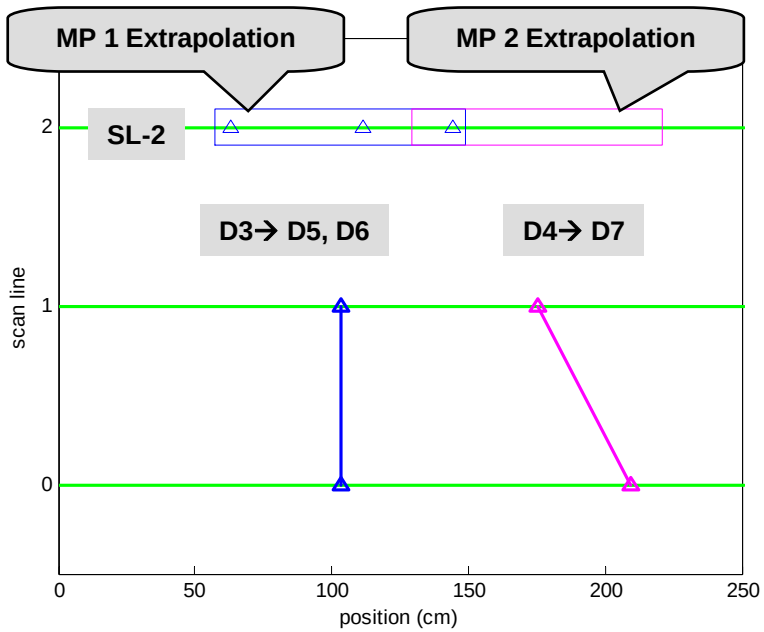

Figure 34. Mapping algorithm application on scan line 2 (SL-2). Extrapolation volumes were projected to SL-2 based on SL-1 information and SL-2 detections were matched to the extrapolations.

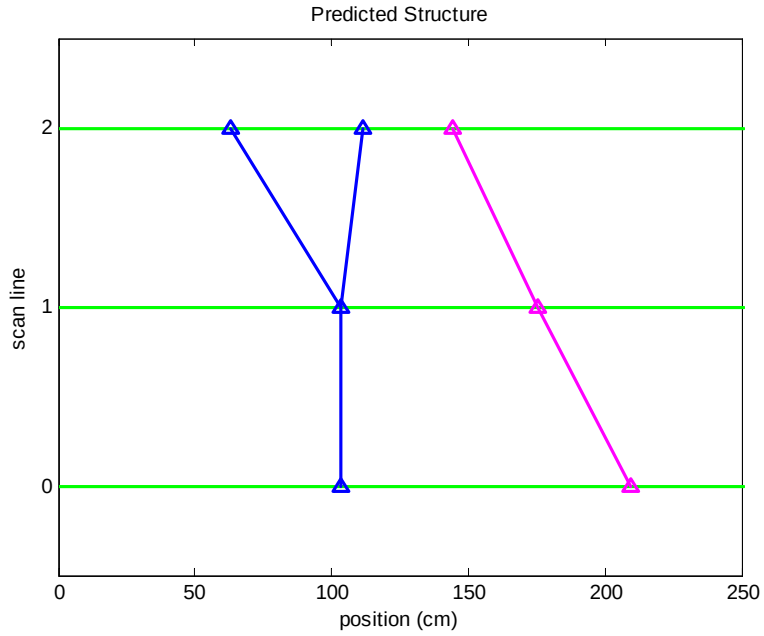

Figure 35. Mapping algorithm example structure prediction.

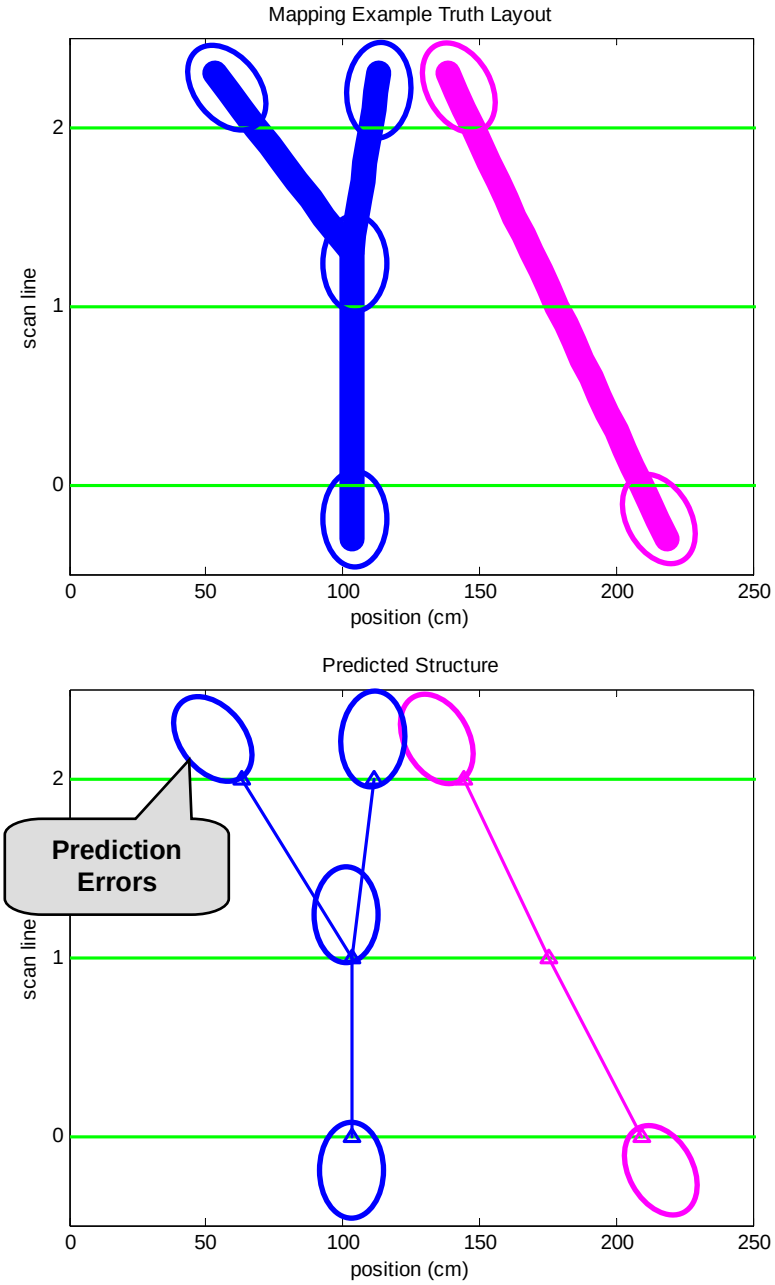

Figure 36. Mapping algorithm example prediction compared to the original truth layout. Prediction errors are noted with the circles.

4.7 Results

4.7.1 Target Detection Accuracy

4.7.1.1 Detection Error Rates

The results of the accuracy assessment for the manual and automated detection methods are summarized in Table 6. The 12 scan lines were assumed to have intersected the pipe structure 24 times ($p = 24$). Using the manual methodology (Fig. 37), 22 of the assumed intersections were detected ($d_M = 22$) with no false alarms ($fa_M = 0$). The two ends of the pipes on the right side of the site (on SL-32 and SL-35) were not detected, probably because the antenna did not actually pass over the pipe segments. Thus, the Type II errors were likely due to the antenna placement during data collection not the detection methodology. The automated procedure had more errors than the manual procedure. Using AGTD, 17 of the assumed intersections were detected ($d_A = 17$) with two false alarms ($fa_A = 2$). As in Experiment I, the false alarms were within 5 cm of the soil surface which can probably be attributed to artifacts generated from disturbing the soil matrix to bury the pipes. Of the 1210 detection grid cells across the 12 scan lines, 1186 did not contain truth pipe positions (ngc = 1210-24 = 1186). The complete set of scan data and results is given in Appendix D.

Table 6. Experiment II manual and automated detection procedure results.

Metric	Manual Procedure	Automated Procedure
Total Grid Cells	1210	1210
Grid Cells Not Containing Truth	1186	1186
Empty Grid Cells Predicted Empty	1186	1184
Potential Detections	24	24
Accurate Detections	22	17
False Alarms (Type I Errors)	0	2
Missed Detections (Type II Errors)	2	7
True Positive Rate	91.7%	70.8%
True Negative Rate	100.0%	99.8%
Type I Error Rate	0.0%	0.002%
Type II Error Rate	8.3%	29.2%
Precision	100.0%	89.5%
Total Accuracy	99.8%	99.3%

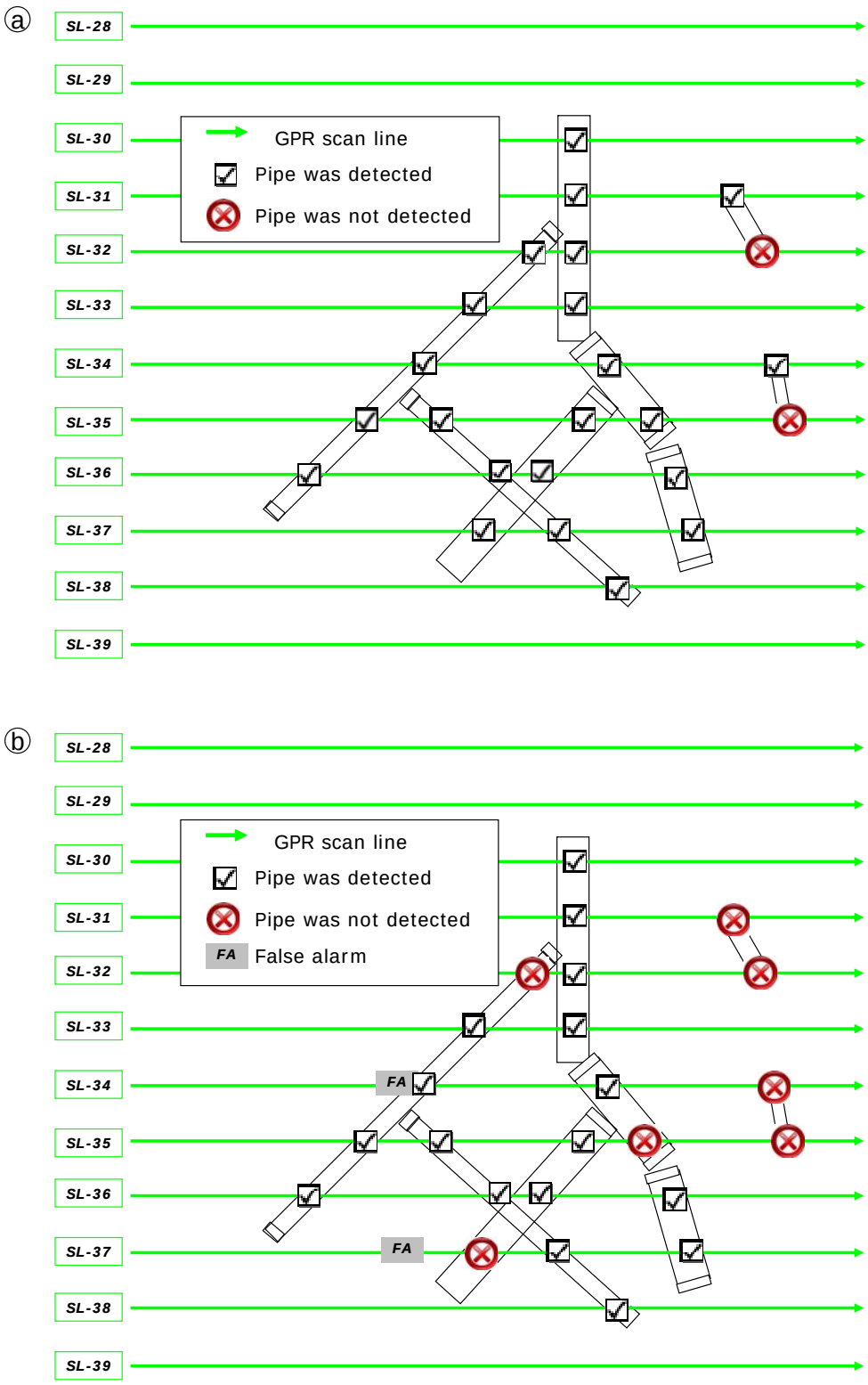

Figure 37. Detection performance relative to the Experiment II pipe layout using the (a) manual and (b) automated detection methodologies.

4.7.1.2 Position and Depth Prediction Errors

As in Experiment I, there was a tendency to over-estimate the pipe positions compared to the center of the antenna housing, especially for the angled pipe intersections (Fig. 38). The median position error (P_e) of the manual target detections for the perpendicular scan line intersections was 3.4 cm as compared to 8.6 cm for all angled intersections. The median depth error was 0 cm; estimates were generally accurate within 2 cm (23% of the wavelength at the antenna center frequency and 32% of the wavelength at the upper bound of the antenna frequency response).

4.7.2 Target Structure Extrapolation Using a Convolution

Two target structure shape extrapolations were created (Fig. 39 b, d) from the data plane of manually identified detections (Fig. 39 a, c) using the shape templates. The true pipe structure was best approximated by taking into account coarse information about the orientation of the pipes (Fig. 39 c). However, *a priori* knowledge of the angles of intersection is required, which is a major limitation.

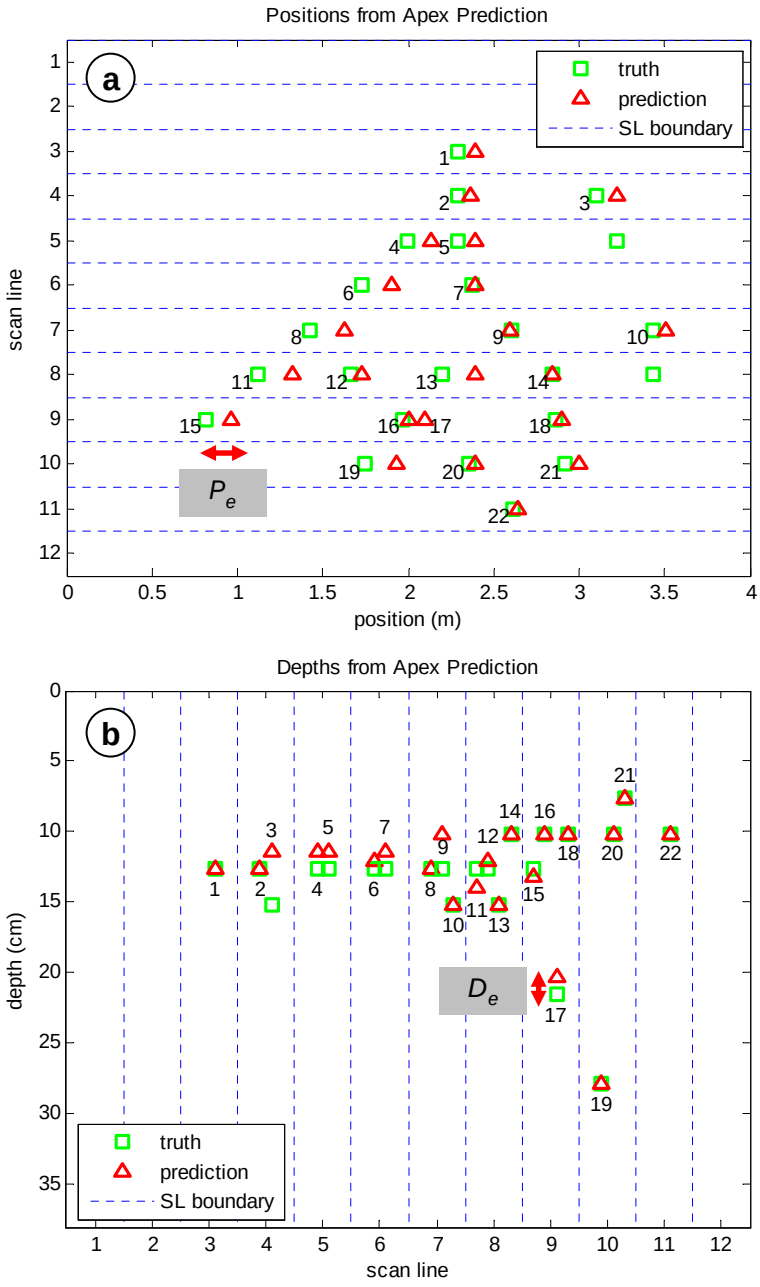

Figure 38. Truth and predicted (a) positions and (b) depths of the Experiment II buried pipe structure on each GPR scan line (mean P_e = 9.6 cm, standard deviation = 6.9 cm; mean D_e = -0.5 cm, standard deviation = 1.1 cm). Predictions were set with the manual detection procedure at the reflection hyperbola apexes. The detection number labels are consistent between the two plots.

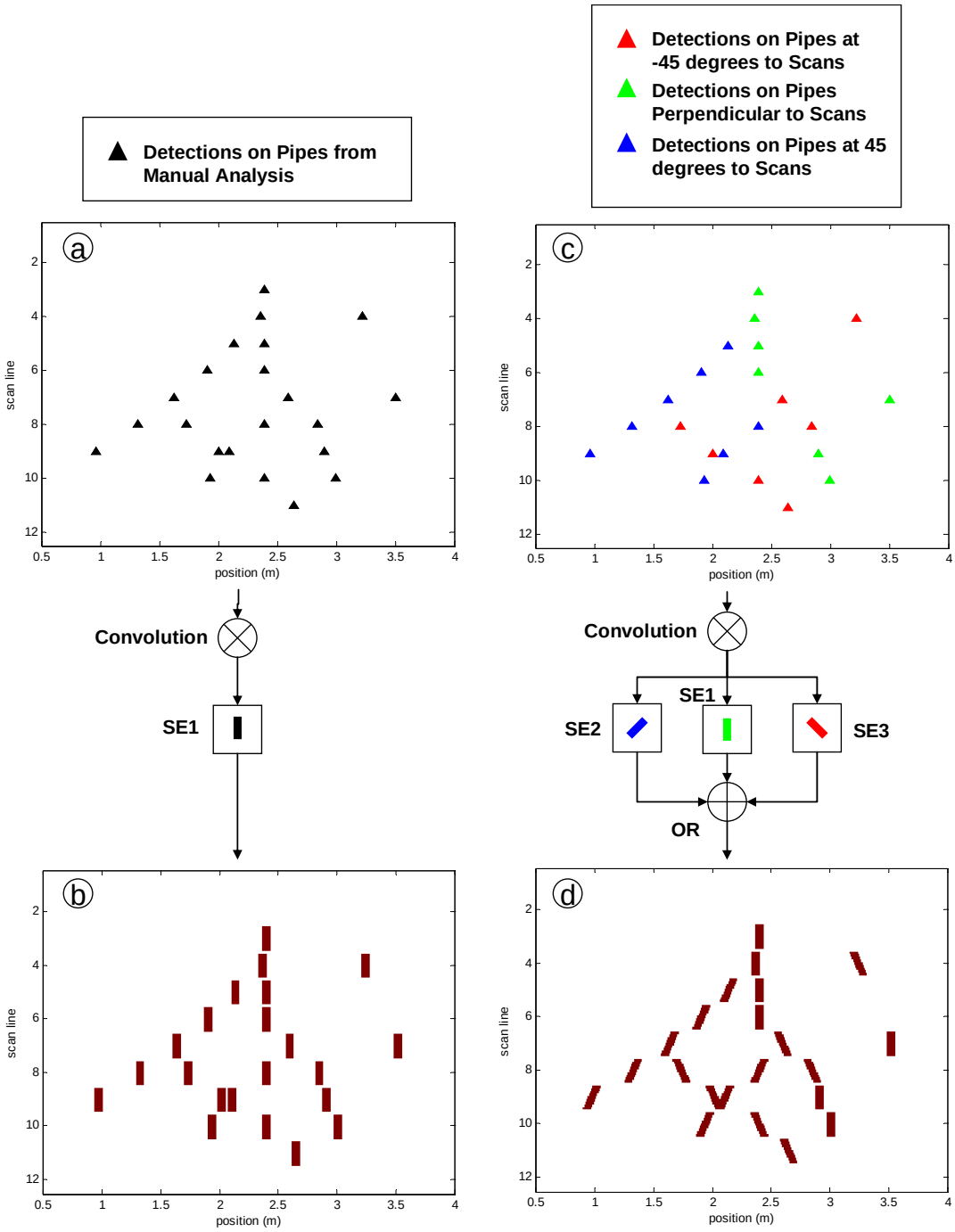

Figure 39. Experiment II convolution shape extrapolation. The input data were the set of manual detections (a) excluding and (c) including the truth pipe orientations. Convolutions were computed (b) using only the perpendicular mask (SE1) and (d) using three masks (SE2, SE1, and SE3) applied to detections of the same color.

4.7.3 Target Structure Mapping

Three *MP*s resulted from the application of M^{3}A to the detections from the manual analysis procedure (plotted blue, green, and red); the green and red *MP*s had only one node each (Fig. 40, 41). The prediction robustly tracked the truth structure as shown in plan view (Fig. 42).

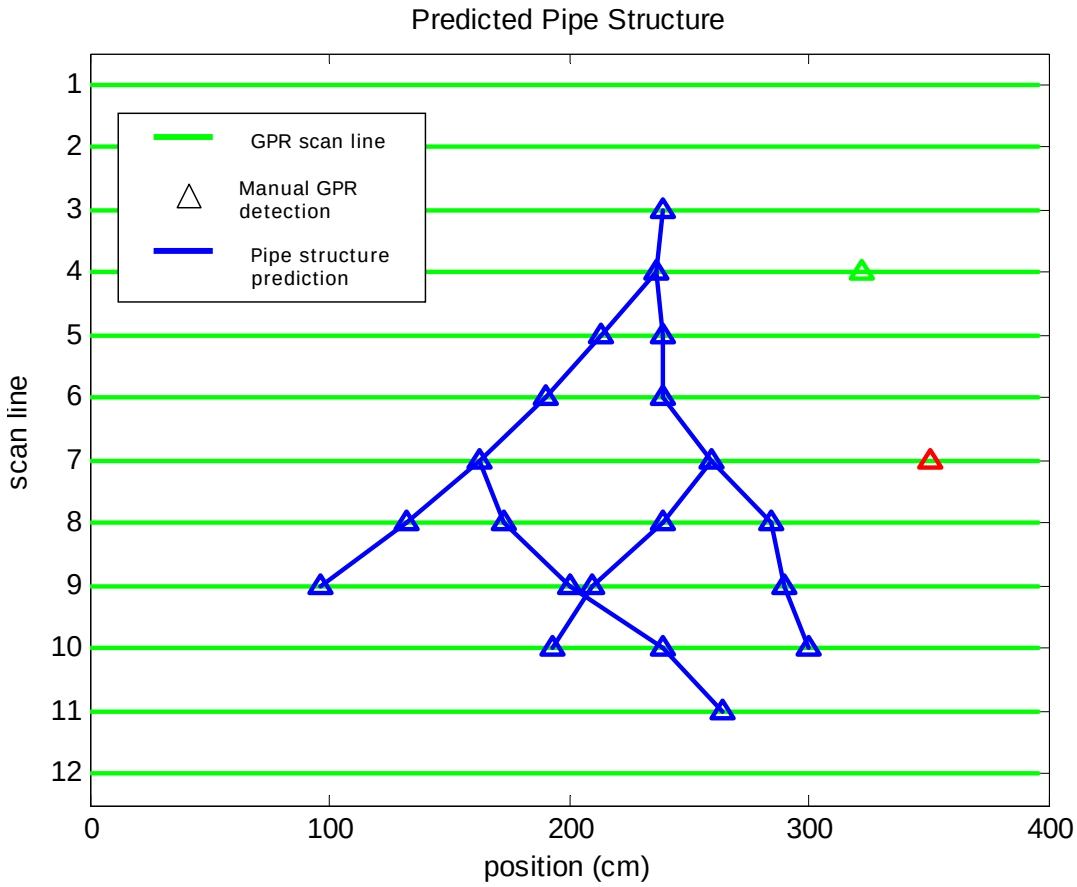

Figure 40. Diagram of the predicted Experiment II pipe structure using M^{3}A and the results of the manual target detection procedure. The green and red triangles are single node *MP*s (the detections were not associated to any others).

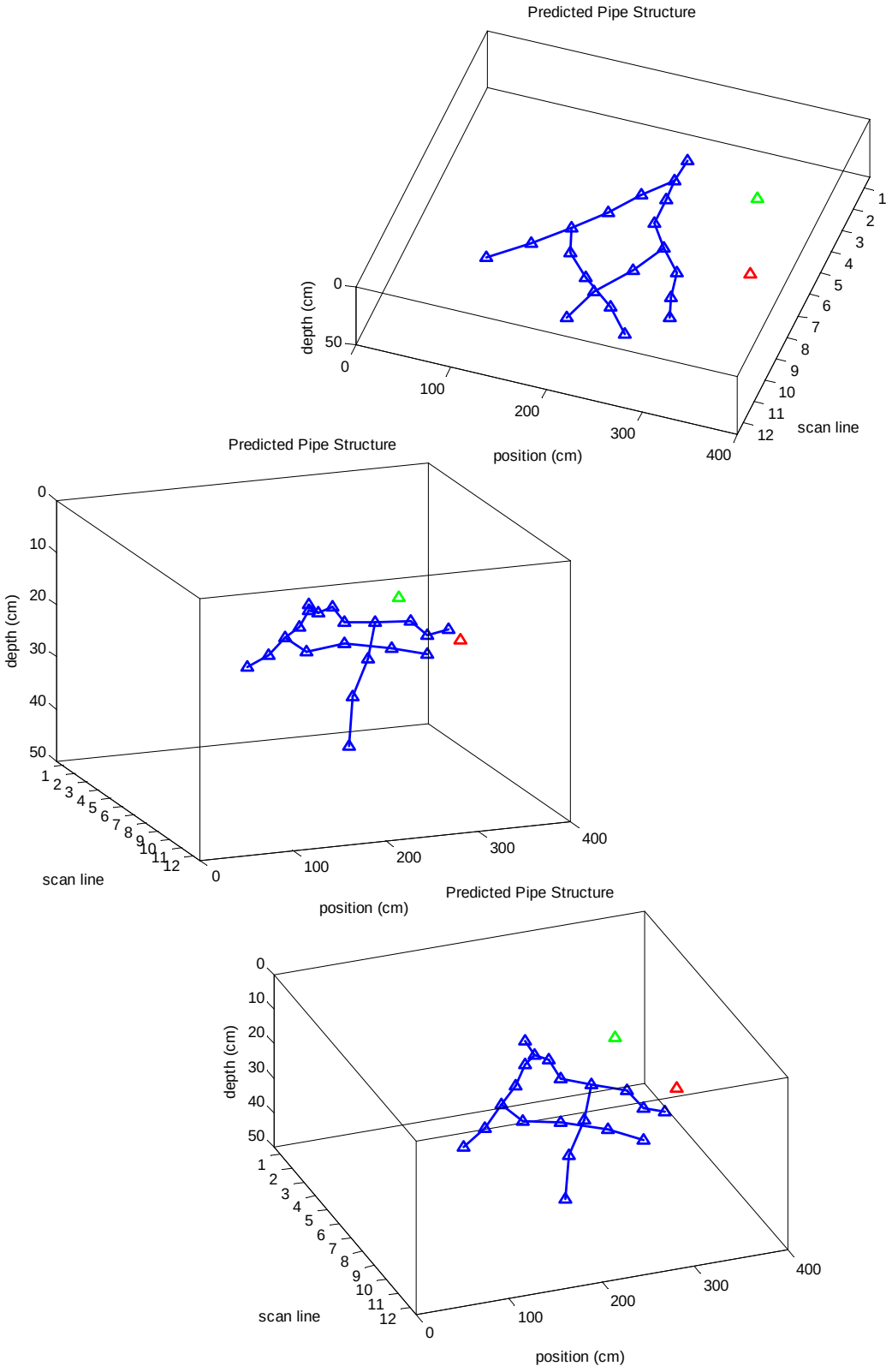

Figure 41. Three three-dimensional views of the predicted Experiment II layout.

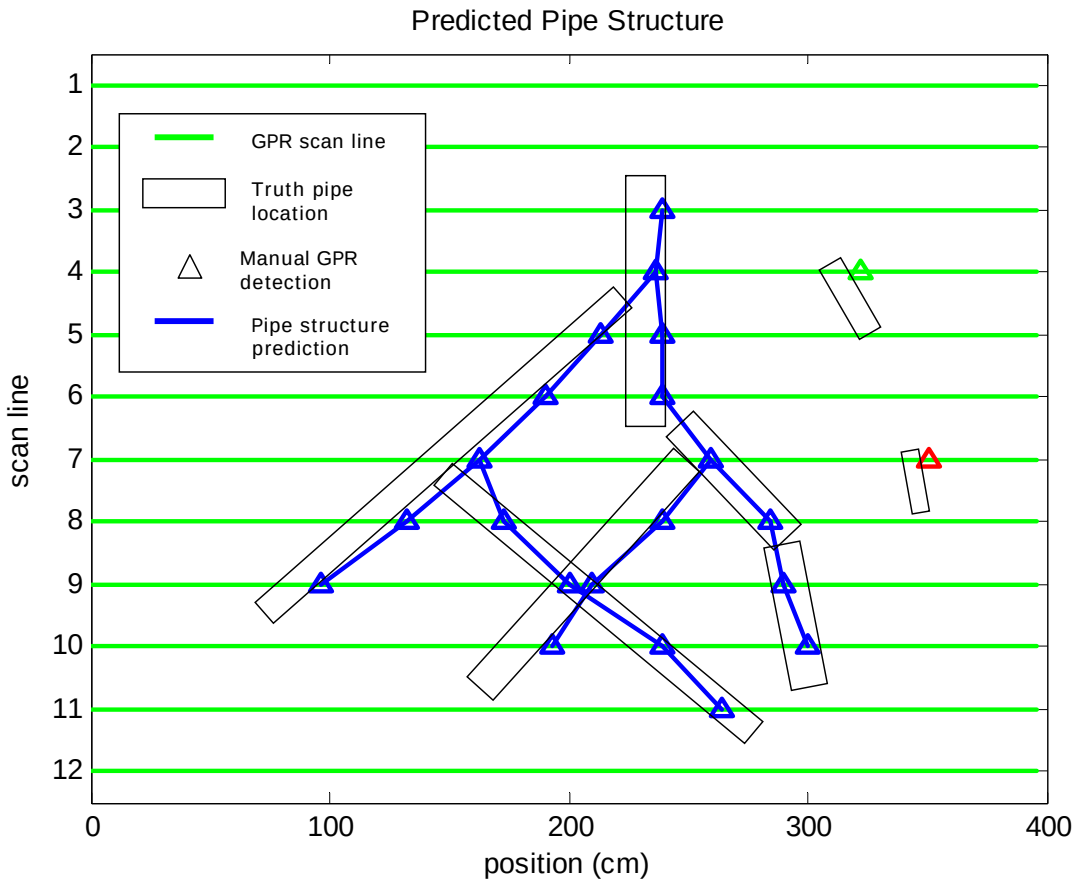

Figure 42. Plan view of the predicted Experiment II pipe structure compared to the truth layout.

4.8 Conclusion

An algorithm named M^3A was developed in Experiment II to automatically reconstruct the geometry of buried pipes simulating riparian wetland preferential flow channels within one meter of the soil surface. The algorithm robustly mapped the branching structure across 12 parallel GPR scan lines from detections generated using the methodologies developed in Experiment I.

The target detection accuracy assessment corroborated the results of Experiment I. Using the manual detection methodology, 91.7% of the pipes were correctly located (8.3% Type II error rate) with a 0% Type I error rate. The two missed detections were on scan lines assumed to have intersected structure end points, suggesting that the antenna did not actually pass by the pipes within the width of the GPR footprint. The median position prediction error (P_e) was 8.6 cm and the median depth prediction error (D_e) was 0 cm. Using the automated procedure, 70.8% of the pipes were correctly located (29.2% Type II error rate) with a 0.002% Type I error rate.

Chapter 5: Experiment III Mapping Validation

5.1 Introduction

Experiment III was conducted as the final step towards developing and validating generalized field procedures for detecting and mapping the structure of riparian wetland lateral preferential flow channels. The procedures developed in Experiments I and II were applied and validated at a study site in a riparian wetland. Preferential flow channels were detected along 10 scan lines covering the study area and the results were referenced by M^3A to create a three-dimensional map of the channel structures. The structure predictions were confirmed by ground truth generated from soil core samples and colored tracer dye transmission.

The goals of the experiment were to (1) use the GPR protocols developed in Experiments I and II to scan a wetland and detect the positions of preferential flow channels, (2) use the convolution operation developed in Experiment II to calculate the density of channel detections across the study area, (3) use the mapping algorithm developed in Experiment II (M^3A) to create a three-dimensional map of the flow channel structures based on the detection locations, and (4) ground truth the locations of the flow channels using colored tracer dye and auger core samples and assess the accuracy of the predictions.

Experiment III included:

1. Selecting a study site within a riparian wetland with known preferential flow;
2. Collecting GPR data along 10 parallel scan lines oriented perpendicular to the hypothesized trend of the preferential flow channel structures;

3. Applying the manual and automated detection methodologies to identify the locations of the preferential flow channels;
4. Mapping the subsurface structure of flow channels using M^3A;
5. Calculating the density of channel detections in the study area using the convolution operation; and
6. Assessing the accuracy of the detection and mapping procedures by ground truthing the locations of channels using core samples and by observing the rates of flow of injected tracer dyes through the study area.

5.2 OPE^3 Soils, Hydrology, and Vegetation

The validation experiment was performed at the USDA/ARS Beltsville Agricultural Research Center OPE^3 research site in a riparian wetland. The study site is located within an agricultural watershed in the mid-Atlantic coastal plain in Beltsville, MD (Fig. 43). About 75% of the 70 ha watershed is in agricultural production and 10% is forested wetland; the remainder is forested upland and uncropped meadow (Angier et al., 2005).

The riparian corridor borders a 1.1 km long first-order stream that runs northeast to southwest through the watershed. The corridor varies in width between 60 m and 250 m (Angier et al., 2005). Five automated data logging stations record flow measurements at intervals along the stream before it joins a higher-order stream at its southern terminus. (Fig. 44)

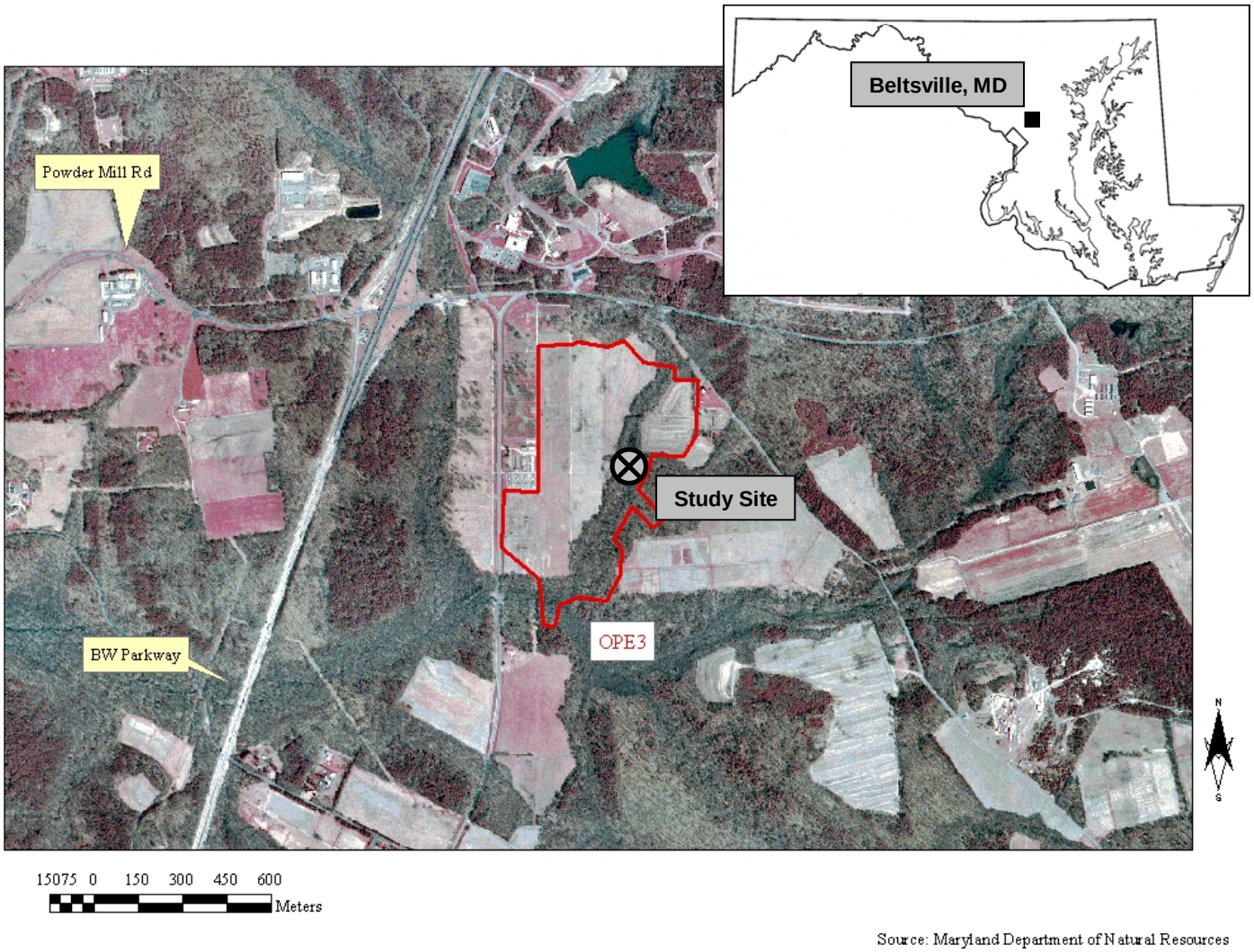

Figure 43. Color infrared photograph of the OPE^3 watershed and surrounding Beltsville, MD area (www.msgic.state.md.us).

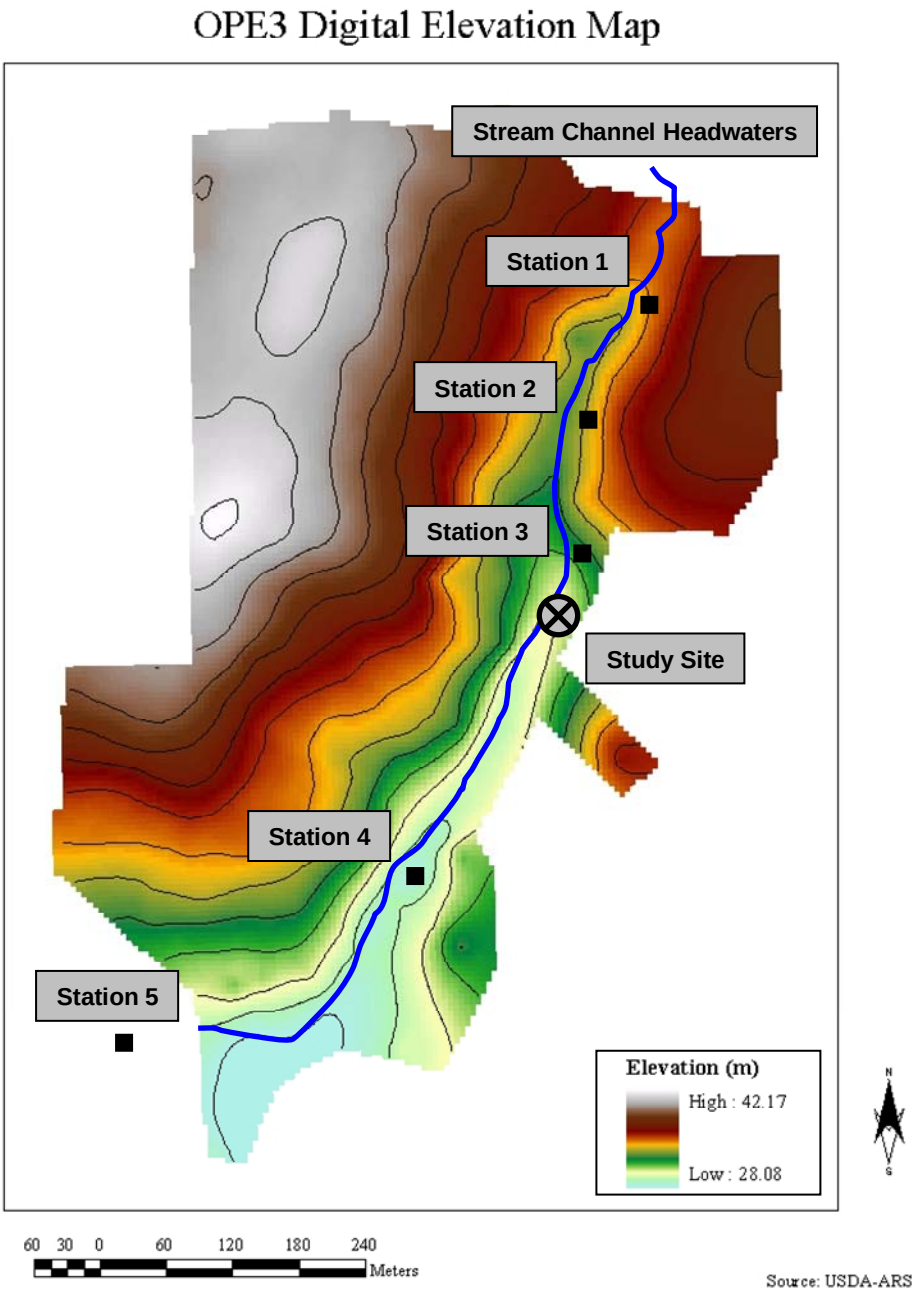

Figure 44. OPE[3] watershed digital elevation map with the location of the Experiment III study site.

The wetland soils at the site are approximately 2 m deep and classified as Typic Haplosaprist. They are underlain by a sand and gravel aquifer. The soil series in the northern part of the wetland is a Johnston Silt Loam (very poorly drained) and a Bibb Silt Loam (poorly drained) in the southern part (Angier et al., 2002). A "post-settlement" layer with greater mineral content is present within 50 cm of the surface; it was deposited when the land use in the region changed to agriculture (Angier and McCarty, 2008).

Indirect and direct evidence has been reported of preferential water conduction in the OPE^3 wetland. Many upwelling (discharging) zones are present throughout the riparian valley and actively discharging macropores are visible along the banks of the stream channel. Fine sands have also been observed discharging from those openings, the source of which was hypothesized to be a sand layer at least 80 cm below the surface. Finally, continuous macropores have been observed in soil cores (Angier et al., 2005).

The most prevalent tree species found within the riparian forest are red maple (*Acer rubrum*) and white oak (*Quercus alba*). Skunk cabbage (*Symplocarpus foetidus*) is the most prevalent understory species (Renz, 2003).

5.3 Description of Experimental Site

A 3 m by 5 m study site was established bordering the stream south of Station 3 (Fig. 44). This location was chosen because of its accessibility from the adjacent agricultural field (allowing transport of the GPR equipment), its relatively unobstructed surface, and its visible indicators of subsurface preferential flow (macropores on the stream channel wall actively conducting water).

5.4 GPR Data Collection

In March 2008, a rectangular grid of 10 scan lines was set with string bordering the stream (Fig. 45) and GPR data was collected. The scan lines were oriented parallel to the stream, perpendicular to the hypothesized trend direction of the channels: following the hillside slope as speculated in the alternative conceptual groundwater flow model (Angier and McCarty, 2008). The scan line spacing was set at the width of the sensor footprint (0.3 m) as in Experiment II. Propagation velocity was calibrated to synchronize the known depth of a metal stake inserted into the stream channel wall to the depth indicated in the real-time A-scan readout. During data collection, the locations of subsurface reflectors were noted from the computer display and flagged on the ground as potential sample locations for ground truth soil cores.

5.5 GPR Data Analysis and Target Structure Mapping Methods

Channel locations were predicted using the manual and automated detection procedures described in Experiments I and II. Reflected energy was disregarded in depths shallower than 15 cm because surface responses were likely caused by biomass like tree roots and skunk cabbage bulbs.

The connectivity of flow channels between scan lines was predicted using M^3A with the set of manual detections.

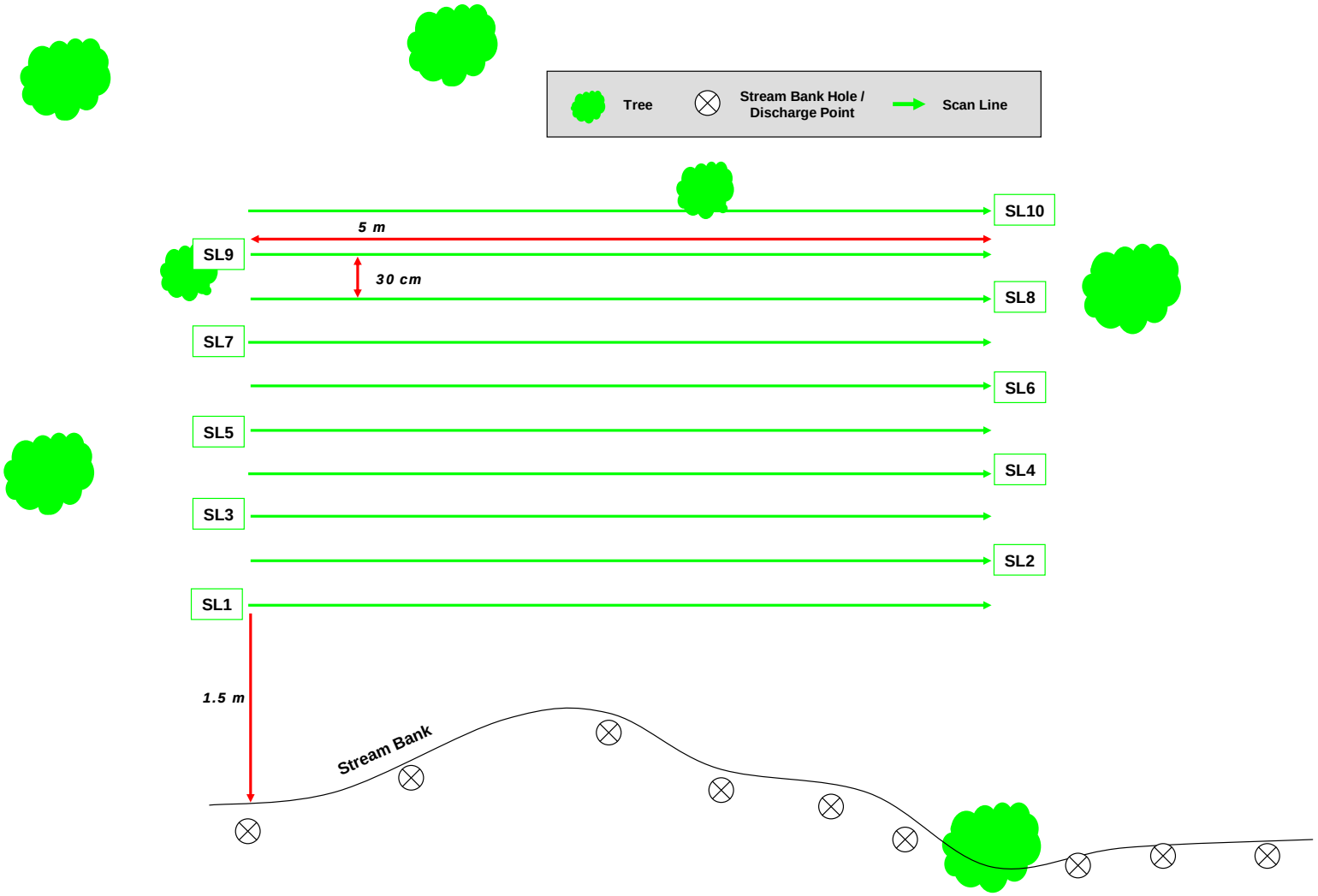

Figure 45. Experiment III study site schematic with rectangular scan line grid (SL1-SL10).

5.6 Target Detection Density Calculation Method

The two-dimensional convolution operation defined in Experiment II (Eq. [4-2]) was applied to calculate the density of detections within the study site. By convolving the plane of detections with a longer and thicker version of the perpendicular shape template (SE1), the detections in a neighborhood the size of the convolved shape template rectangle (2.9 scan lines long by 30 cm wide) were accumulated, providing a count, or density, of the detections in that neighborhood.

5.7 Ground Truthing Methods

The accuracy of the preferential flow channel location predictions was assessed by evaluating soil core samples and by observing the direction of preferential water conduction in the study site using colored tracer dye.

5.7.1 Soil Coring

Soil cores were obtained in March 2008 using a core extractor (Eijkelkamp Peat Sampler, Eijkelkamp Agrisearch Equipment, Giesbeek, The Netherlands) to directly confirm predictions of the presence and absence of large pores in the subsurface. The peat sampler extracted 0.5 m increments of the low-bulk-density wetland soils intact with little compression, allowing detailed examination of the samples (Angier et al., 2005).

Co-located target and control samples were extracted in six groups throughout the site as directed by real-time GPR readouts. Target samples were taken at points where macropores were predicted to be present based on a response detected from GPR transmissions. Corresponding control samples were taken at neighboring

positions that did not exhibit a GPR response. The samples were visually inspected and classified as either positive or negative for the presence of large pores (gaps in the cores). Samples with gaps larger than 3 cm in diameter, the functional resolution of the 900 MHz antenna established in Experiments I and II, were classified positive. Samples with smaller or no gaps were classified negative.

The metrics defined in Chapter 3 were reinterpreted to summarize the soil core prediction performance:

$$truePositiveRate = \frac{pt}{t} \quad [5\text{-}1]$$

$$trueNegativeRate = \frac{nc}{c} \quad [5\text{-}2]$$

$$typeIErrorRate = \frac{nt}{t} \quad [5\text{-}3]$$

$$typeIIErrorRate = \frac{pc}{c} \quad [5\text{-}4]$$

$$precision = \frac{pt}{pt + nt} \quad [5\text{-}5]$$

$$totalAccuracy = \frac{pt + nc}{pt + nc + pc + nt} \quad [5\text{-}6]$$

where pt = number of positive target samples
nt = number of negative target samples (Type I error)
t = number of total target samples
pc = number of positive control samples (Type II error)
nc = number of negative control samples
c = number of control samples

5.7.2 Acceptance Sampling

Acceptance sampling, a statistical quality control assurance technique from the field of reliability engineering, was used to judge the overall acceptability of the GPR-based channel predictions from the core sample results. The technique was popularized by Dodge and Romig (1959) and originally applied by the U.S. military to test the acceptability of bullets produced during World War II.

Dodge reasoned that by testing a sample at random from a batch, a decision could be made to either accept or reject the entire batch. Therefore, acceptance sampling represents a compromise between exhaustive sampling and no sampling. It is used when testing is destructive and the cost of inspection is high, as is the case with core extraction. Military Standard 105E (Department of Defense, 1989) is the most recent version of the standard specifying this procedure.

The soil core sampling design was a "single sampling plan" where one sample (sample size n) was selected at random from the batch. Instead of a batch of product, the batch size in this case was the number of potential samples, the number of grid cells along all of the GPR scan lines. Each cell was 22.86 cm long (along the scan) as in Experiments I and II and covered the full depth range. The acceptability of the set of predictions as a whole (both the presence and absence of channels) was determined by comparing the number of misclassified samples (target samples that were negative and control samples that were positive out of n total) to a threshold (the maximum number allowed was c). Standard 105E specifies values for n and c based on the batch size and three parameters: Acceptable Quality Level (AQL), inspection level, and inspection type.

AQL is the maximal percent of nonconforming cores allowed. Values of 1.0% or 2.5% are typical. Inspection level is either I, II, or III where Level II is designated normal, Level I requires about half the amount of inspection as Level II and is used when reduced sampling costs are required and a lower level of discrimination can be tolerated, and Level III requires about twice the amount of inspection as Level II and is used when more discrimination is needed. There are three types of inspection: normal, tightened, and reduced which allows for smaller sample sizes.

The parameters specified for this analysis were: AQL = 2.5%, inspection Level II, and reduced inspection type. To accept the batch of 220 GPR-based predictions (the total number of grid cells across the 10 scan lines), the standard dictates that 12 of 13 soil core samples be correctly classified (Table 7).

Table 7. Military Standard 105E acceptance sampling specifications for the soil core samples (Department of Defense, 1989, Table II-C).

Parameter	Specification
Batch size	151-280
Inspection Level	II
AQL	2.5%
Inspection Type	reduced
Sample Size (*n*)	13
Acceptance Threshold (*c*)	1

Thirteen cores (7 target samples and 6 control samples) were extracted in six groups (Fig. 46) below the surface root mat to a maximum depth of 67 cm (+/- 4 cm).

5.7.3 Tracer Dye

To confirm preferential flow through the study site, blue and red water tracing dyes (Cole-Parmer Instrument Company, Vernon Hills, IL) were injected into the subsurface in November 2004 at six locations in and around the study area (Fig. 46). Preferential flow (if any) from those input points was confirmed when the dye appeared in the stream channel within five minutes, far more rapidly than one would expect from typical rates of groundwater flow. The direction of flow was inferred based on the straight line connection of the inputs and outputs.

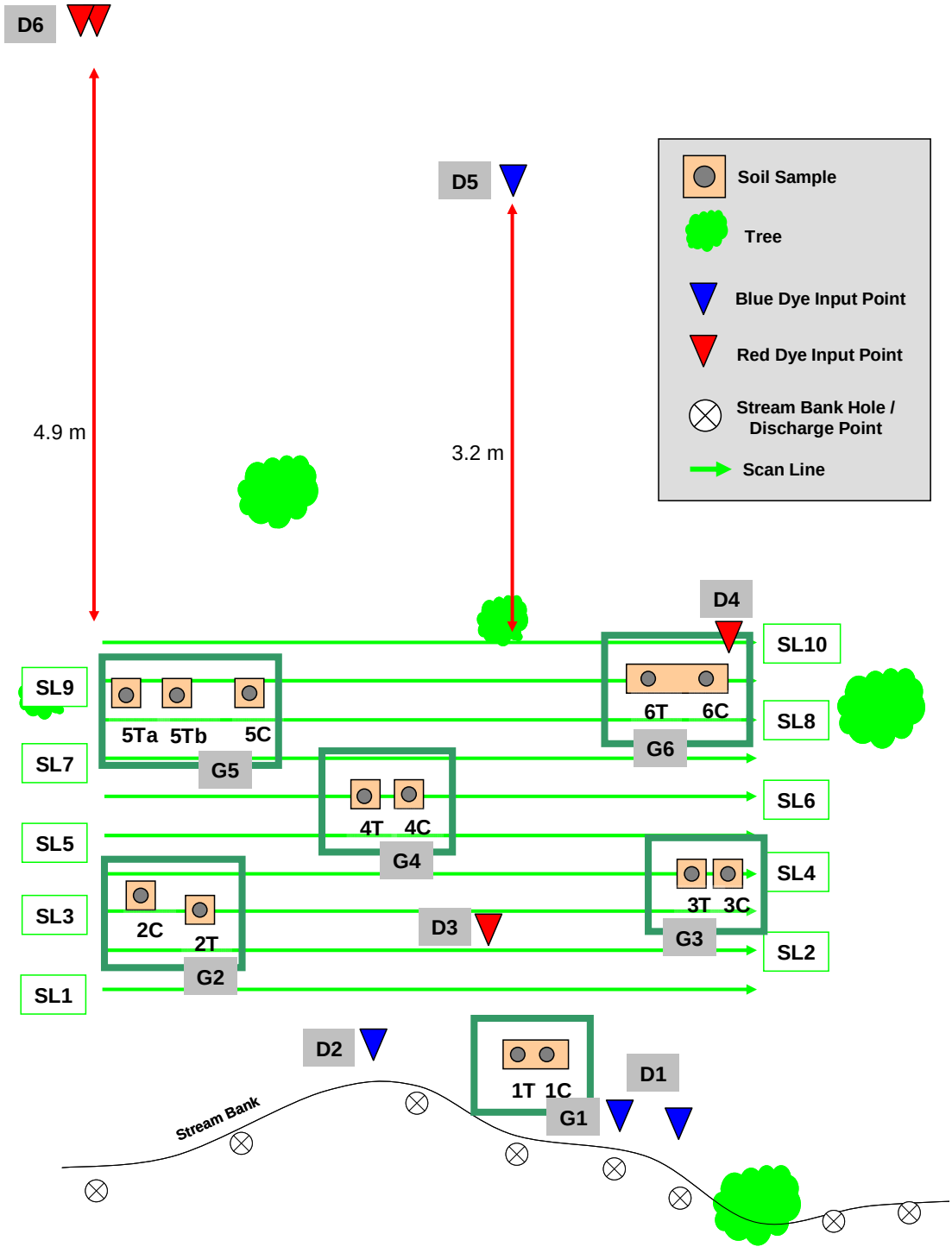

Figure 46. Experiment III study site schematic with the locations of the six groups of core samples (G1-G6) and six dye input points (D1-D6) relative to the grid of GPR scan lines (SL1-SL10).

5.8 Results

5.8.1 Target Detection

There were 450 total target detections across the 10 scan lines using the manual detection methodology. The complete set of scan data and detection results (including the automated methodology results) can be found in Appendix E. Constant bands of reflected energy were observed in the B-scan images (before background removal filtering) at approximately 38 cm and 55 cm. These bands were probably the result of changes in electromagnetic properties between soil layers that are evident in the soil cores. Refer to Appendix F for further examination of this correlation.

The numbers of detections and the character of the radar energy reflections varied within and between these soil strata. The bimodal distribution of manual detections in depth corresponded to the soil layer boundaries (Fig. 47). The shape of the reflections in the deeper depth ranges was also markedly different from those in the shallowest range.

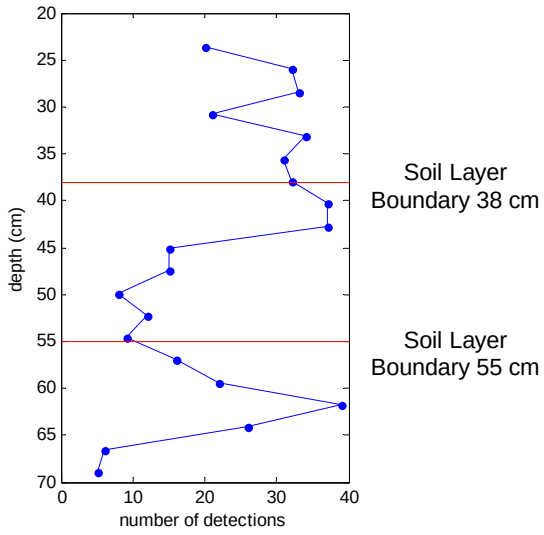

Figure 47. Distribution of detections in depth across all 10 Experiment III scan lines.

The distribution of detections was potentially due to the OPE^3 soils: the middle strata may be less permeable and thus inhibit the formation of channels, whereas the shallower and deeper layers appeared to be less cohesive and thus may be more susceptible to channel formation. The detections at deeper depths may also correspond to vertical upwelling pathways between the aquifer and the shallow subsurface as hypothesized by Angier et al. (2005).

5.8.2 Target Structure Mapping and Detection Density

The results of the connectivity prediction using M^3A and the detection density calculation in plan view are shown in Fig. 48. The M^3A results are also displayed in three dimensions in Fig. 49.

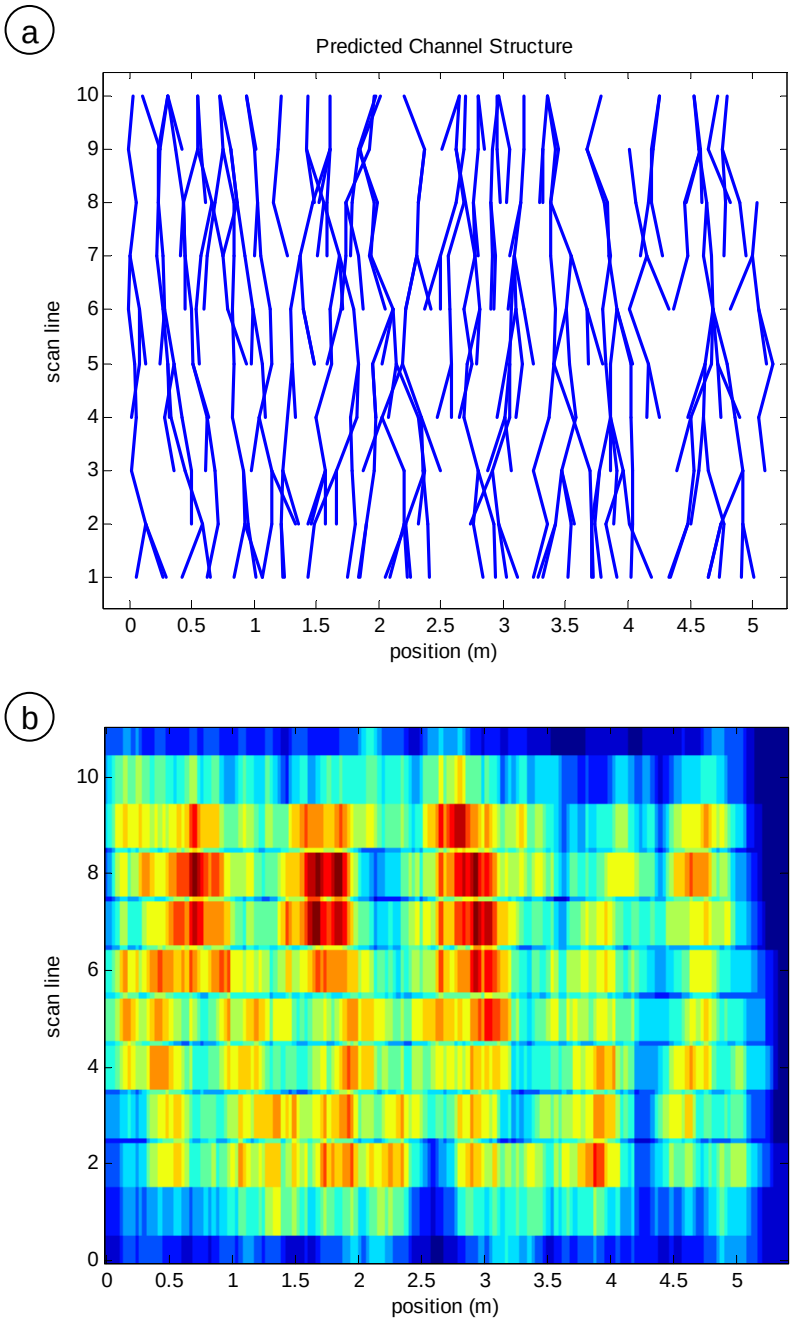

Figure 48. Experiment III M^3A preferential flow channel prediction (a) in plan view and (b) colorized detection density using the convolution operation where red stands for higher density and blue lower density.

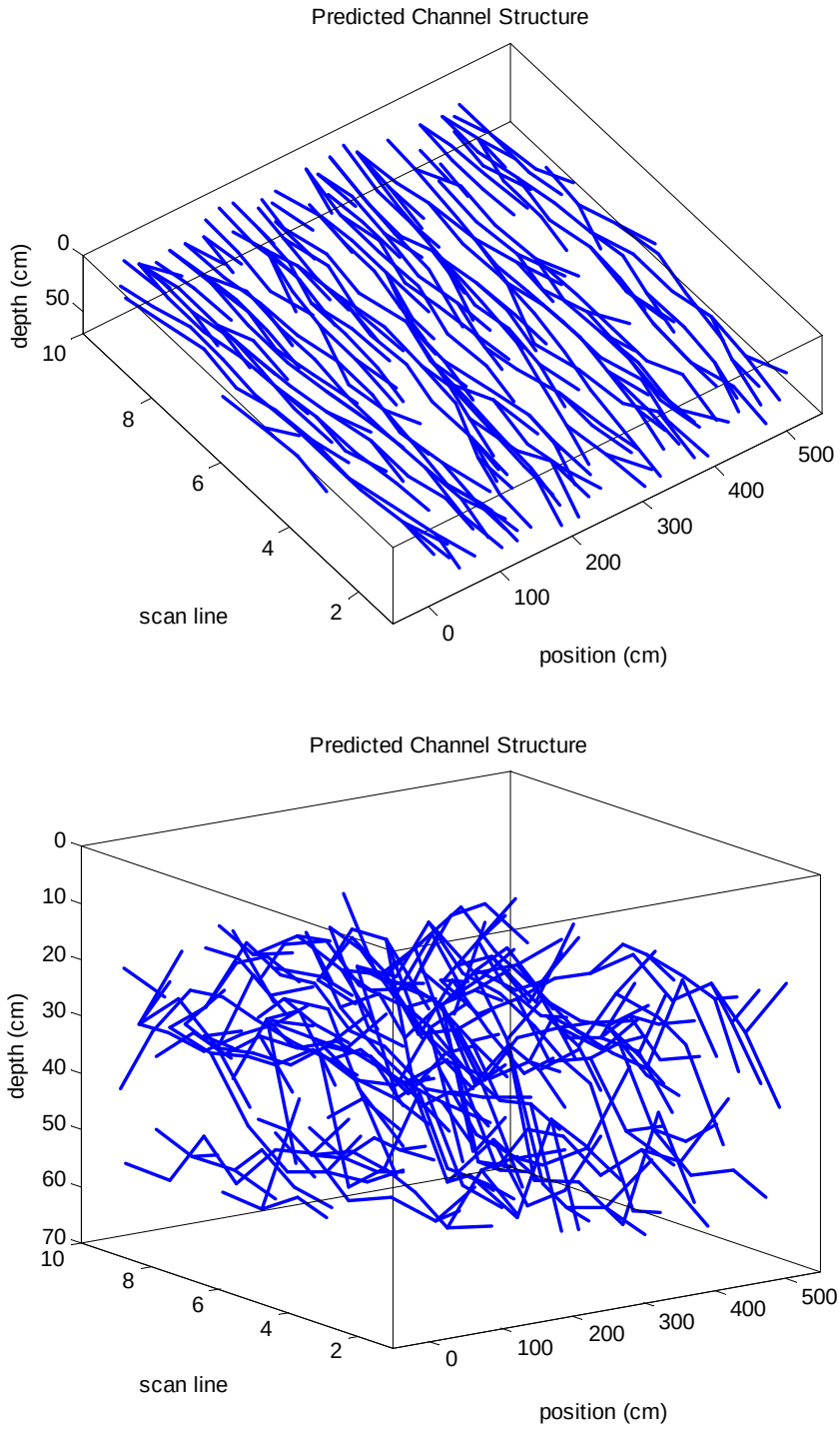

Figure 49. Two different three-dimensional views of the predicted channel structure.

5.8.3 Prediction Accuracy Assessment

5.8.3.1 Soil Coring

Six of the seven target cores had qualifying pore spaces (diameter > 3 cm) and were classified as positive samples (Table 8 and Fig. 50). All six control cores were classified negative resulting in a total accuracy 92.3%. Pictures of all the samples and expanded views showing the pore spaces are given in Appendix E.

Table 8. Experiment III core sample metrics (Eq. [5-1], [5-2], [5-3], [5-4], [5-5], and [5-6]).

Metric	Result
Total Samples	13
Target Samples	7
Positive Target Samples	6
Control Samples	6
Negative Control Samples	6
False Alarms (Type I Errors)	1
False Negatives (Type II Errors)	0
True Positive Rate	86%
True Negative Rate	100%
Type I Error Rate	14%
Type II Error Rate	0%
Precision	86%
Total Accuracy	92%

Target sample 3T did not contain qualifying pore spaces as predicted. This false alarm may have been due to the non-uniform bulk density at the predicted target depth (the soil was compressed and there appeared to be a small root present) or the core might have been taken at a position slightly offset from the true channel location.

The batch of GPR-based predictions meets the MIL-STD-105E acceptance qualification since only one sample was incorrectly classified.

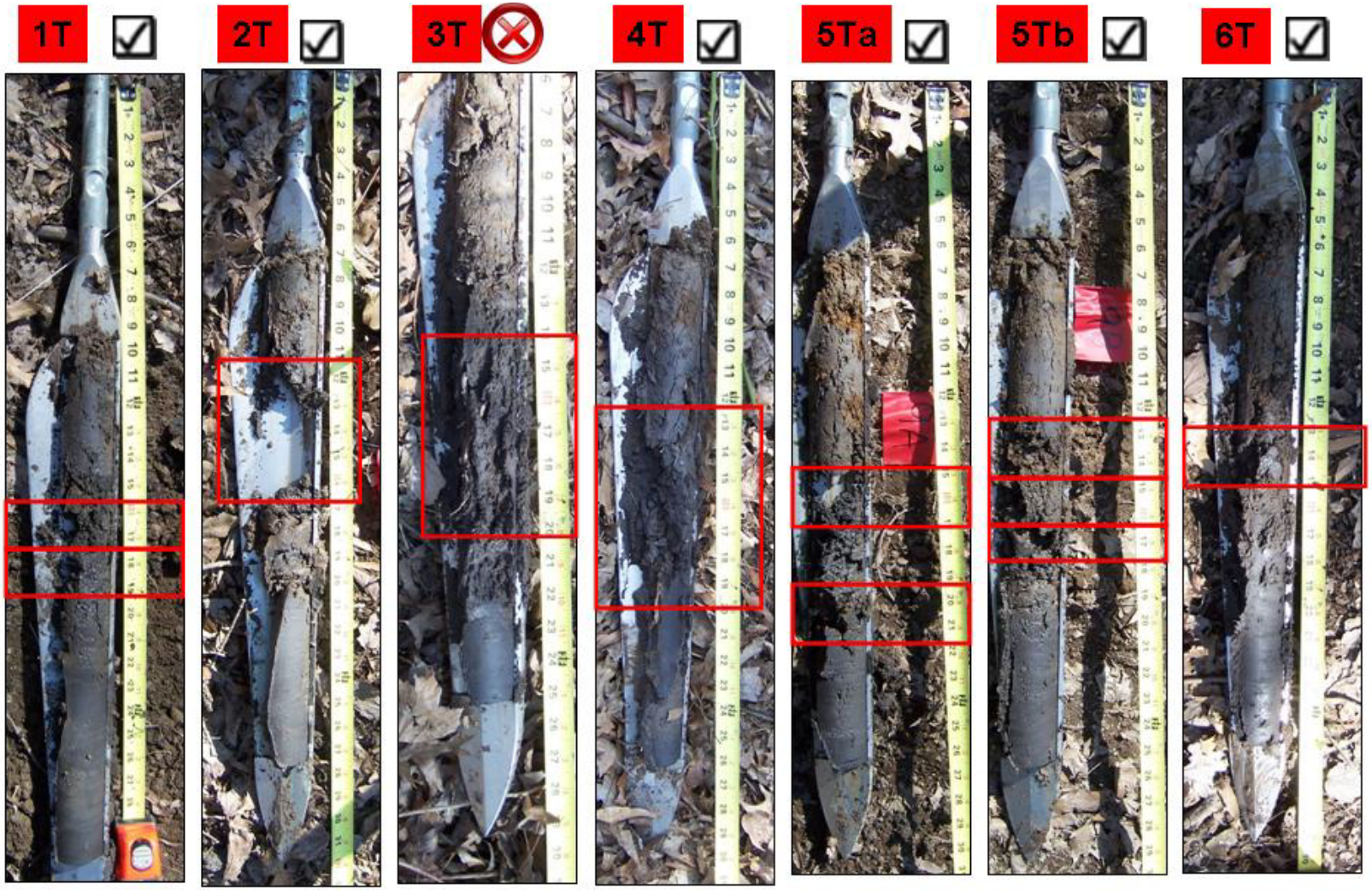

Figure 50. Target cores (1T, 2T, 3T, 4T, 5Ta, 5Tb, and 6T). Pore spaces or anomalies (3T) at the predicted depths are highlighted.

5.8.3.2 Tracer Dye

Observations of dye conducted from injection points to discharge points at the stream channel showed that preferential flow was active within the study site (Fig. 51). Four of the input points (D1, D3, D5, and D6) were connected to four different output points at the stream channel. Two other injection points did not have preferential transmission (D2, D4); note that D4 did not occur close to a predicted channel location (Fig. 52). The coarse extrapolations connecting inflow points to outflow points overlapped several of the predicted (and confirmed) target locations, leading to speculations about potential transmission paths through the site (Fig. 52).

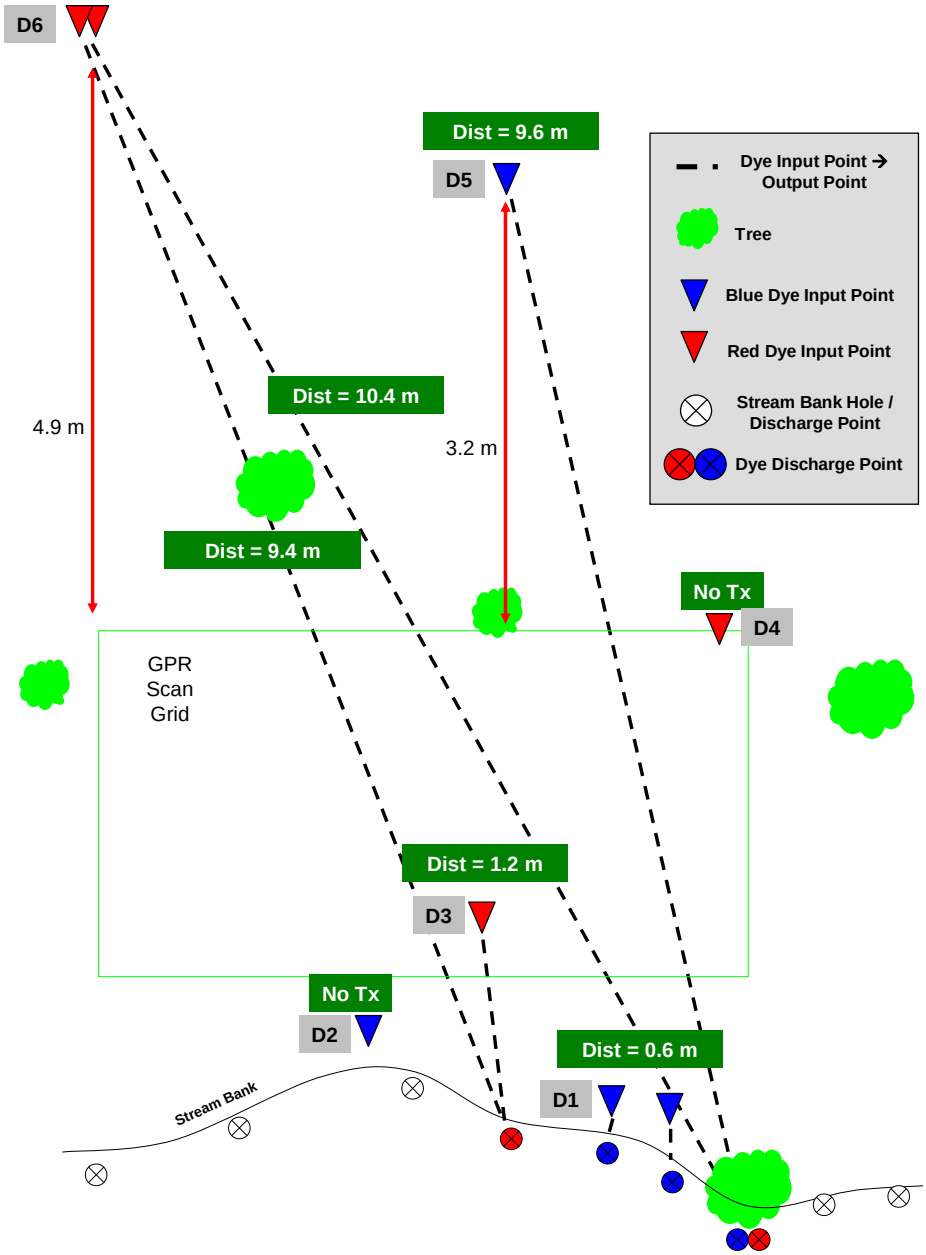

Figure 51. Colored dye injection points (D1-D6) and corresponding output points in OPE[3]. The dashed lines only connect the input and output points; the farther the distance from the stream bank, the greater the uncertainty about the actual path traveled through the study site. "No Tx" means no transmission was observed from this input point to the stream within five minutes.

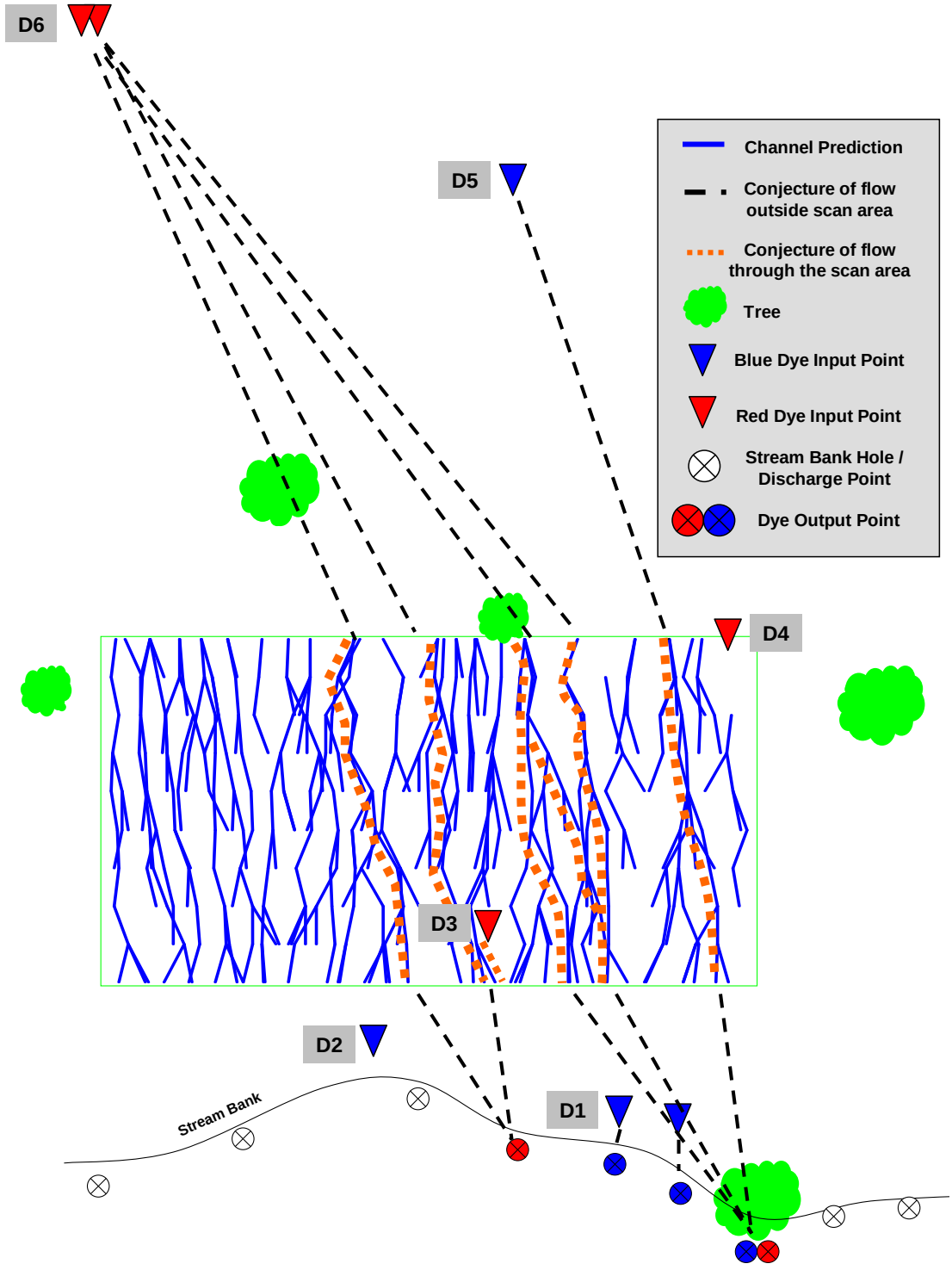

Figure 52. Colored dye injection points (D1-D6) and observed output points compared to the mapping predictions. Potential pathways are highlighted next to the predictions.

5.9 Conclusion

The generalized field procedures for detecting and mapping preferential flow channels were applied and validated in Experiment III at the OPE^3 riparian wetland forest. Channels were detected and mapped into a three dimensional structure and the predictions were corroborated with ground truth from colored tracer dye and auger core samples. Transmission of colored dye verified that preferential conduction existed in the wetland. Furthermore, the connections between observed input and output points could be satisfied by the channels predicted by the mapping algorithm. The sample error rate of thirteen soil core samples (92% accurate) satisfied the requirements of Military Standard 105E for statistical quality control.

Chapter 6: Summary and Conclusions

Ground-penetrating radar was applied to detect and map lateral preferential flow channel structures in the top meter of riparian wetland soils. Procedures were developed and tested in experiments at the UMD Paint Branch Turfgrass Research Facility and validated at the USDA-BARC OPE^3 research site. Scientists employing these tools can now, for the first time, non-invasively map the structure of lateral preferential flow pathways in riparian buffers.

In Experiment I, a field test plot was created to develop generalized methods for detecting channel-like objects. Sixteen PVC pipes simulating channels of different sizes and fill media were buried in four parallel rows. A manual detection methodology was applied to locate the pipes based on reflections in radar scan data collected at different orientations to the plot layout (0% Type I error, 7.8% Type II error). An automated detection algorithm that I created (AGTD) had a higher Type II error rate (29.7%) at a similar Type I error rate (0.7%). Positions and depths were successfully predicted regardless of the scan orientation (mean P_e from the reflection apex with the manual procedure = 11.1 cm**,** standard deviation = 8.0 cm; mean D_e = -0.6 cm, standard deviation = 1.8 cm). The minimum resolvable object size across all angles of intersection (3.00 cm) agreed well with an *in situ* estimate based on wavelength at the upper bound of the GPR antenna's bandwidth (3.1 cm).

In Experiment II, a field test plot was created to test the detection methodologies from Experiment I and to develop an algorithm for connecting the resulting detections into a three-dimensional prediction of the buried objects' geometries. I created a nearest neighbor mapping algorithm (M^3A) to construct the

three-dimensional shape of a connected PVC pipe structure simulating branching preferential flow channels. The pipe segments were effectively detected in 12 parallel GPR scan lines using the manual and automated detection methodologies. There was a performance gap as in Experiment I between the manual procedure and AGTD (8.3% Type II error rate versus 29.2% for AGTD for a 0% Type II error rate versus 0.002% for AGTD). Position and depth prediction accuracy measurements also agreed with those from Experiment I (mean P_e from the reflection apex with the manual procedure = 9.6 cm, standard deviation = 6.9 cm; mean D_e = -0.5 cm, standard deviation = 1.1 cm).

In Experiment III, the methods and algorithms developed in Experiments I and II were applied to detect and map preferential flow channels at an experimental study site in the OPE^3 riparian wetland. Predicted flow channel locations between 15 cm and 65 cm in depth were ground truthed with soil core samples and observations of colored tracer dye transmission. The sample error rate of thirteen soil core samples (92% accurate) satisfied the requirements of Military Standard 105E for statistical quality control. The channel predictions could also account for the observations of preferential tracer dye conduction through the study site.

These three experiments show that preferential flow channels in riparian wetlands can be reliably detected and non-invasively mapped using GPR. This is a distinct contribution compared to previous studies, notably Holden et al. (2002). The primary difference is that I mapped preferential pathway geometries in three dimensions automatically, without cueing from manual site surveys. Incorporating features of algorithms from the field of computed tomography (Perret et al., 1999;

Pierret et al., 2002a), the mapping algorithm (M^3A) is a useful new tool for reconstructing channel-like target geometries, from preferential flow channels to tree root structures.

The resulting methods can be applied by researchers, including scientists without engineering backgrounds, to non-invasively uncover the pathways of by-pass flow through riparian wetlands and relate those mechanisms to measurements of environmental quality.

The prevalence of flow channels can be measured within a watershed and compared to field observations across watersheds in different geographical regions (Weiler and Naef, 2003). Channel density per unit surface area can be calculated using the convolution procedure described in Chapter 5 and the fraction of the matrix with macropores can be determined by assuming an average channel diameter. These calculations can be input to lumped models predicting water flow rates through riparian buffers (Lin et al., 1999). Furthermore, M^3A pathway predictions can be used to bootstrap and reduce the uncertainty of stochastic hydrologic flow path models.

Channel location predictions can also direct the placement of water quality samplers in environmental quality studies. Samplers can be installed into detected channels to collect real-time flow measurements and water quality samples to directly assess by-pass nutrient transport.

In addition to directly applying these GPR methods, future researchers can refer to this study as an example of how to manipulate analysis techniques described in literature for new non-invasive detection applications in new settings. The foundation of the manual detection methodology has been enumerated in many

studies into non-invasive detection of channel-like targets such as utility pipes (Allred et al., 2004; Park et al., 2003; Zarkhidze and Lemenager, 2004). For each new application, the researcher must build upon that foundation using the specific requirements of the application. The properties of the soil and the targets (size, depth, lateral extent, and electromagnetic contrast from the medium) must be understood to design a successful scanning and analysis procedure (number of scan lines, scan line spacing, antenna center frequency, and signal processing filter types).

Future research into automated target detection can also reference the lessons learned from this study. The automated detection methodology (AGTD) I created using techniques from the field of image processing showed promise but could not fully replicate the results of the manual methodology. Further development is required to improve the detection rate of this algorithm before the human operator can be taken completely out of the analysis loop. Areas of potential exploration include adaptive amplitude thresholding techniques based on gray-level histograms (Otsu, 1979; Yang and Gupta, 1993), more robust segmentation techniques (Malik et al., 2001; Pal and Pal, 1993; Svensson, 2008), and an iterative methodology (Dell'Acqua et al., 2004; Goldman and Cohen, 2004).

Similar algorithms in the literature (Al-Nuaimy et al., 2002; Capineri et al., 1998; Herman and Singh, 1995; Shihab et al., 2003; Youn and Chen, 2002) have reported successes automatically detecting targets but it is difficult to determine the relative performance of the various approaches. Standard datasets should be established and made available to all researchers and common metrics established to provide a common ground for comparison.

One extension of this work is to create an automated system using the GPR detection and mapping algorithms for canvassing large study areas. A locomotive robot equipped with a computer, GPR sensor, and global positioning system (GPS) could be programmed to perform labor-intensive GPR surveys and map target features across study areas autonomously (Fig. 53).

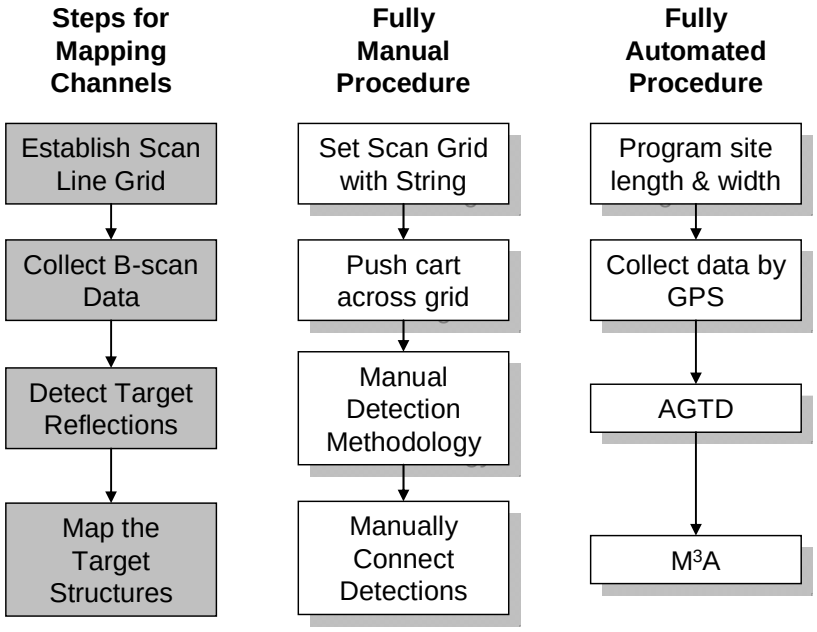

Figure 53. Manual and fully automated versions of the general GPR application procedure. AGTD = Automated GPR Target Detection algorithm. M^3A = Macropore Morphology Mapping Algorithm.

The researcher would program the desired coordinates of survey sites and the length and scan spacing of the GPR survey, the robot would collect data at the sites based on GPS measurements, the AGTD algorithm (described in Chapter 3) would be applied to the scan data to generate target detections, and M^3A (described in Chapter 4) would be applied to predict the three-dimensional structures. The results could be

stored on the robot's computer and transmitted back to the laboratory for real-time examination.

Other potential applications include investigations addressing the impacts of preferential pathways on nutrient feedbacks to biological and hydrological systems such as: the inter-dependencies of wetland earthworms (Shipitalo et al., 2004) or the crayfish that are abundant in the OPE^3 wetland, their burrows, and preferential flow; and the relationships between plant nutrient availability, water availability, and tree root structures (Gish et al., 1998; Holden, 2005; Noguchi et al., 1999; Stewart et al., 1999).

Appendix A: Experiment I Data

Refer to Table 9 for a description of each of the 16 pipes buried in the Eperiment I field test plot.

Table 9. The 16 Experiment I pipes with nominal pipe size (NPS), inner diameter (ID), and fill type (W=water, A=air, A/W=50% air 50% water, SW=salt water).

Pipe Label	NPS	ID (cm)	Fill Type	Depth (cm)	Salt Mass (g)	Salt Concentration (g/cm3)
1w	0.5	1.85	W	20.3	0	0
1aw	0.5	1.85	A/W	15.2	0	0
1a	0.5	1.85	A	17.8	0	0
1sw	0.5	1.85	SW	15.2	20.1	0.020
2w	1	3.00	W	17.8	0	0
2aw	1	3.00	A/W	17.8	0	0
2a	1	3.00	A	17.8	0	0
2sw	1	3.00	SW	17.8	63.2	0.024
3w	1.5	4.46	W	17.8	0	0
3aw	1.5	4.46	A/W	15.2	0	0
3a	1.5	4.46	A	15.2	0	0
3sw	1.5	4.46	SW	17.8	129.9	0.023
4w	2	5.64	FW	17.8	0	0
4aw	2	5.64	A/FW	15.2	0	0
4a	2	5.64	A	17.8	0	0
4sw	2	5.64	SW	17.8	216.5	0.024

The AGTD algorithm was applied to each Experiment I scan line using the parameters listed in Table 10.

Table 10. Automated target detection algorithm (AGTD) parameter specification.

Parameter	Value
pre-filter	81 point wide moving window average
analysis depth gate	between the ground surface and the maximum recorded depth
hysteresis upper amplitude threshold	6
hysteresis lower amplitude threshold	4.8
minimum bandwidth requirement	11.43 cm
target window size ([in depth, position])	[10.16 cm, 5.08 cm]

The detection performance for each scan line is compiled in Table 11. The number of correct detections for the automated algorithm (d_A) and manual procedure (d_M) are listed, as well as the number of false alarms by the algorithm (fa_A), and the number of total detection cells (*ngc*) and correctly predicted empty detected cells (np_A). The results are broken into two depth ranges: all depths below the ground surface and a subset of depths 5 cm under the ground surface and below. The latter was included to filter out false alarms close to the ground surface that were induced by air pockets left in the pipe burial process.

Table 11. Detection performance by scan line for all angles of intersection (90˚ = perpendicular, 0˚ = parallel, 45˚ = angled, R-to-L = right-to-left, L-to-R = left-to-right). p = number of possible detections per scan and total; d = number of detections per scan and total (d_M = manual, d_A = auto-detected); ngc = number of grid cells with no truth present; fa_A = number of algorithm false alerts per scan and total; np_A = number of grid cells with no detections or truth per scan and total.

Scan Line	Angle	p	d_M	d_A	ngc[†]	fa_A[‡]	np_A[ξ]
SL-24	90˚	4	4	1	101 (80)	1 (0)	100 (80)
SL-25		4	4	4	101 (80)	0 (0)	101 (80)
SL-26		4	4	3	111 (88)	1 (0)	110 (88)
SL-27		4	4	4	101 (80)	1 (0)	100 (80)
SL-40	0˚	4	4	3	116 (92)	7 (2)	109 (90)
SL-41		4	4	4	111 (88)	2 (1)	109 (87)
SL-42		4	4	4	121 (96)	7 (2)	114 (94)
SL-43		4	4	3	121 (96)	4 (2)	118 (94)
SL-44	45˚ R-to-L	1	0	0	39 (31)	0 (0)	39 (31)
SL-45		2	2	2	83 (66)	4 (0)	79 (66)
SL-46		3	2	2	107 (85)	1 (1)	106 (84)
SL-47		4	3	1	151 (120)	2 (0)	149 (120)
SL-48		3	3	3	122 (97)	2 (0)	121 (97)
SL-49		2	2	2	83 (66)	0 (0)	83 (66)
SL-50		1	1	0	49 (39)	0 (0)	49 (39)
SL-51	45˚ L-to-R	1	0	0	34 (27)	1 (0)	33 (27)
SL-52		2	2	2	83 (66)	1 (0)	82 (66)
SL-53		3	3	1	117 (93)	3 (0)	114 (93)
SL-54		4	3	2	146 (116)	2 (0)	144 (116)
SL-55		3	3	1	112 (89)	1 (0)	109 (87)
SL-56		2	2	2	88 (70)	1 (0)	86 (69)
SL-57		1	1	1	49 (39)	1 (0)	48 (39)
All		64	59	45	2146 (1704)	42 (8)	2103 (1693)

[†] in parentheses, number of grid cells with no truth in a depth subset below 5 cm
[‡] in parentheses, number of false alarms in depth subset below 5 cm
[ξ] in parentheses, number of grid cells with no detections in depth subset below 5 cm

B-scan images with 91.4 cm long samples around each of the Experiment I PVC pipes at perpendicular and angled intersections with GPR scan lines show the different characteristics of reflection hyperbolas with target size and orientation (Fig. 54-59). B-scan images for scans intersecting the pipe layout with parallel angles of intersection show the characteristic constant bands of energy reflectance (Fig. 60-61). A constant gain factor of 5 was applied to the data as well as a background removal filter (Eq. [3-2]). The y-axis was offset by 7.62 cm to align zero depth with the true ground surface.

Samples were grouped together by nominal pipe size (NPS) level and angle of intersection for each of the four fill types: perpendicular (Fig. 54, 55), 45 degree angle from right-to-left (Fig. 56, 57), 45 degree angle from left-to-right (Fig. 58, 59), and parallel (Fig. 60, 61). The true position of the pipes, response apexes of the corresponding GPR responses (if any), and traces of the first and second half-cycles are shown with each sample. The truth markers scale in size with the pipe diameter. If a response could not be identified due to lack of amplitude, the following annotation was made: “No Significant Response.”

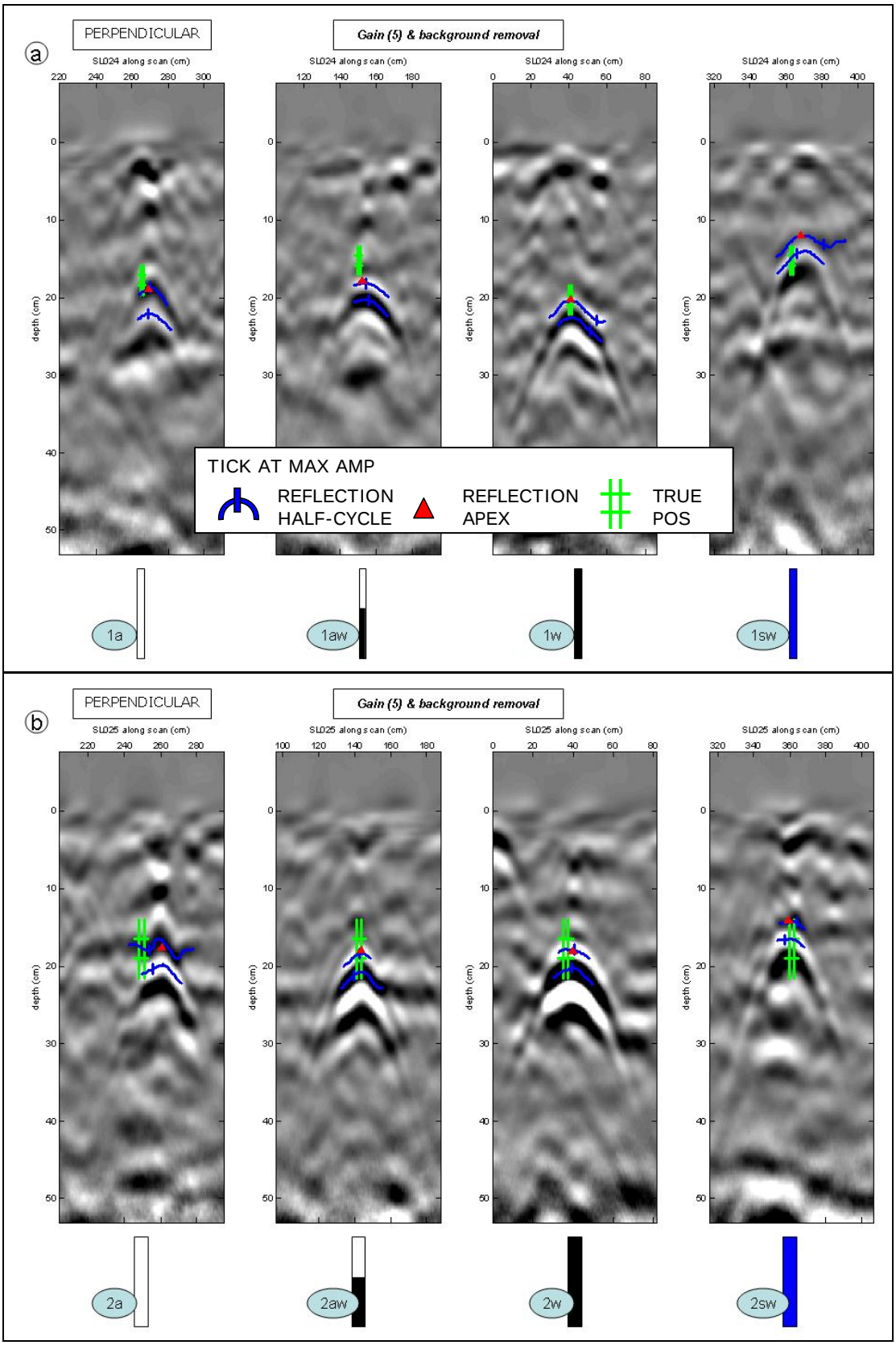

Figure 54. Perpendicular B-scans of the (a) 0.5 NPS and (b) 1.0 NPS PVC.

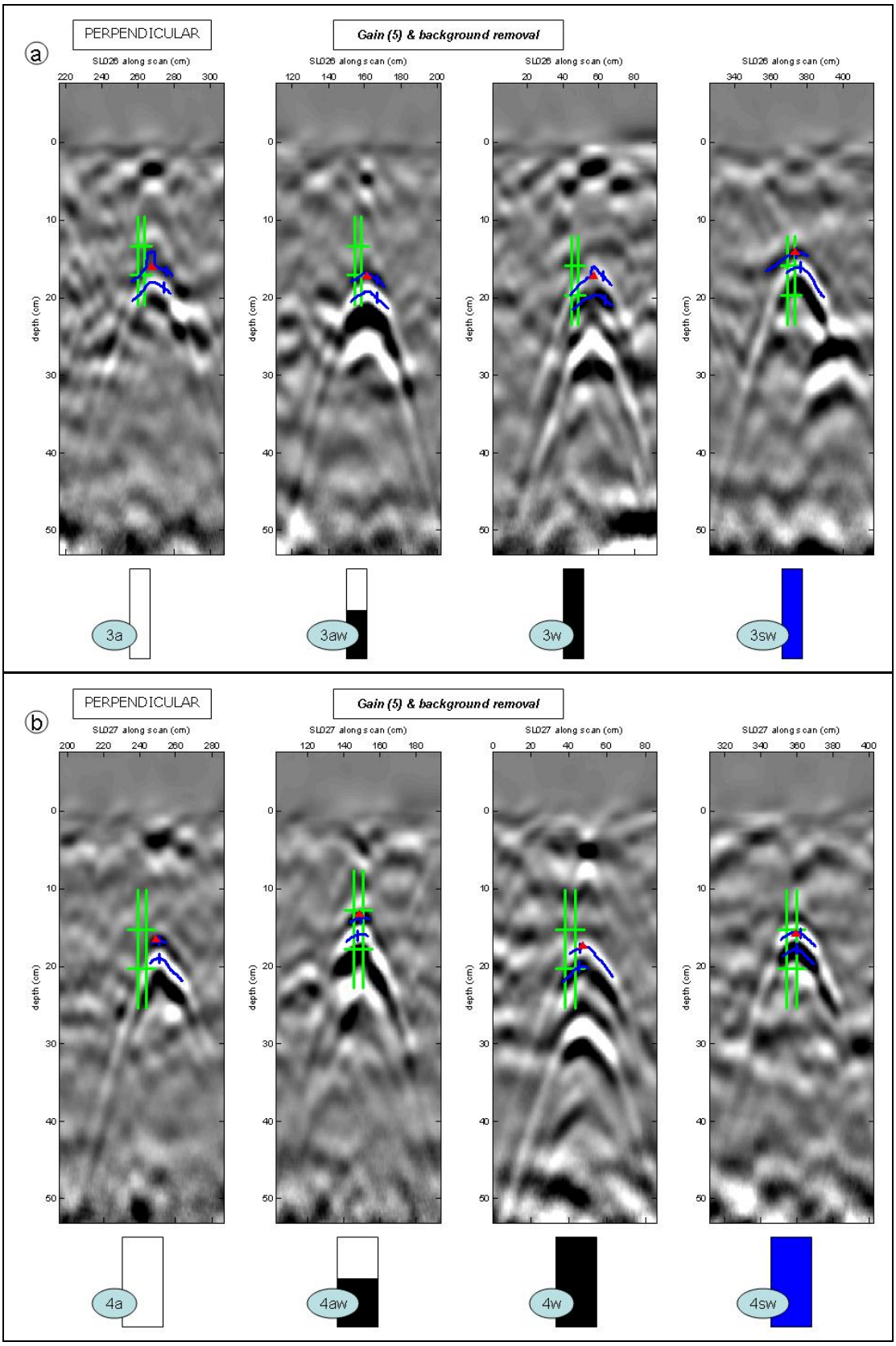

Figure 55. Perpendicular B-scans of the (a) 1.5 NPS and (b) 2.0 NPS PVC.

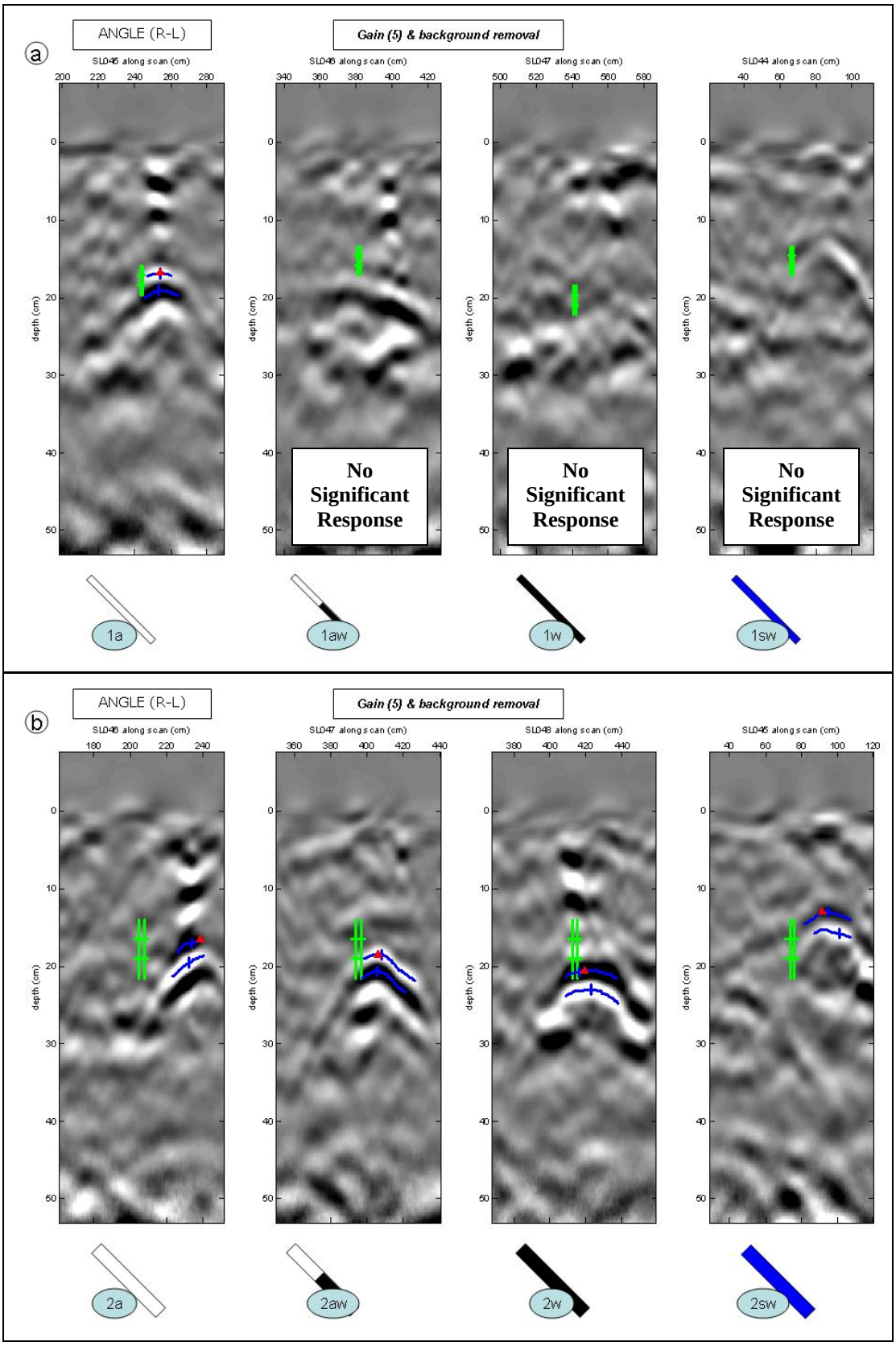

Figure 56. Angled (R-L) B-scans of the (a) 0.5 NPS and (b) 1.0 NPS PVC.

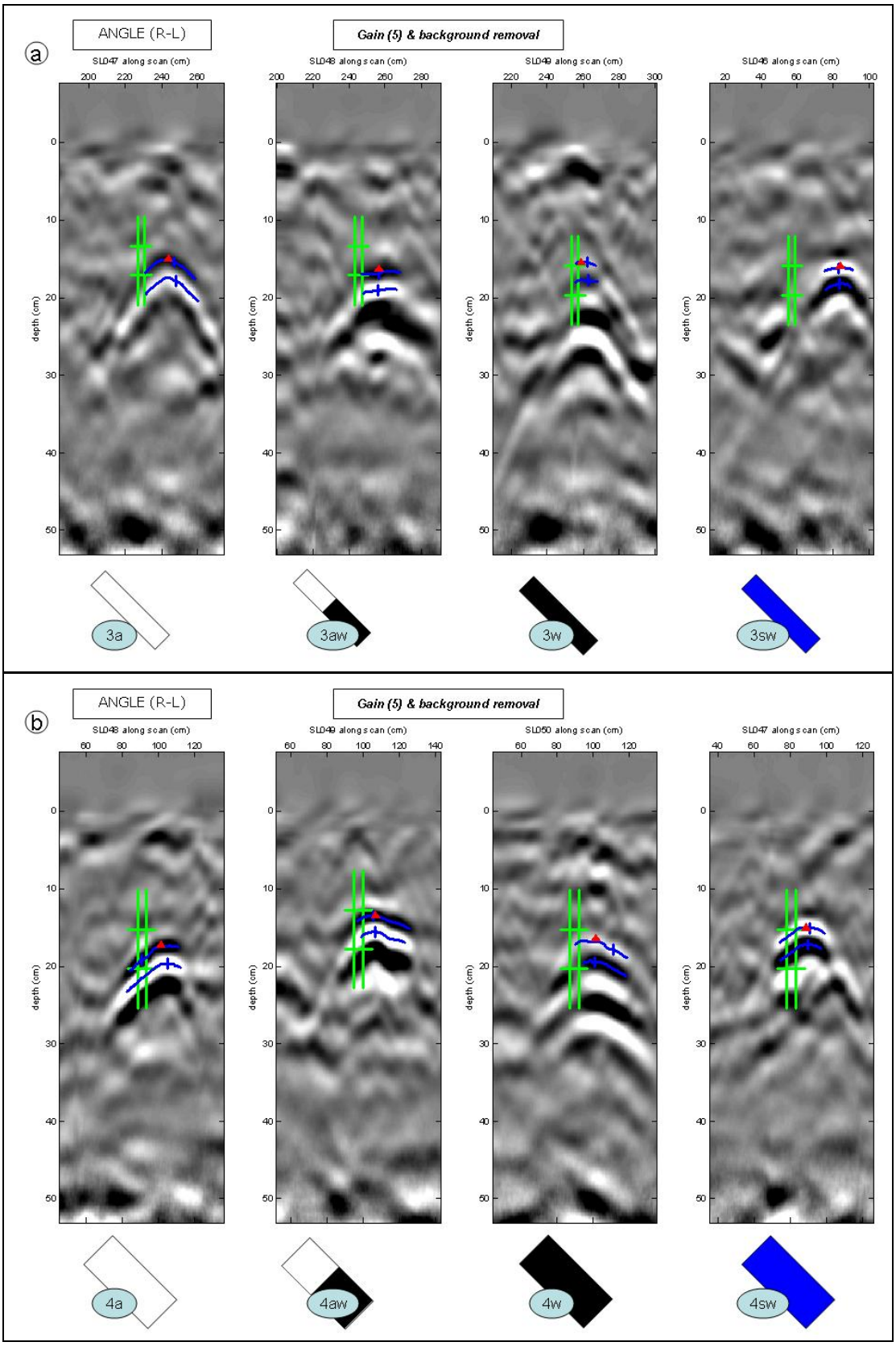

Figure 57. Angled (R-L) B-scans of the (a) 1.5 NPS and (b) 2.0 NPS PVC.

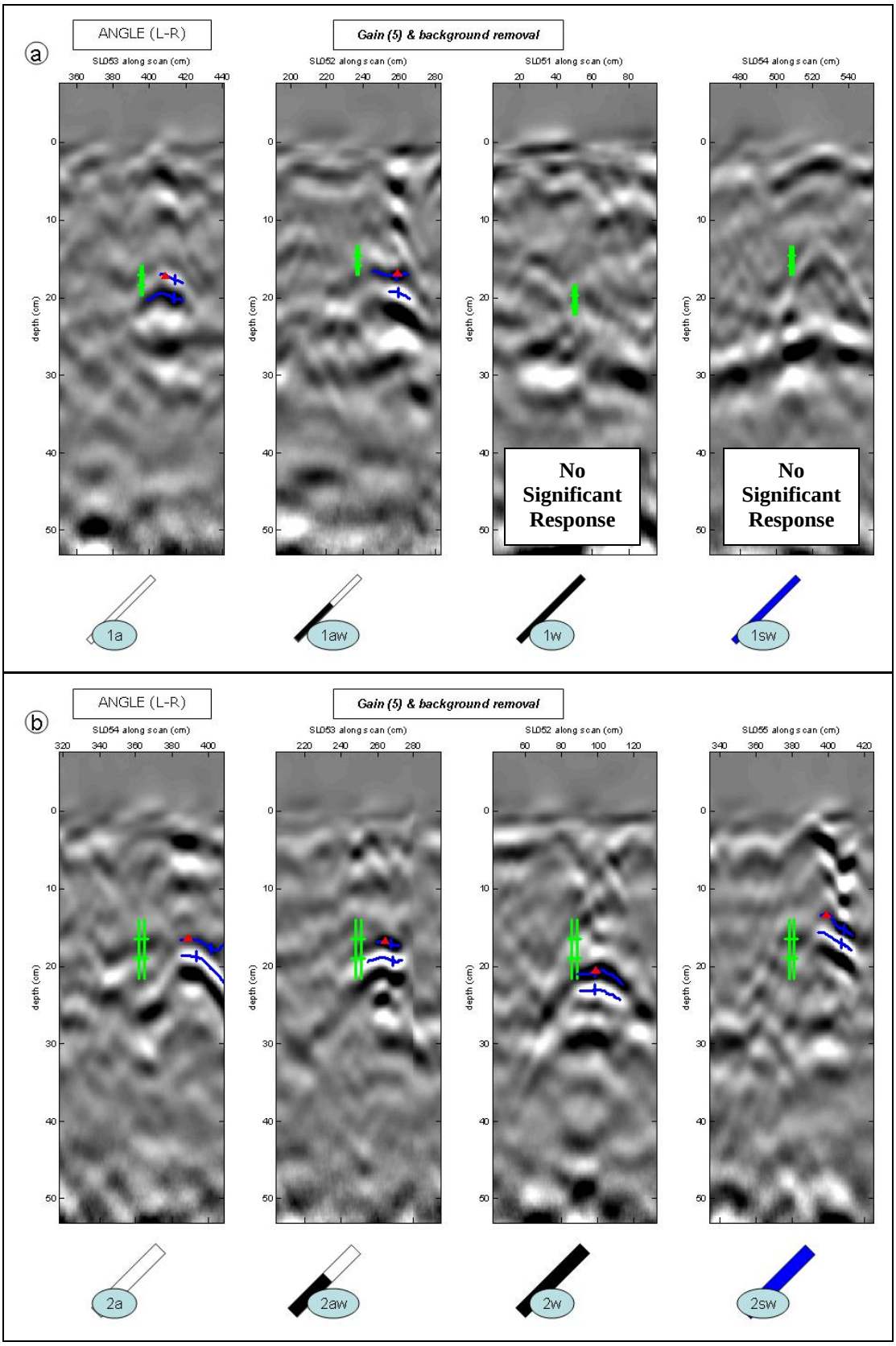

Figure 58. Angled (L-R) B-scans of the (a) 0.5 NPS and (b) 1.0 NPS PVC.

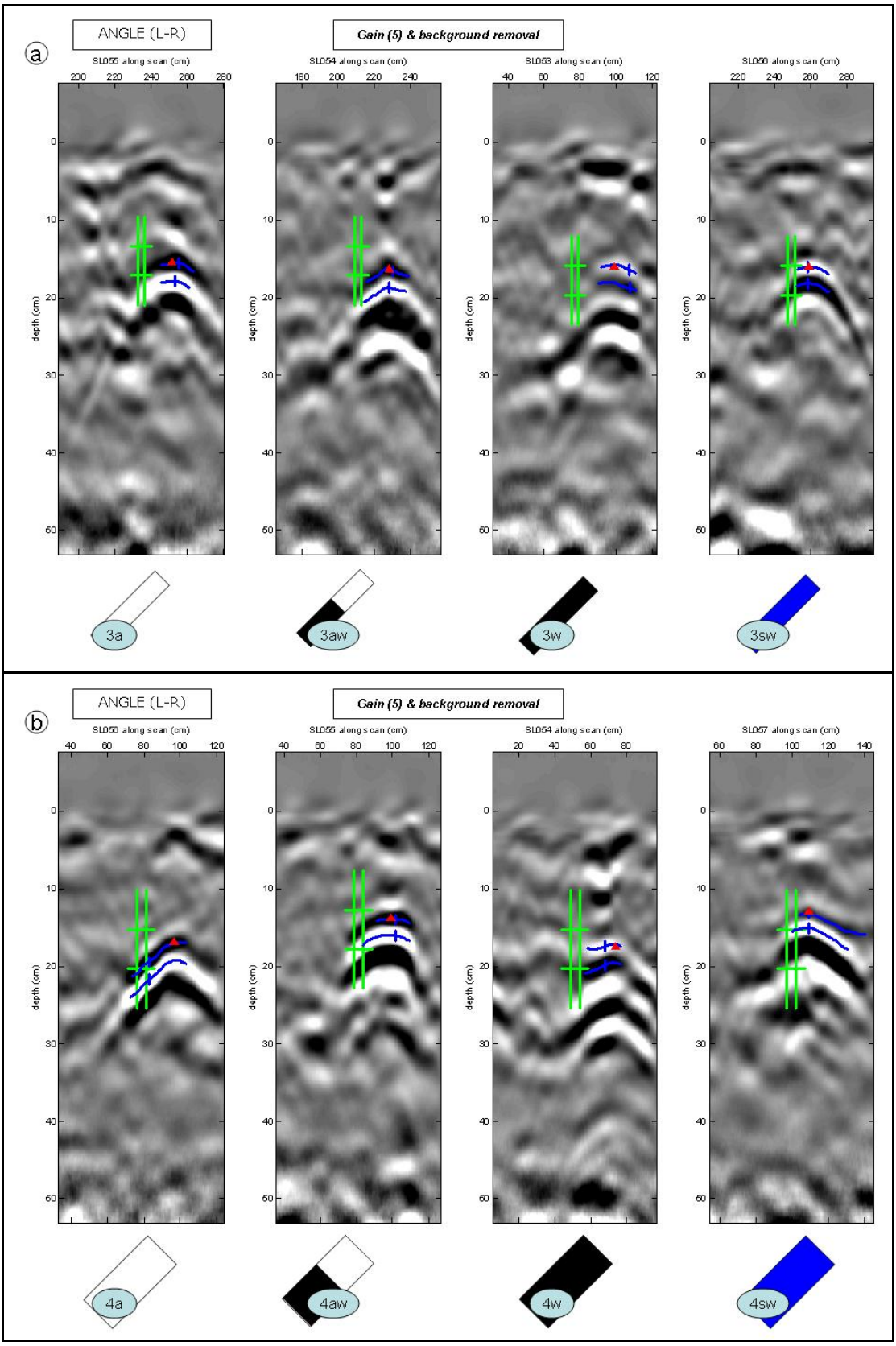

Figure 59. Angled (L-R) B-scans of the (a) 1.5 NPS and (b) 2.0 NPS PVC.

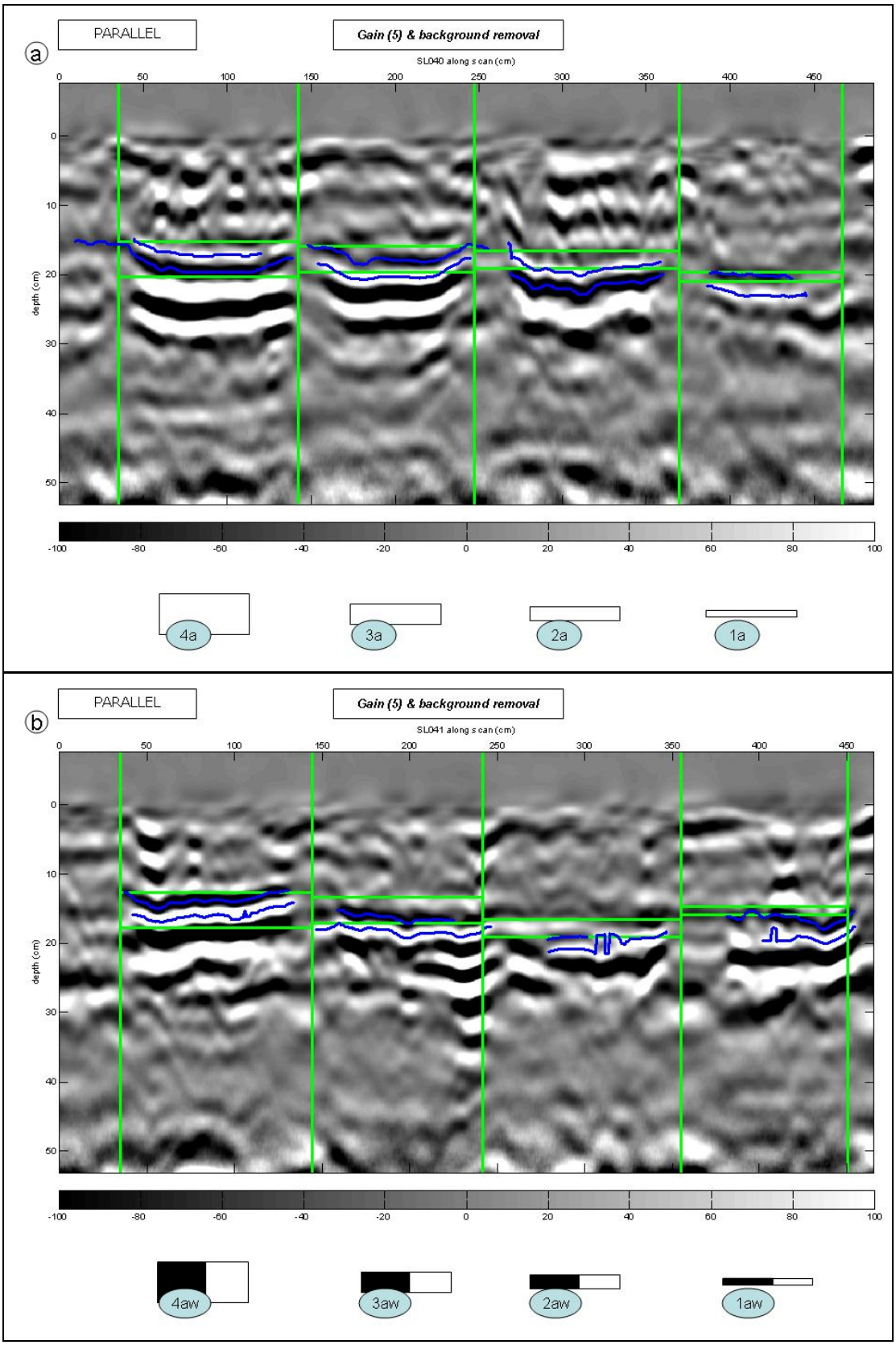

Figure 60. Parallel B-scans of the (a) air and (b) 50% air 50% water filled PVC.

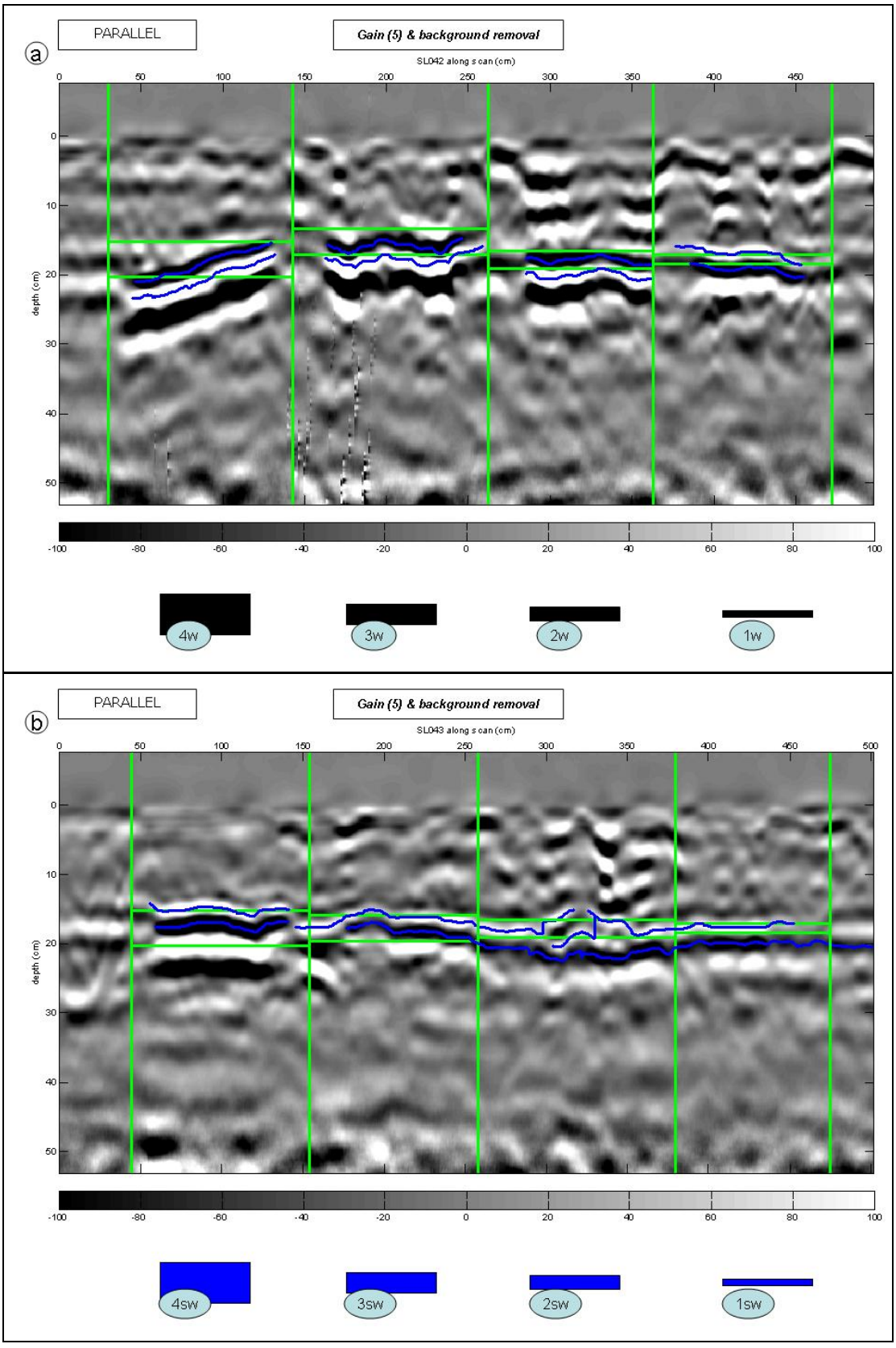

Figure 61. Parallel B-scans of the (a) water and (b) salt water filled PVC.

Appendix B: Experiment I Feature Extraction Analysis

B.1 Introduction

The Experiment I data was examined to discern whether nominal pipe size (NPS) and B-scan line orientation could be determined from the form of the GPR responses. If predictive features can be identified, future studies can extract the feature data from the GPR B-scans to characterize the unknown properties of detected targets (Al-Nuaimy et al., 2004).

Three features of the reflection hyperbolas from the 16 combinations of NPS and fill types were compared across the three non-parallel scan line orientations (perpendicular, 45 degree angle from right-to-left, and 45 degree angle from left-to-right): maximum reflected amplitude, 3 dB hyperbola width, and hyperbola skew. The features were measured and analyzed for trends.

B.2 Literature Review

Similar research has focused on extracting mostly amplitude-related features of GPR reflections to predict the size of tree roots and PVC pipes. Barton and Montagu (2004) showed that tree root target diameters could be predicted (R^2 = 0.89) based on the intervals between successive zero crossings in depth. Butnor et al. (2001) reported that tree root target diameters could be predicted with reasonable accuracy based on a measurement called "high amplitude area" (area under the half-cycle above a threshold). Cox et al. (2005) found correlations of amplitude with both tree root and PVC pipe target diameters. Dannoura et al. (2008) examined several features (peak reflection amplitude, "high amplitude area," and "pixels within

threshold area") and found significant correlations ($p < 0.001$) with *Cryptomeria japonica* root diameter.

B.3 Feature Extraction and Trend Analysis

The maximum absolute amplitudes of the target reflections were accumulated for the first half-cycle response traces (Fig. 62). The background amplitude distribution across all waveforms was also calculated for comparison (Fig. 62 g).

The amplitude measurements were fit with respect to inner pipe diameter using linear regression models for each of the fill types and scan orientations, and across all fill measurements combined, and goodness of fit was calculated. The results were accumulated for the first half-cycle trace (Table 12) and the second half-cycle trace (Table 13) separately to note any differences.

There was reasonable correlation of amplitude measurements from the perpendicular scan lines with inner diameter; the fresh water 1.0 NPS amplitude was an outlier from this trend. Correlation coefficients were smaller for the angled scan lines. The maximum amplitudes were greater than 5 while the background levels were almost entirely less than 5.

Reflection width (w_{3dB}) was defined as the difference between the right (P_{re}) and left edges (P_{le}) of the half-cycle trace boundaries to half of the peak trace amplitudes:

$$w_{3dB} = P_{re} - P_{le} \qquad \text{[B-1]}$$

The widths of the first half-cycle traces were calculated and plotted (Fig. 63). No clear trend was observed with NPS. Part of the variability was due to measurement error with the traces of the half-cycle amplitude (refer to Fig. 54: the

trace of pipe 2a erroneously tracks away from the main lobe of the response hyperbola).

A unitless measure for skew (s) was defined with a range of [0, 1] as the relative distance between the peak (P_p) and the left and right edges (Eq. [B-2]). Values closer to zero indicate less skew while values closer to one indicate more skew.

$$s = \left| \frac{P_p - P_{le}}{P_{re} - P_{le}} - 0.5 \right| * 2 \qquad \text{[B-2]}$$

Skew values were calculated from the peaks of the apex of the response hyperbolas (Fig. 64 a, b, c and Fig. 65 g, h, i) and the locations of the maximum amplitudes (Fig. 64 d, e, f and Fig. 65 j, k, l) in the first reflection half-cycle for the perpendicular and angled scan lines. Differences between reflections in perpendicular scan lines and angled scan lines were most apparent in the calculations from the apex peak position (Fig. 65 g, h, i); measurements from perpendicular scan lines clustered near zero whereas those from angled intersections clustered closer to 0.5, particularly the left-to-right oriented scans.

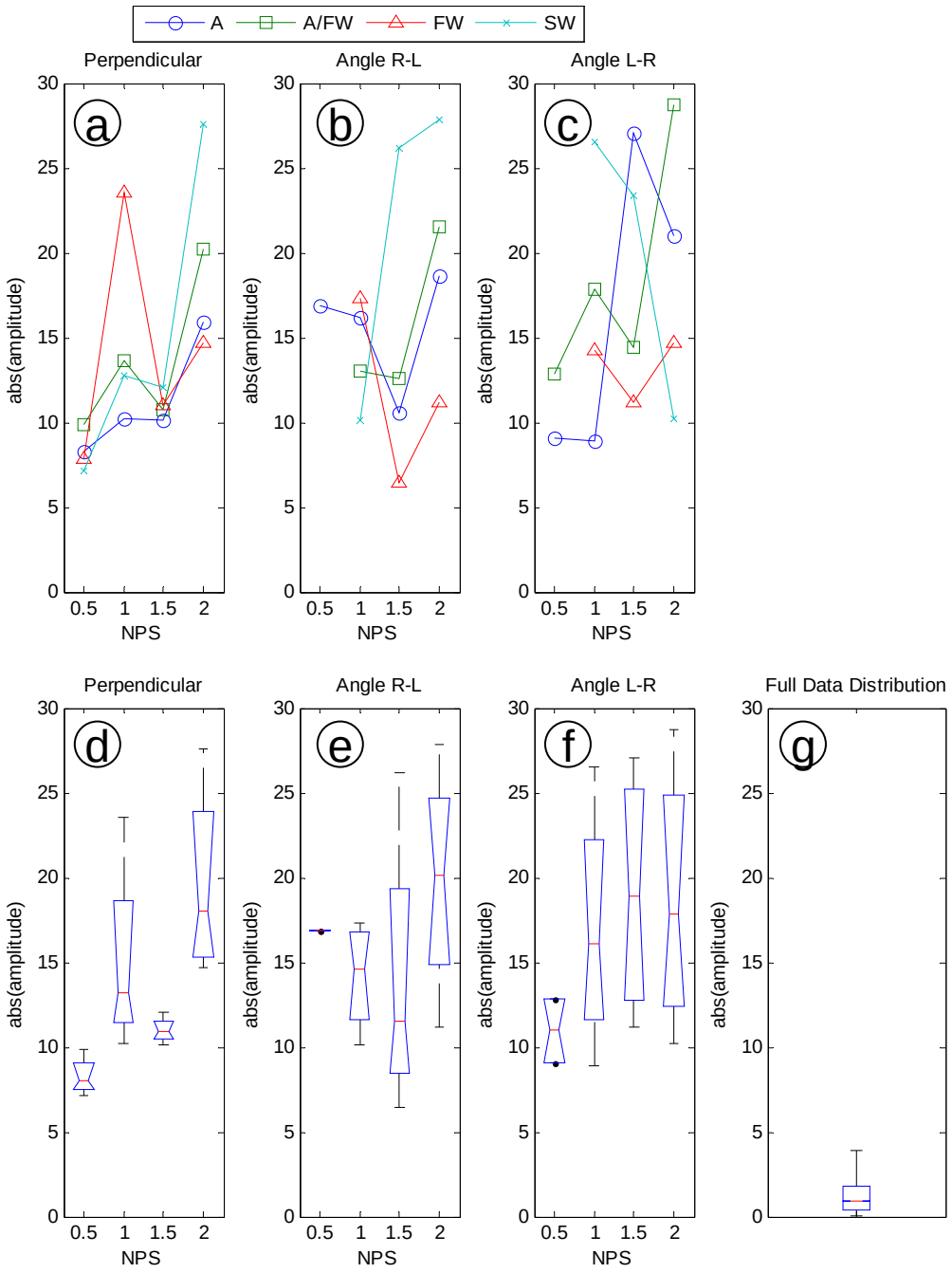

Figure 62. (a, b, c) Scatter plots of maximum amplitude for responses from each fill type and nominal pipe size (NPS) and (d, e, f) box plots combining measurements across all fill types. (g) Box plot of all scan sample amplitudes (without outliers). The measurements are sorted by the angle of intersection: (a, d) perpendicular, (b, e) R-to-L 45 degree angles, and (c, f) L-to-R 45 degree angles.

Table 12. Linear regression statistics (m = slope, R^2 = coefficient of determination) for maximum absolute first half-cycle amplitude predicted by inner pipe diameter.

Pipe/Scan Property		Fit Statistic	
Orientation	Fill Type	m	R^2
Perpendicular	Air	1.75	0.77
Perpendicular	Air/Water	2.14	0.57
Perpendicular	Water	0.45	0.01
Perpendicular	Salt Water	4.65	0.76
Perpendicular	All Fills	2.25	0.33
Angle (R-to-L)	Air	-0.08	0.00
Angle (R-to-L)	Air/Water	3.08	0.65
Angle (R-to-L)	Water	-2.54	0.38
Angle (R-to-L)	Salt Water	6.87	0.87
Angle (R-to-L)	All Fills	1.34	0.07
Angle (L-to-R)	Air	4.34	0.63
Angle (L-to-R)	Air/Water	3.35	0.60
Angle (L-to-R)	Water	0.06	0.00
Angle (L-to-R)	Salt Water	-6.04	0.85
Angle (L-to-R)	All Fills	1.64	0.11

Table 13. Linear regression statistics (m = slope, R^2 = coefficient of determination) for maximum absolute second half-cycle amplitude predicted by inner pipe diameter.

Pipe/Scan Property		Fit Statistic	
Orientation	Fill Type	M	R^2
Perpendicular	Air	2.66	0.69
Perpendicular	Air/Water	4.92	0.83
Perpendicular	Water	-1.28	0.03
Perpendicular	Salt Water	3.96	0.72
Perpendicular	All Fills	2.56	0.19
Angle (R-to-L)	Air	0.74	0.05
Angle (R-to-L)	Air/Water	4.65	0.54
Angle (R-to-L)	Water	-1.32	0.52
Angle (R-to-L)	Salt Water	1.78	0.37
Angle (R-to-L)	All Fills	1.46	0.08
Angle (L-to-R)	Air	5.41	0.62
Angle (L-to-R)	Air/Water	6.43	0.65
Angle (L-to-R)	Water	0.71	0.18
Angle (L-to-R)	Salt Water	3.58	0.55
Angle (L-to-R)	All Fills	4.03	0.34

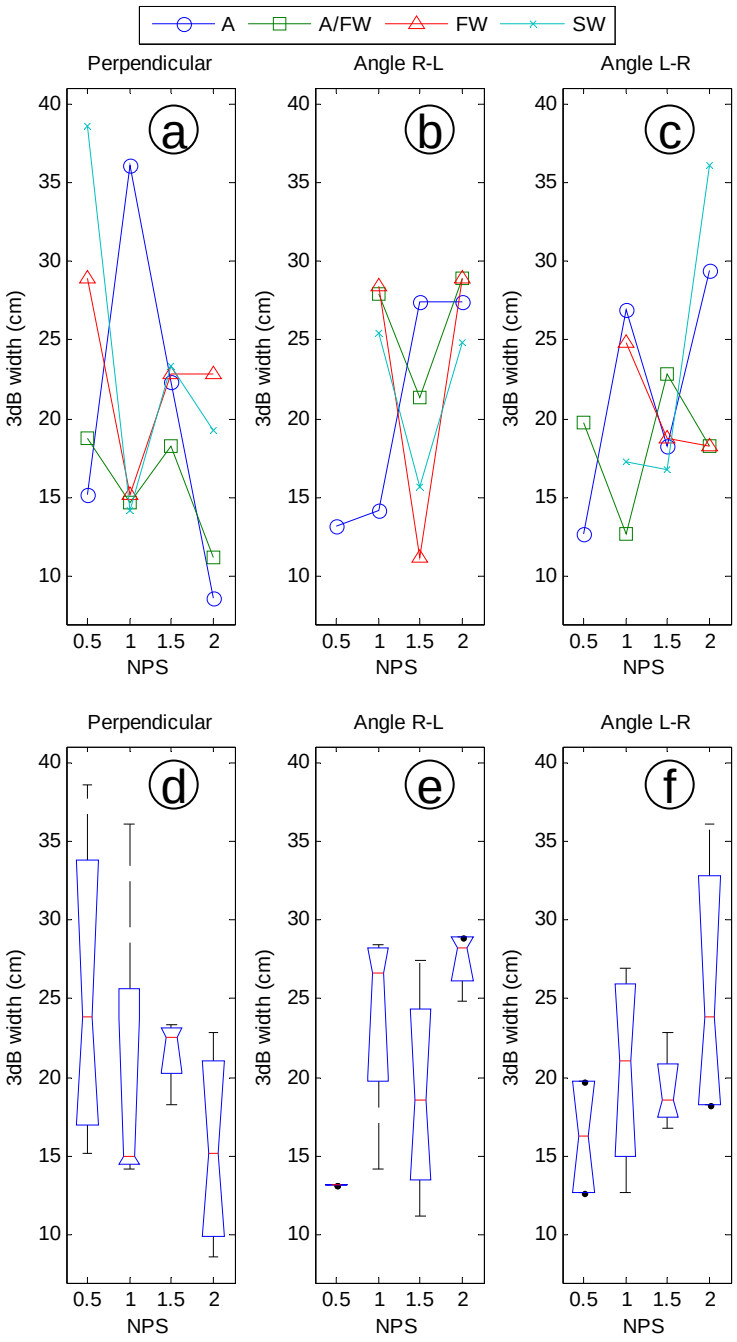

Figure 63. (a, b, c) Scatter plots of 3 dB widths for each fill type and nominal pipe size (NPS) and (d, e, f) box plots combining all fill types. The measurements are further sorted by the angle of intersection: (a, d) perpendicular, (b, e) R-to-L 45 degree angles, and (c, f) L-to-R 45 degree angles.

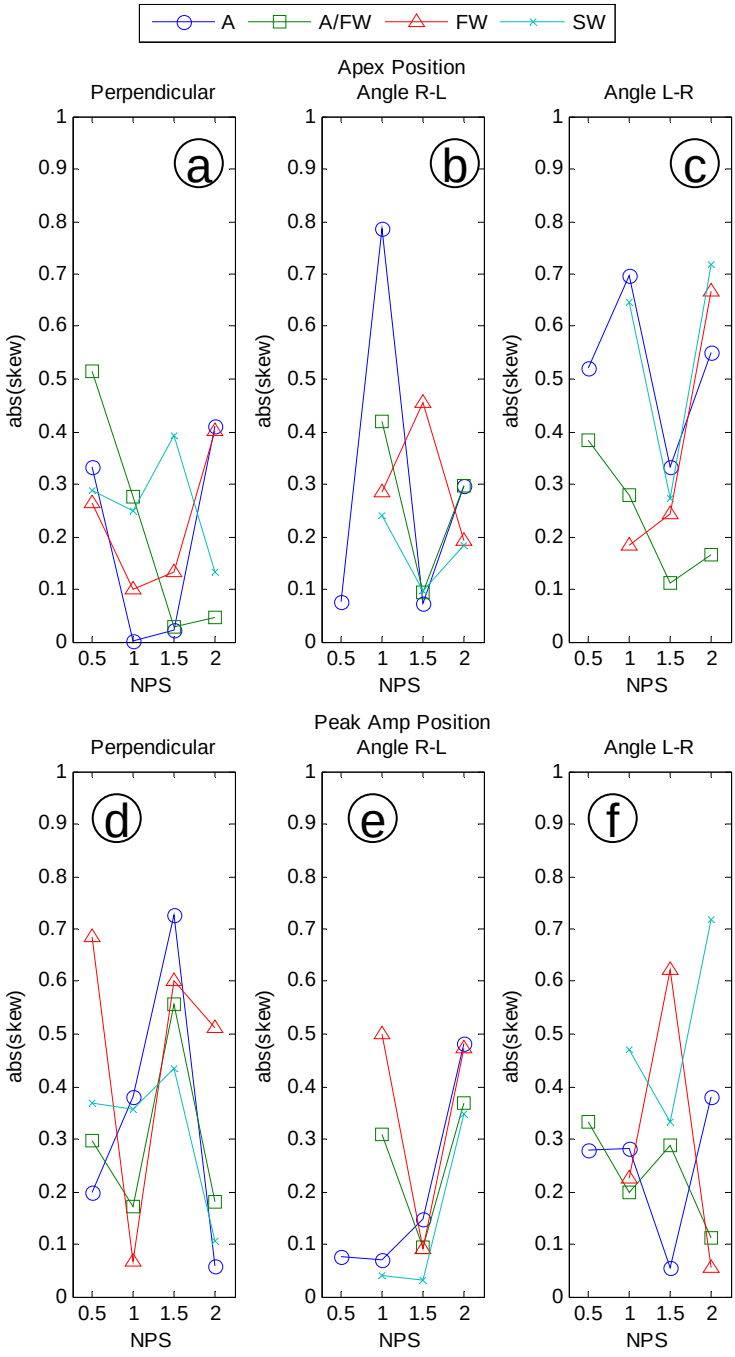

Figure 64. Scatter plots of skew measurements for each fill type and nominal pipe size (NPS) from the (a, b, c) apex of the response and (d, e, f) maximum amplitude location. The measurements are further sorted by the angle of intersection: (a, d) perpendicular, (b, e) R-to-L 45 degree angles, and (c, f) L-to-R 45 degree angles.

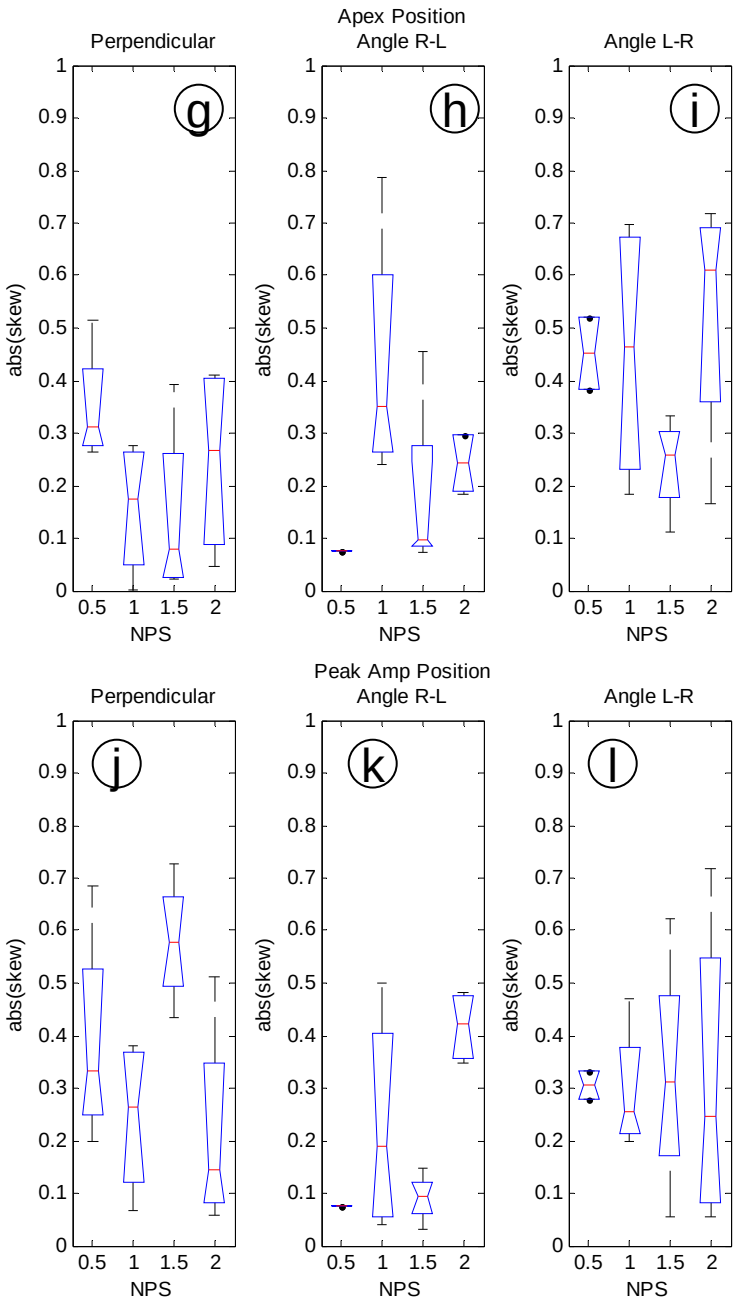

Figure 65. Box plots of skew measurements across all fill types for each nominal pipe size (NPS) from the (g, h, i) response apex and (j, k, l) maximum amplitude location. The measurements are further sorted by the angle of intersection: (g, j) perpendicular, (h, k) R-to-L 45 degree angles, and (i, l) L-to-R 45 degree angles.

B.4 Conclusion

Comparisons of descriptive statistics extracted from PVC pipe reflections in the GPR scan data indicated that there were some differences in these measurements between different pipe sizes and fill media. However, it is unclear how useful these statistics could be as a predictor for target size and target orientation with respect to the scan. Additional study of this problem is needed with a greater range of pipe size.

Trends were observed in some measurements of maximum amplitude with respect to NPS (e.g., the salt water fill with angled R-to-L scan lines had an R^2 of 0.87) as reported in the literature. However, the variability between replicates (intersection angles and fill media) casts doubt on the applicability of amplitude to predict target size, at least for the sizes considered in this study. A stronger correlation could perhaps be uncovered with a wider range of target sizes.

No one fill type had consistently higher amplitudes than any other. One explanation for this finding is the attenuation (α) and conductivity (σ) properties (Table 14) of salt compared to fresh water and their effects on electromagnetic (EM) energy. EM energy attenuates quicker in more electrically conductive materials because the electrical component of the propagating wave is rapidly conducted away (Conyers, 2004). Therefore, even though salt solution has a slightly higher dielectric, energy is attenuated by the solution instead of fully reflected. Another potential explanation, and complication, is that the salt may have settled out of solution to the bottom of the pipes by the time the scan data were collected.

Table 14. Properties of air and water relating to GPR reflectance, including dielectric (k), electrical conductivity (σ), velocity (v), and attenuation (α) (Annan, 2001).

Material	k	σ (mS/M)	v (m/ns)	α (dB/m)
Air	1	0	0.30	0
Distilled water	80	0.01	0.033	0.002
Fresh water	80	0.5	0.033	0.1
Sea water	80	3000	0.01	1000

Effects of angle of intersection were observed, particularly with the skew measurements out of the left-to-right angled scan lines compared to the perpendicular scans for positions marked at the reflection apex. Some evidence was also seen of the response width correlating with increasing NPS, particularly with the left-to-right angled scans, but its validity is questionable given that the inverse was measured in the perpendicular scans.

Appendix C: M^3A

C.1 Algorithm Details

M^3A operates according to a nearest neighbor principle that links together targets detected at similar positions on successive scan lines. Detections are matched and connected into a branch-node data structure called *MP* using a coding device called an "extrapolation box." The box defines the limits in space to capture candidate "neighbors," detections that are close in proximity to a detection on the previously considered scan line.

Similar nearest neighbor rules were specified by Perret et al. (1999) to generate branch-node graphs of vertical macropores (with a radius of <1 mm) imaged in soil cores using a computer-assisted tomography (CAT-scan) reconstruction algorithm.

C.1.1 Extrapolation Box

The mapping algorithm links detections on adjacent scan lines based on a distance qualification. Extrapolation search boxes are created for each "active" predicted structure segment (*MP*) on the current scan based on the position of the node of that *MP* on the previous scan. *MP* branches become "inactive" if no matches are made to them in a scan; these branches are not considered for matches in any subsequent scans.

The size of the box (in position along the scan and depth) is specified by two parameters (*positionTravel* and *depthTravel*) and the distance between the current and

previous scans (SL-1 to SL). The first parameter, *positionTravel*, is the size of the extrapolation box in the position dimension on scan line SL when there is one unit of distance between SL and SL-1. The second parameter, *depthTravel*, is the size of the extrapolation box in the depth dimension on scan line SL for one unit of distance from scan line SL-1.

C.1.2 Matching Detections to *MP*s

Links are formed by comparing the locations of detections on the current scan to the extrapolation box extents of active *MP*s. All detections that fall inside the search volumes are identified (i.e., when the detection position is greater than the lower limit of the box's position dimension and less than the upper limit of the box's position dimension, and similarly for depth) and goodness of fit measures are calculated.

Goodness is currently defined as the combined (unweighted) distance in position and depth from the expected position of the *MP* branch on the current scan line based on the previous scan line (i.e., the absolute difference from the detection location to the center of the extrapolation box).

This portion of the algorithm can be expanded in the future to take into account more complicated association cues that are not currently available. Target diameter and relative orientation can be included to enhance the fidelity of the goodness measure.

C.1.3 Adjudicating Multiple Matches

There are three possible outcomes of the matching operation: detections may not fall within the extent of any *MP* extrapolation boxes, they may fall within a single *MP* extrapolation, or they may fall within multiple *MP* extrapolations. A given detection may only be linked to a single *MP* so a procedure is employed to break the ties in the latter case based on goodness of fit. The detection is associated to the *MP* with the "best" fit, which is considered the minimum distance measure.

C.1.4 Closing *MP* Gaps

After the matching operation is completed, suggestions are made to fill gaps in the *MP* links (e.g., in case of Type II errors). Extrapolation boxes of inactive branches are projected over the gaps and matched to the first node of new *MP* branches. There is a maximum permitted gap distance, specified by the *maxGap* parameter, and a minimum segment length requirement for the active *MP* that is to be connected, specified by the *minNewSegmentLength* parameter.

C.2 Algorithm Extension to Circular Scan Line Layouts

C.2.1 Rectangular versus Polar Coordinates

The application of M^3A has thus far been limited to parallel linear scan line layouts with detections and target structures mapped in the Cartesian coordinate system, $M^3A(x, y, depth)$. However, for some applications (such as mapping tree root systems), it may be more prudent to form a scan grid with concentric circular scans around a central hub (the tree stem) to maximize the potential for perpendicular intersection of the targets. The mapping algorithm is extendable to these scan layouts by employing a polar coordinate system, $M^3A(\rho, \theta, depth)$.

In the polar system, each point on a plane is determined by an angle and a distance. The distance to any given point is *rho* (ρ) and the angle of the radial to the point between 0 and 360 degrees is *theta* (θ).

M^3A operates in the polar system just as in the rectangular system: extrapolation boxes are formed and links are made between detections on adjacent scan lines. The extrapolations are still formed based on the *positionTravel* parameter, but the boxes are defined in ρ–*depth* instead of *x-depth*.

C.2.2 Simulated Circular Scan Line Example

To test and refine M^3A, hypothetical target structures were created with various features of the Experiment II pipe structure: the lengths of the target segments and the spacing between the segments were varied, segments were crossed, and segments were split into multiple branches. The algorithm robustly and accurately mapped these structures for both parallel linear and concentric circular scan lines.

One layout will be highlighted as an example (Fig. 66). Four circular scan lines at unit values of *rho* intersect three channels that originate at a common point ($\rho = 0$) and radiate directly outwards (*theta* stays constant as *rho* increases).

Perfect detection performance is assumed prior to applying M^3A, so the mapping procedure operates on the set of eight intersections of scan lines with channels (Fig. 67). The procedure uses the scan line data in order of increasing *rho* (first SL-1, then SL-2, and lastly SL-3).

The three detections in scan line 1 (SL-1) are referenced first. There are no possible matches because no *MP*s exist yet, so instead the detections are set as nodes of three new *MP*s (Fig. 68). Extrapolation volumes are projected radially outward from the origin through the SL-1 root nodes onto SL-2. The three SL-2 detections fall into these extrapolation boxes and are associated to their respective *MP*s (Fig. 69). Similarly, extrapolation volumes are projected from the SL-2 detection positions onto scan line 3 and the two SL-3 detections are associated (Fig. 70). The final result is three predicted *MP*s that match the initial positions and middle extents of the true channels (Fig. 71). There are errors, however, just as there are in the linear scan line example (refer to Fig. 36), where the algorithm did not capture the segment endings that fell between scan lines.

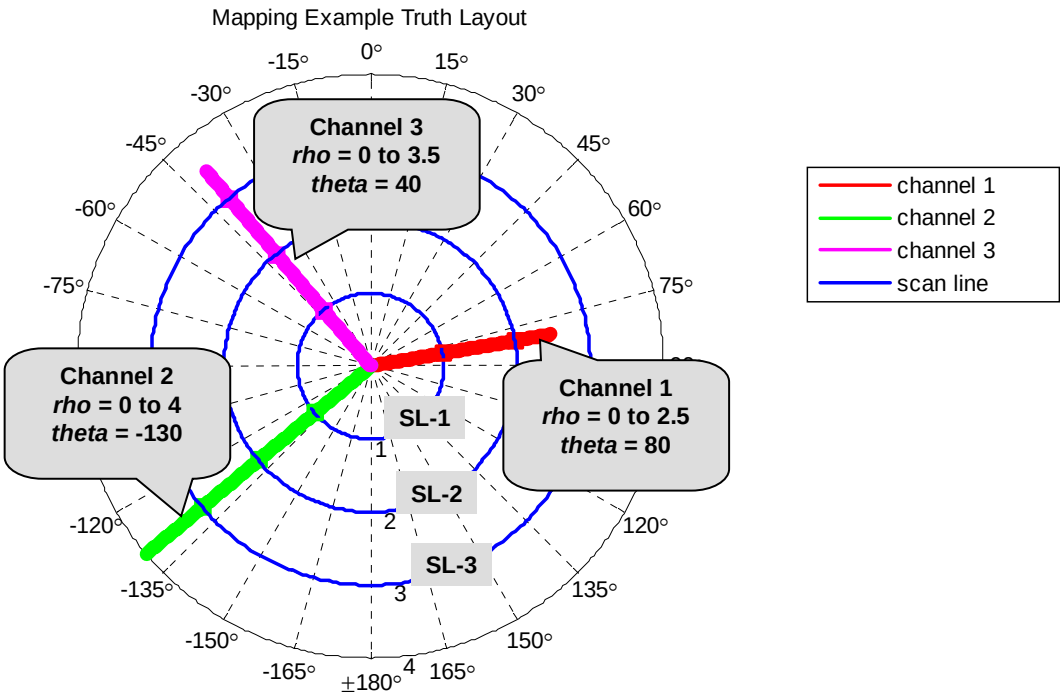

Figure 66. Circular scan line example in polar coordinates: a structure with three channels radiating outward from the center (*rho* = 0) and three B-scans.

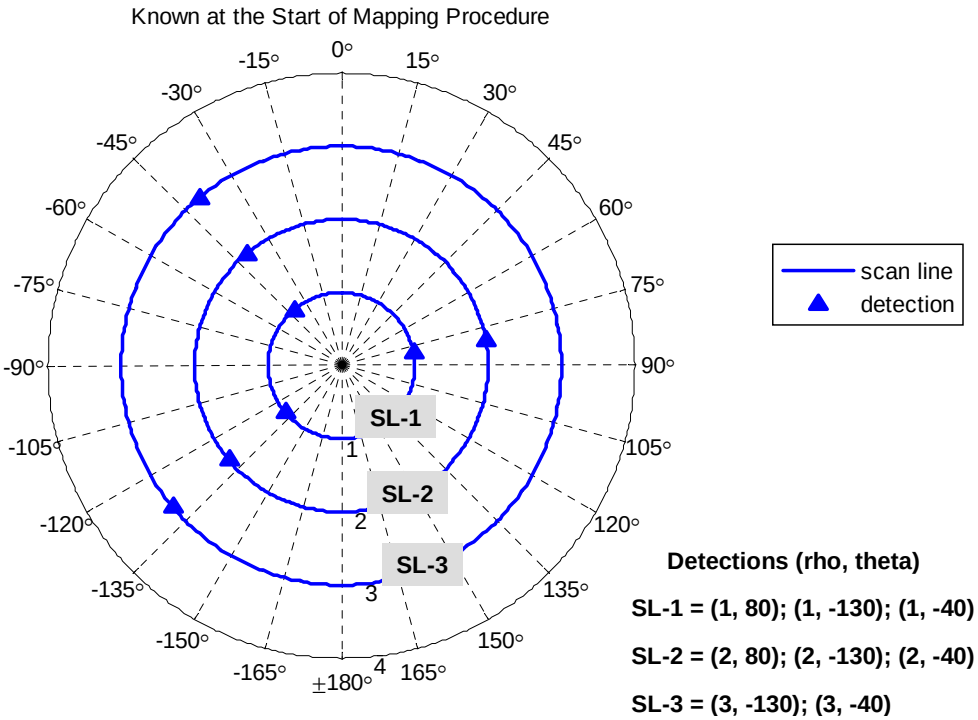

Figure 67. Known information at the start of the mapping analysis.

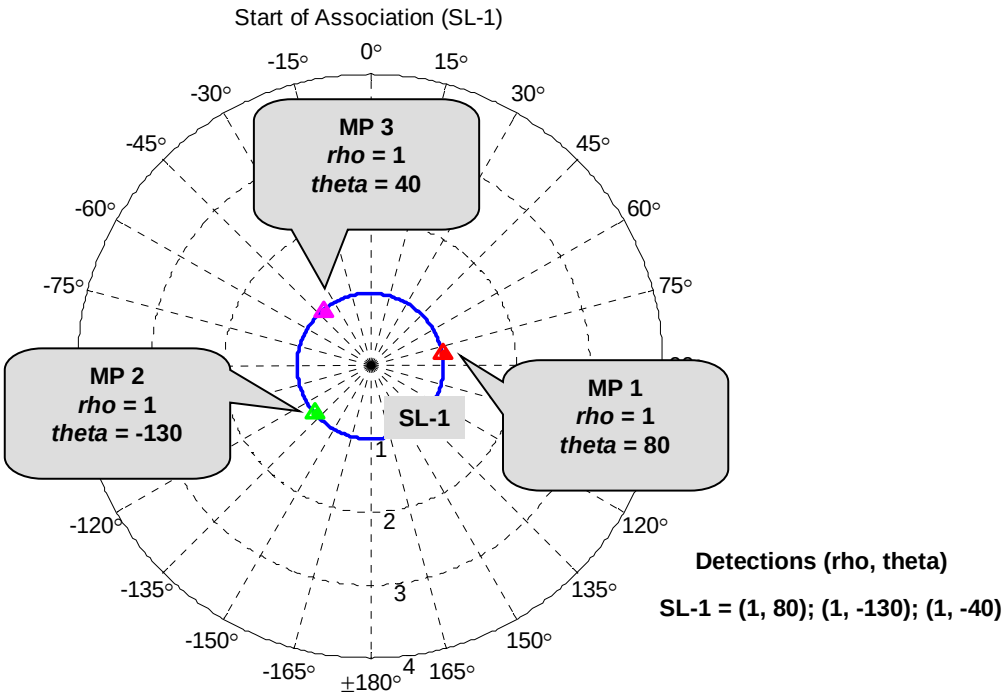

Figure 68. Mapping analysis starting with scan line 1 (SL-1). Each SL-1 detection is initialized as the first node of an MP.

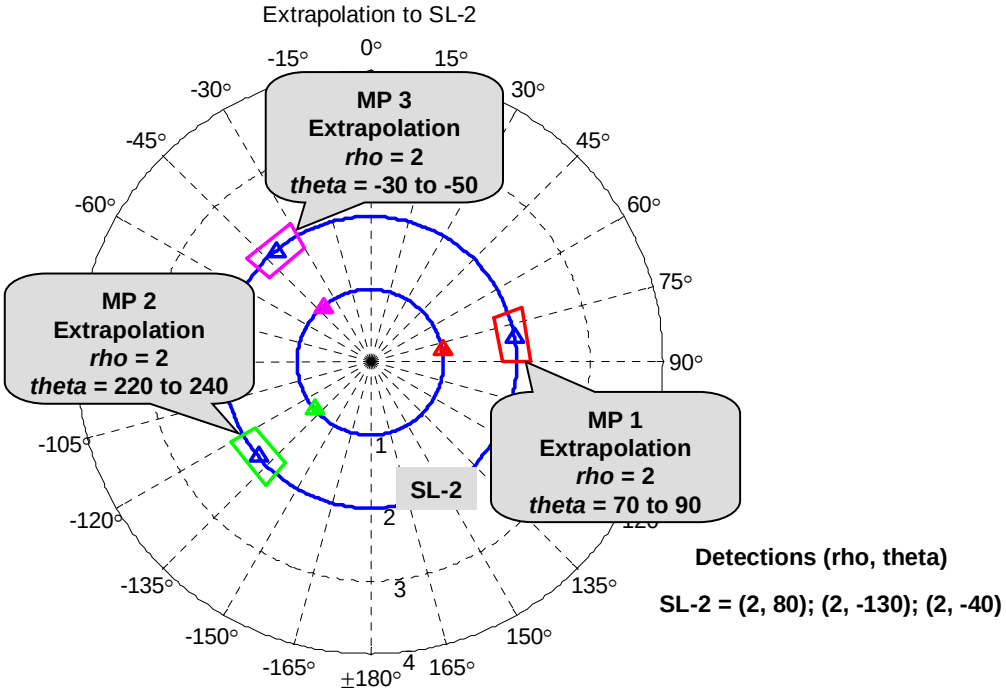

Figure 69. Mapping analysis on scan line 2 (SL-2). Extrapolation volumes are projected to SL-2 based on SL-1 and detections are matched to the extrapolations.

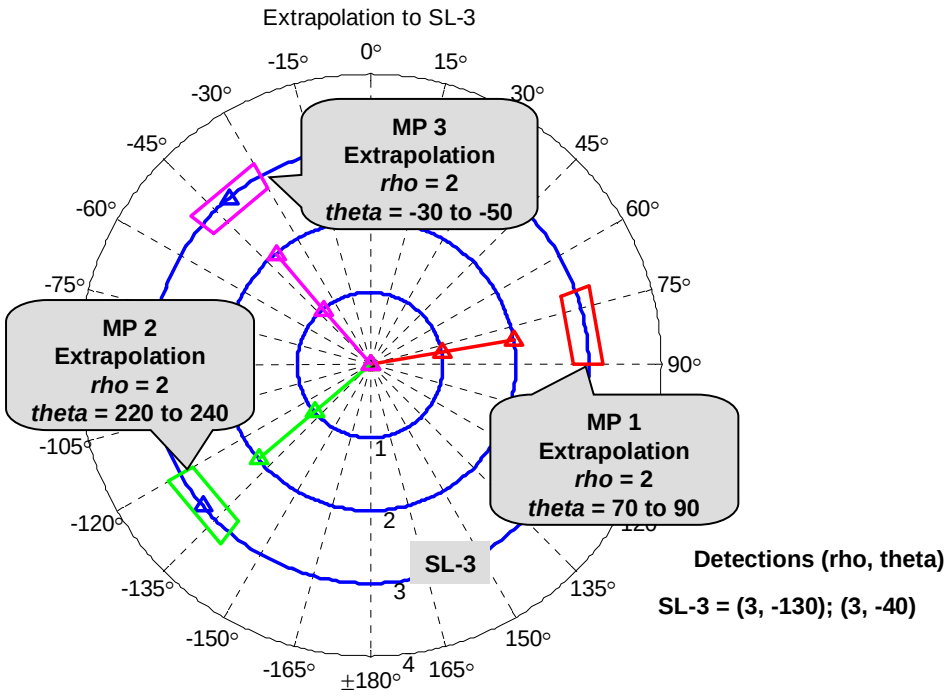

Figure 70. Mapping analysis on scan line 3 (SL-3). Extrapolation volumes are projected to SL-3 based on SL-2 and detections are matched to the extrapolations.

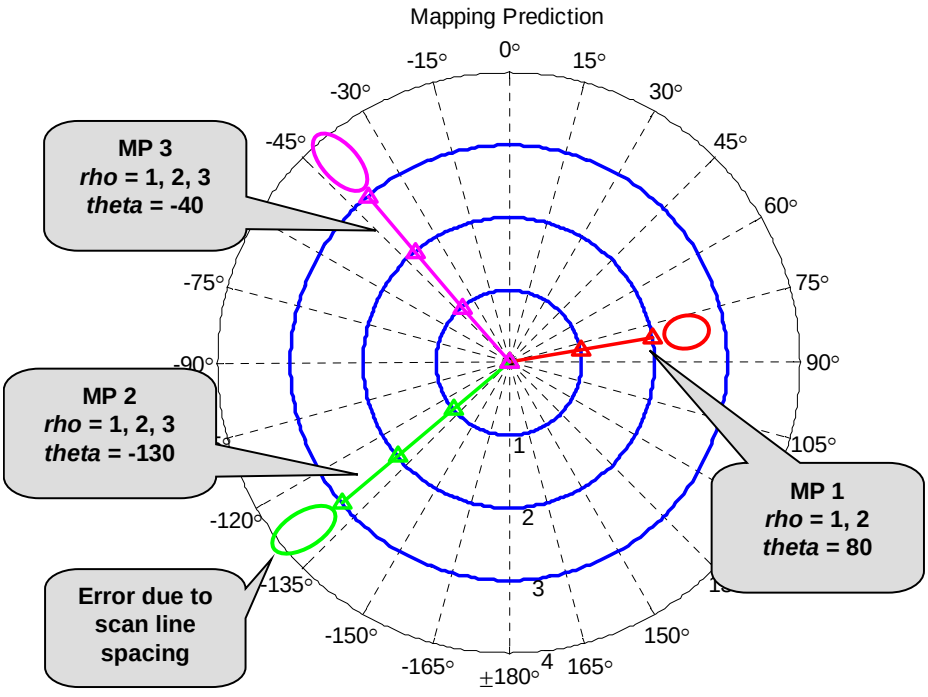

Figure 71. Subsurface structure prediction for the example layout. Errors are noted at the ends of the predicted channels.

C.3 Application of M^{3}A for Mapping Tree Roots

C.3.1 Introduction

One example of an additional application of M^{3}A is for mapping a tree's lateral structural root system. Roots in the top meter of the soil can be detected along concentric circular scan lines using the 900 MHz GPR antenna and mapped using the extension of M^{3}A for polar coordinates. Roots generally grow outward from the trunk so circular scan lines maximize the potential for intersecting the targets at perpendicular angles.

C.3.2 Literature Review

The application of GPR for non-invasive tree root detection is in its infancy, but several researchers have reported successes (Barton and Montagu, 2004; Butnor et al., 2001; Cermak et al., 2000; Cox et al., 2005; Dannoura et al., 2008; Hruska and Cermak, 1999; Niltawach et al., 2002; Stover et al., 2007; Wielopolski et al., 2002).

Many of these studies were performed in controlled conditions and relatively uncluttered soils (i.e., sand). Roots with diameters between 1 and 10 cm were detected under optimal conditions after cutting them into pieces and burying them in sand (Barton and Montagu, 2004; Cox et al., 2005; Dannoura et al., 2008). Dannoura et al. (2008) found that the critical factor for detection was the difference in water content between the roots and soil. Stover et al. (2007) showed a correlation between coarse scrub-oak root biomass and the summed amplitude of 1500 MHz GPR energy reflectance (R^2 = 0.68) in a fairly uncluttered sandy marine soil (Pomello type).

Researchers in the Czech Republic reported detections of tree roots in urban and forested soils as verified by air spade excavation (Cermak et al., 2000; Hruska and Cermak, 1999) but did not describe the detection methodology in detail. In a review of these results and others, Stokes et al. (2002) stated that GPR could be a valuable non-invasive sensing tool for arborists but that computer software is needed to analyze the raw scan data and construct 3D root architectures.

One option, albeit impractical, for performing these reconstructions is computed tomography techniques borrowed from biomedical applications (CAT-scans) (Heeraman et al., 1997; Pierret et al., 2002b). Wiepoloski et al. (2002) used very finely-spaced high-frequency GPR scan data to create three-dimensional images of small twigs (2.5 mm diameter) buried in sand.

C.3.3 Tree Root Mapping Examples

Two examples of oak trees scanned in grids of concentric circular scan lines (data provided courtesy of Tree Radar, Inc., Silver Spring, MD) are given for the application of the M^{3}A algorithm to map structural tree root systems. The first tree was located at the corner of Eastern Ave. and Piney Branch Rd. in Washington, D.C. (Fig. 72 a). A density plot of root detections (Fig. 72 b) was created using the following accumulation function based on Eq. [4-2] as described in Chapter 5:

$$D(\rho,\theta) = \sum_{k_1=-\rho w}^{\rho w} \sum_{k_2=-\theta w}^{\theta w} r(\rho + k_1, \theta + k_2) \qquad \text{[D-1]}$$

where D = plane of accumulation results;
r = *rho-theta* plane of root detections disregarding depth;
ρw = length of accumulation window in *rho*; and
θw = width of accumulation window in *theta*

The result of the M^{3}A algorithm was plotted in Fig. 73.

The second tree was located in Melbourne, Australia. Root detections were plotted along each scan line in unwrapped *theta-depth* space (Fig. 74 a), a "virtual trench" of the subsurface. *Theta* was unwrapped (θ_{uw}) to a normalized range of values between 0 and 1 by dividing by the maximum *theta* value (360 degrees, the angle of the ray to the scan line end point). A density plot of the detections (Fig. 74 b) in this space was created with the following accumulation function based on Eq. [D-1]:

$$Dvt(\theta_{uw}, d) = \sum_{k_1=-\theta w}^{\theta w} \sum_{k_2=-dw}^{dw} r_{sl}(\theta_{uw} + k_1, d + k_2) \quad \text{[D-2]}$$

where Dvt = plane of virtual trench accumulation results;
r_{sl} = unwrapped *theta-depth* plane of root detections for one scan line;
θw = width of accumulation window in *theta*; and
dw = length of accumulation window in *depth*

The result of the M^3A algorithm was plotted in Fig. 75.

C.3.4 Algorithm Limitations

The limitations of the tree root mapping application are: (1) performance is predicated on the accuracy of the detection procedure; (2) roots are detected within "line of sight" of the GPR sensor (directly under the antenna), which excludes vertically oriented tap roots; (3) only structural roots larger than approximately 1 cm in diameter will be detected, which excludes fine feeder roots; and (4) healthy versus diseased conditions cannot currently be distinguished (further research is required to determine whether these conditions exhibit different forms of reflections).

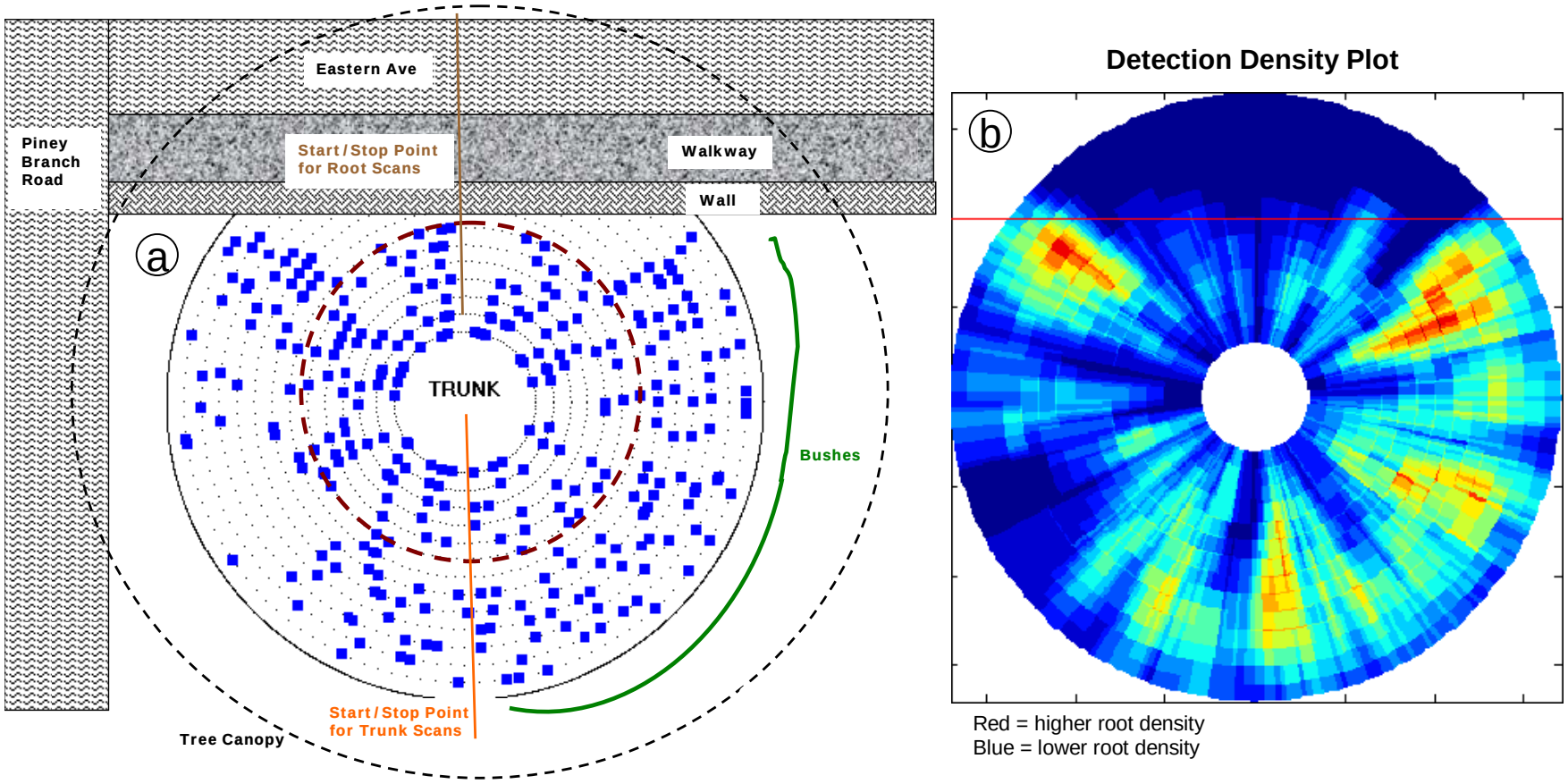

Figure 72. Example 1 of tree root mapping (Washington, D.C. oak tree). (a) Plan view of root detections along circular scan lines. (b) Detection density plot (density window size is 3 units of *rho* and 10 degrees of *theta*). (Data courtesy Tree Radar, Inc.)

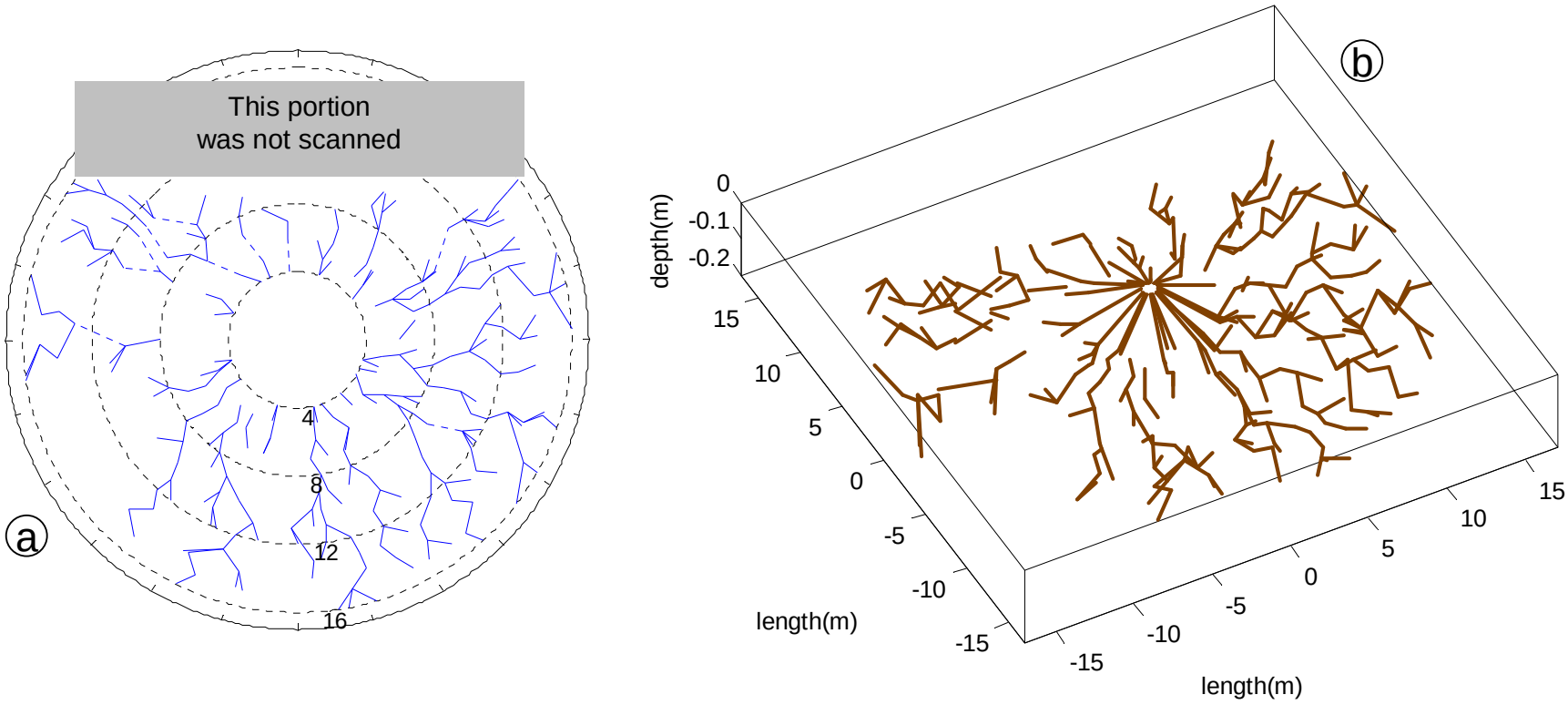

Figure 73. Example 1 tree root mapping results (Washington, D.C., oak tree). M^3A prediction plotted (a) in plan view and (b) in a three-dimensional view.

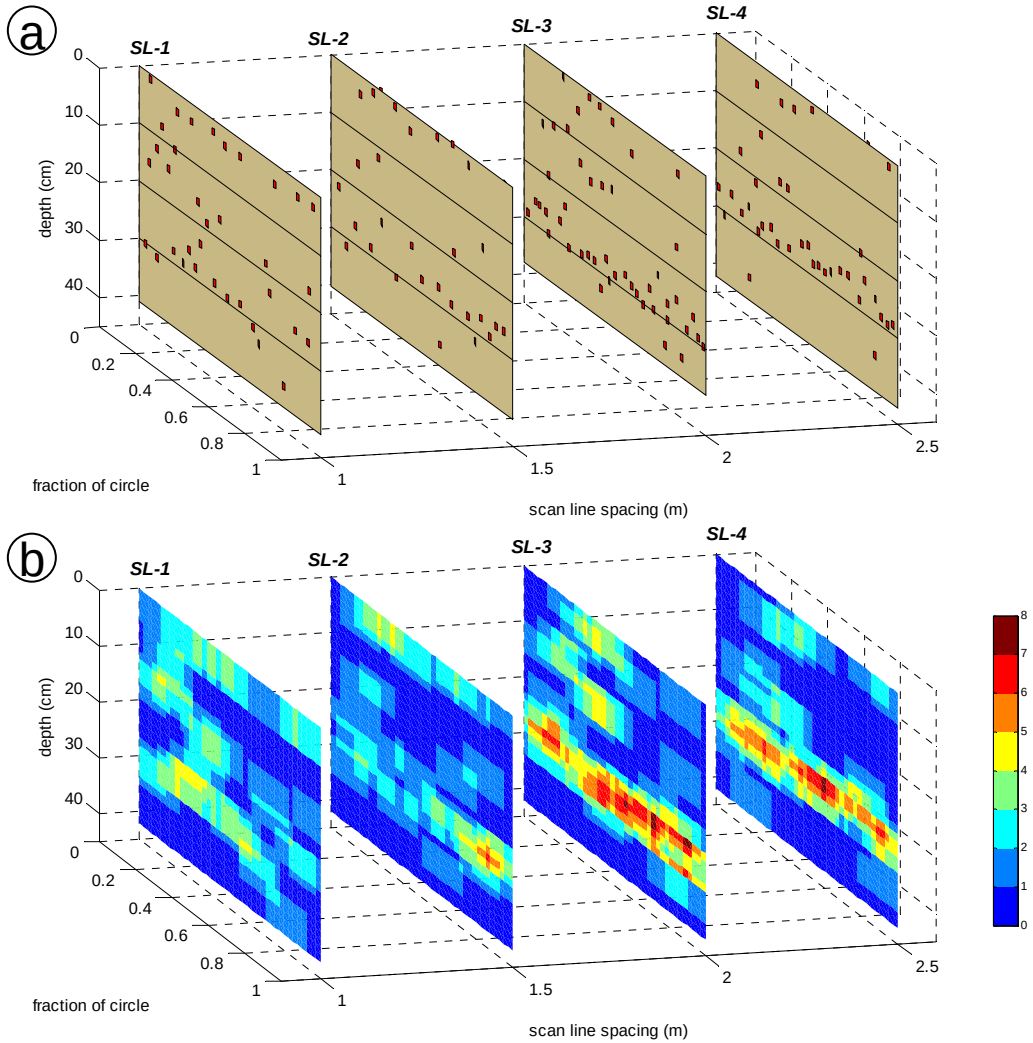

Figure 74. Example 2 of tree root mapping application (Melbourne, Australia oak tree). (a) Profile view of root detections along four circular scan lines (SL-1 thru SL-4) in positions unwrapped and normalized to a fraction between 0 and 1. (b) Detection density plot in position-depth planes. (Data courtesy Tree Radar, Inc.)

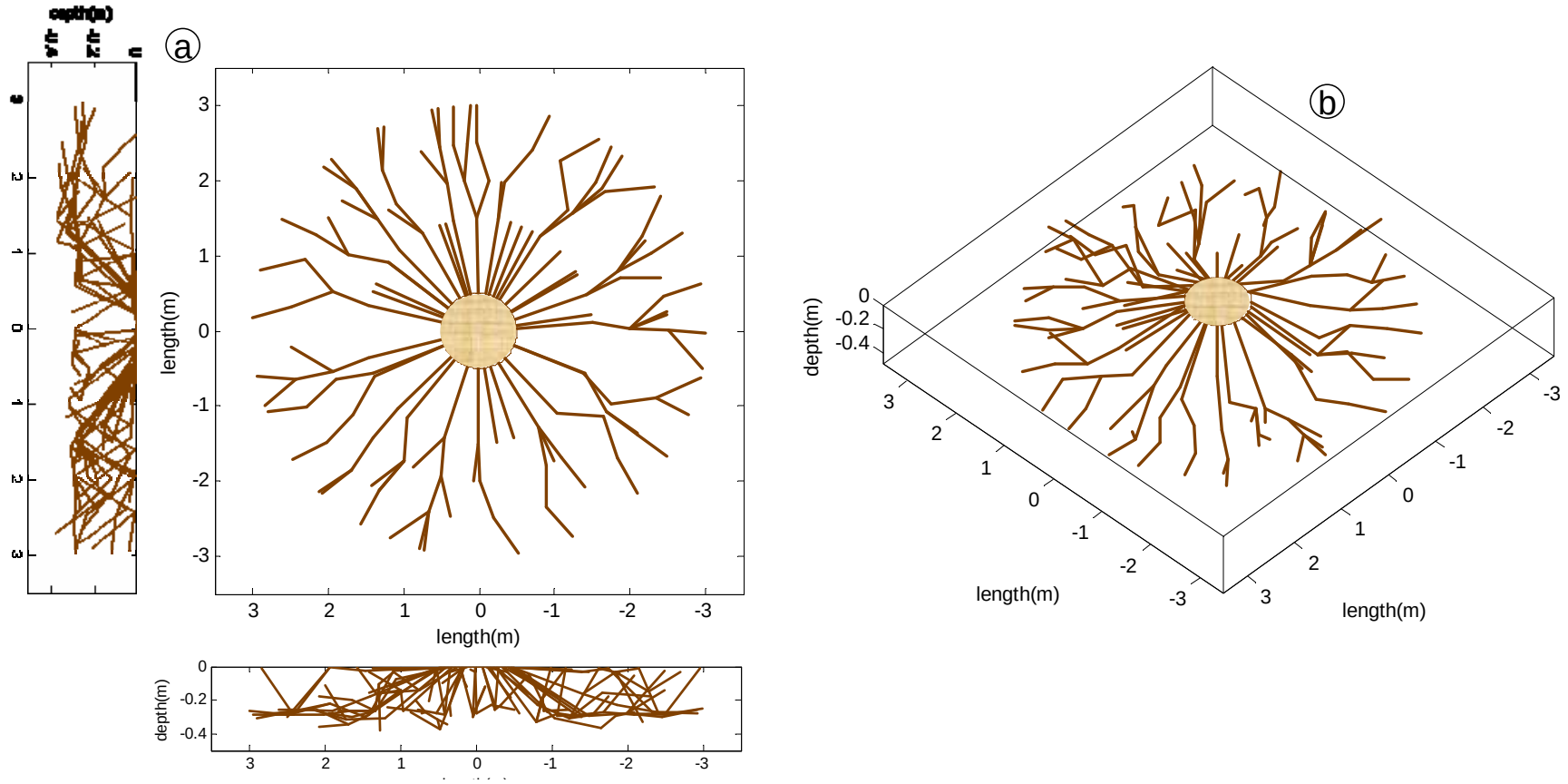

Figure 75. Example 2 tree root mapping results (Melbourne, Australia oak tree). M^3A prediction was plotted (a) in plan and profile views and (b) in a three-dimensional view.

C.3.5 Summary

The mapping algorithm developed for preferential flow channels can also be applied to predict the geometries of lateral structural tree root systems. Root system mapping with M^3A is a practical approach that stands in stark contrast to the high sampling requirements of tomographic-type reconstruction.

Studies can be performed to confirm the algorithm's accuracy by comparing the algorithm outputs to ground truth of the roots' actual lateral extent. The true root locations can be manually identified after excavating the root bowl using a tool like an air spade (Cermak et al., 2000; Hruska and Cermak, 1999; Stokes et al., 2002).

The density functions (Eq. [D-1], [D-2]) provide a means of calculating root biomass density. These functions, combined with assumed or predicted root diameters, can be used to compute *in situ* measurements of biomass which can be compared to reported experimental measurements (Butnor et al., 2003; Di Iorio et al., 2005; Kiley and Schneider, 2005; Purbopuspito and Van Rees, 2002; Sudmeyer et al., 2004; Wynn et al., 2004). These tools can also be applied to measure the ecosystem services provided by trees, including more accurate predictions of Carbon sequestration (Snowden et al., 2000; Wielopolski et al., 2002).

Appendix D: Experiment II Data

The performance of the manual and automated detection procedures for each Experiment II scan line is compiled in Table 15. The number of correct detections (*d*), false alarms (*fa*), and number of total detection cells (*ngc*) and correctly predicted empty detected cells (*np*) are listed.

Table 15. Experiment II manual and automated detection performance per scan. *p* = number of possible detections; *d* = number of detections; *fa* = number of false alerts; *ngc* = number of grid cells with no truth present; *np* = number of empty grid cells with no detections. ($<>_M$ = manual metric value, $<>_A$ = automated procedure metric value)

Scan Line	*p*	d_M	d_A	fa_M	fa_A	*ngc*	np_M	np_A
SL-28	0	0	0	0	0	100	100	100
SL-29	0	0	0	0	0	100	100	100
SL-30	1	1	1	0	0	104	104	104
SL-31	2	2	1	0	0	103	103	103
SL-32	3	2	1	0	0	97	97	97
SL-33	2	2	2	0	0	98	98	98
SL-34	3	3	2	0	1	97	97	96
SL-35	5	4	3	0	0	95	95	95
SL-36	4	4	4	0	0	96	96	96
SL-37	3	3	2	0	1	97	97	96
SL-38	1	1	1	0	0	99	99	99
SL-39	0	0	0	0	0	100	100	100
All(12)	24	22	17	0	2	1186	1186	1184

The GPR scan line data were plotted (Fig. 76-79) with a constant gain factor of 5 and a background removal filter (Eq. [3-2]) applied. The true positions of the pipe structure, manually identified reflection hyperbola apexes, and detections by the automated algorithm were noted within each scan.

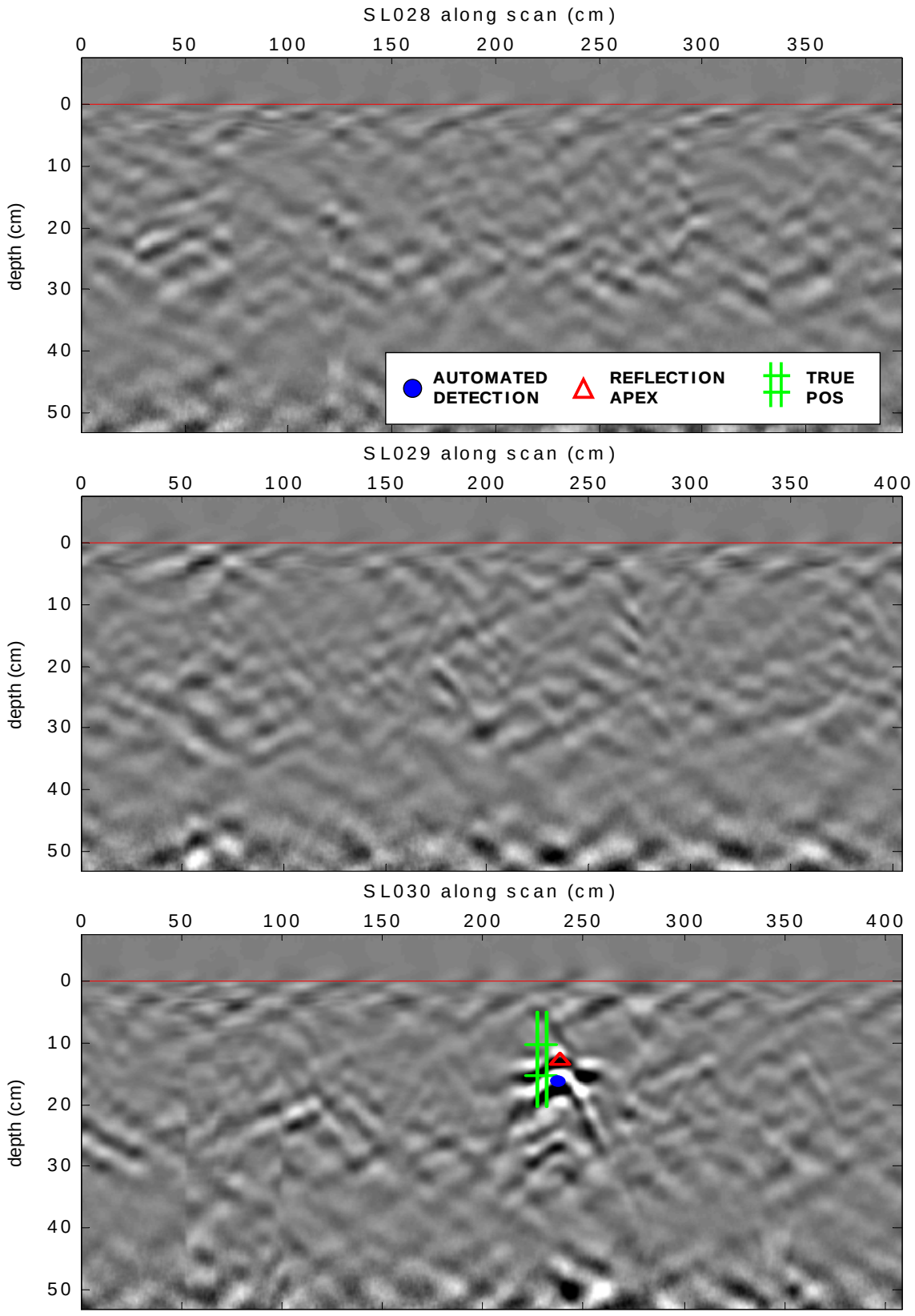

Figure 76. Experiment II scan line data (SL-28, 29, 30) with truth and predictions.

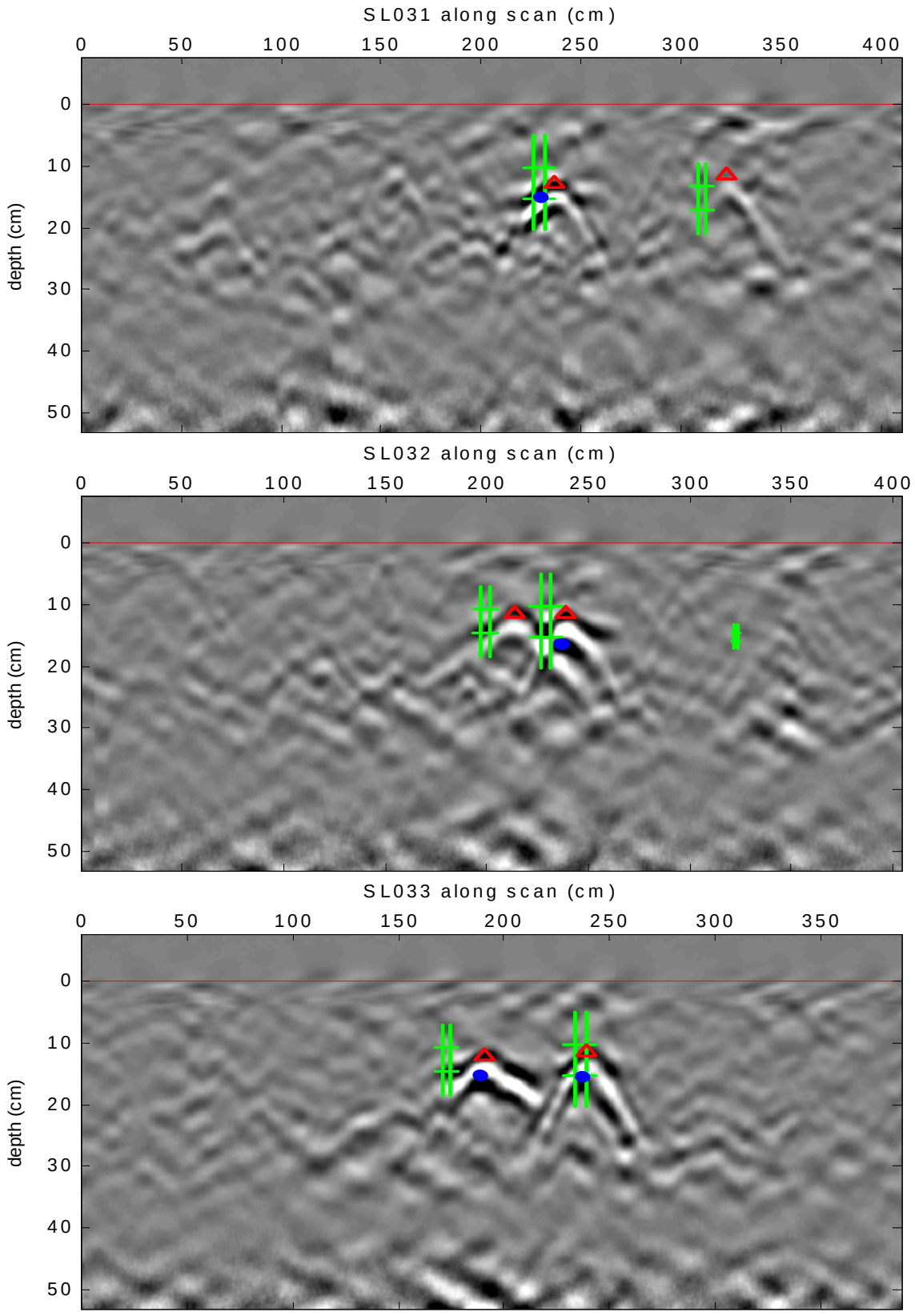

Figure 77. Experiment II scan line data (SL-31, 32, 33) with truth and predictions.

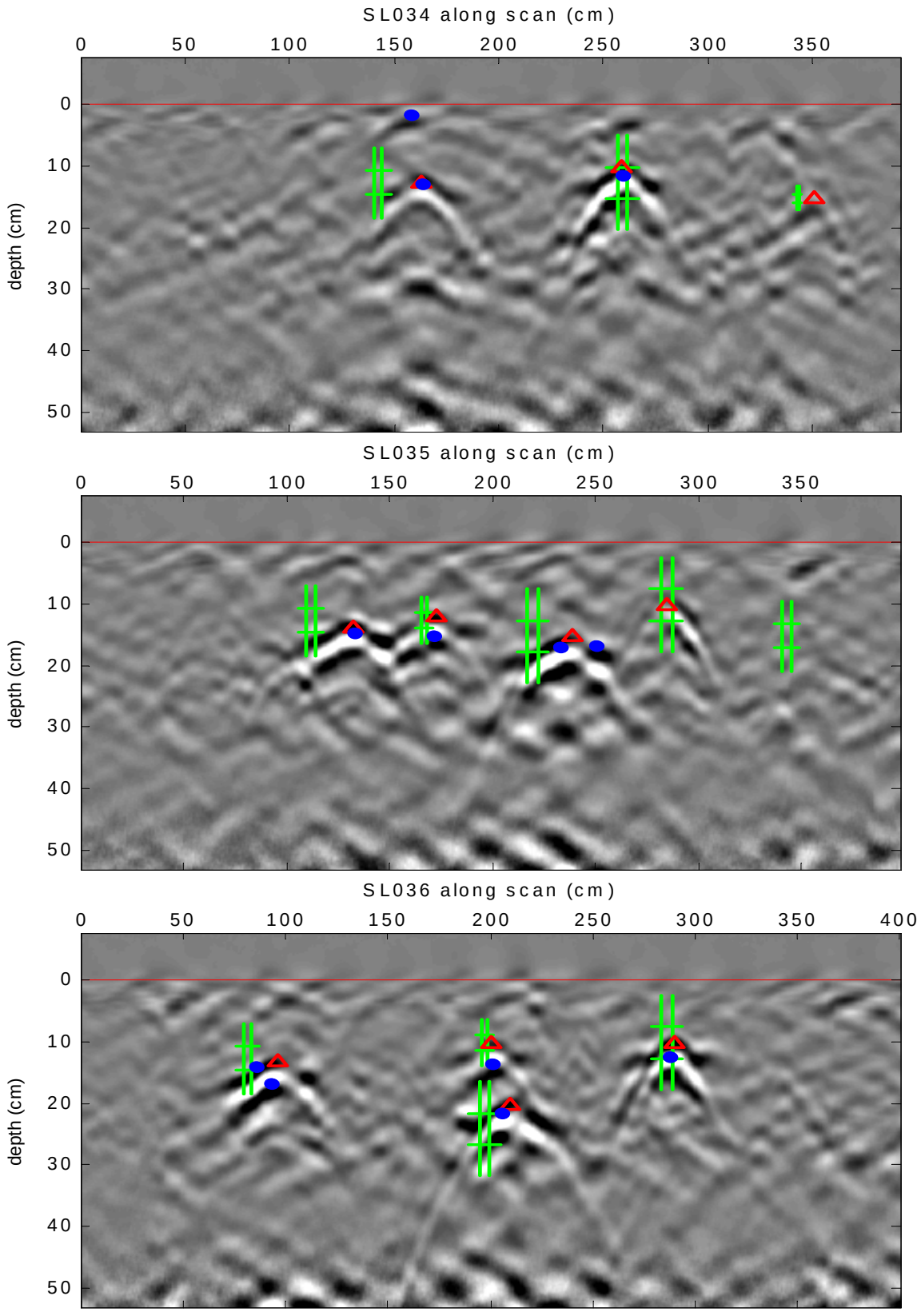

Figure 78. Experiment II scan line data (SL-34, 35, 36) with truth and predictions.

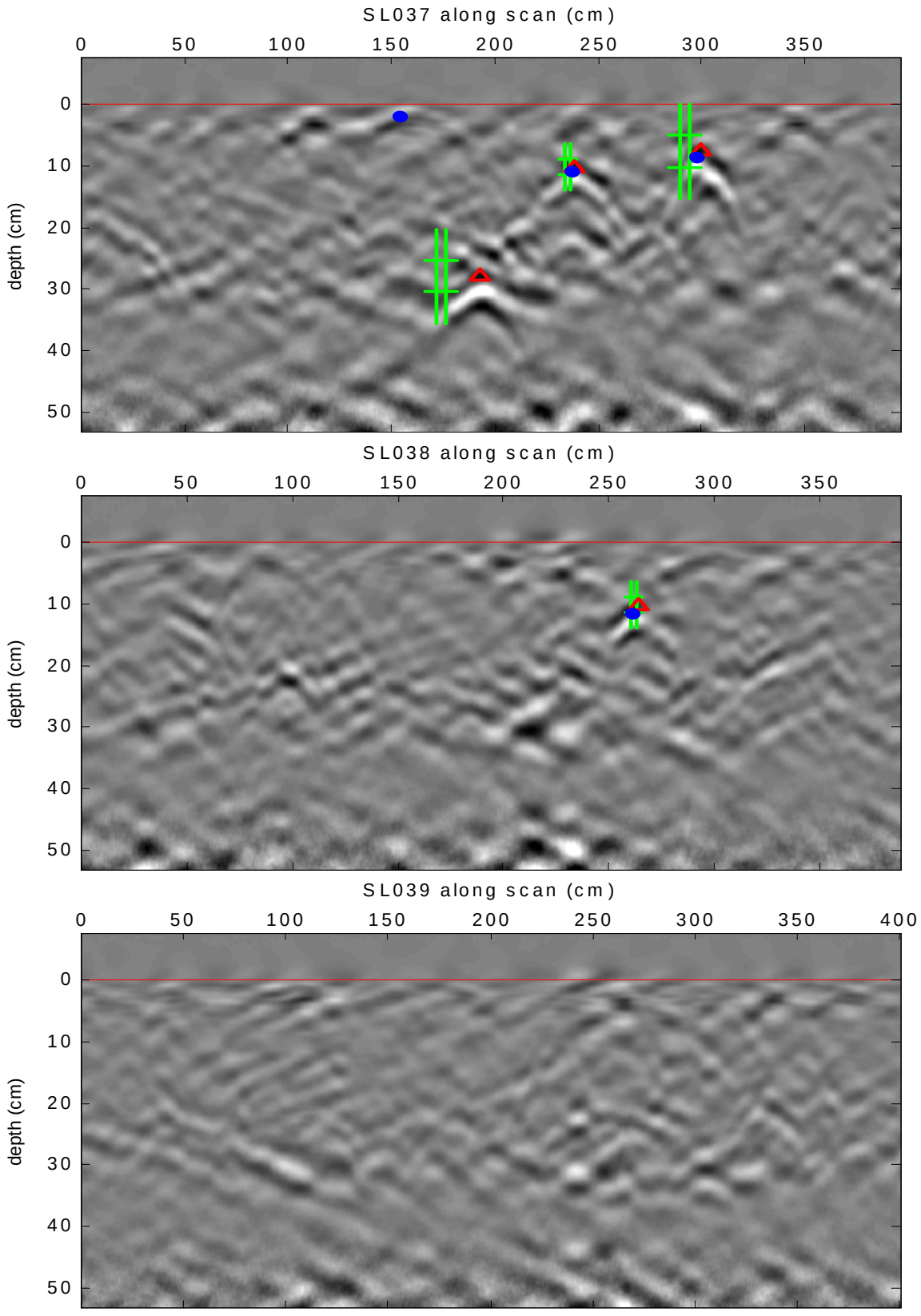

Figure 79. Experiment II scan line data (SL-37, 38, 39) with truth and predictions.

Appendix E: Experiment III Data

Plots were created for each of the filtered GPR scan lines in Experiment III (Fig. 80-83). All recorded waveforms and depth samples were plotted with a constant gain factor of 5 and a background removal filter (Eq. [3-2]) applied. Channel detection locations (from both the manual and automated procedures) and ground truth core sample locations are plotted on top of the scan data images. In addition, the locations of pore spaces identified within the cores are denoted for comparison to the scan and detections.

Pictures of the soil cores were compiled according to group number in Fig. 84-89.

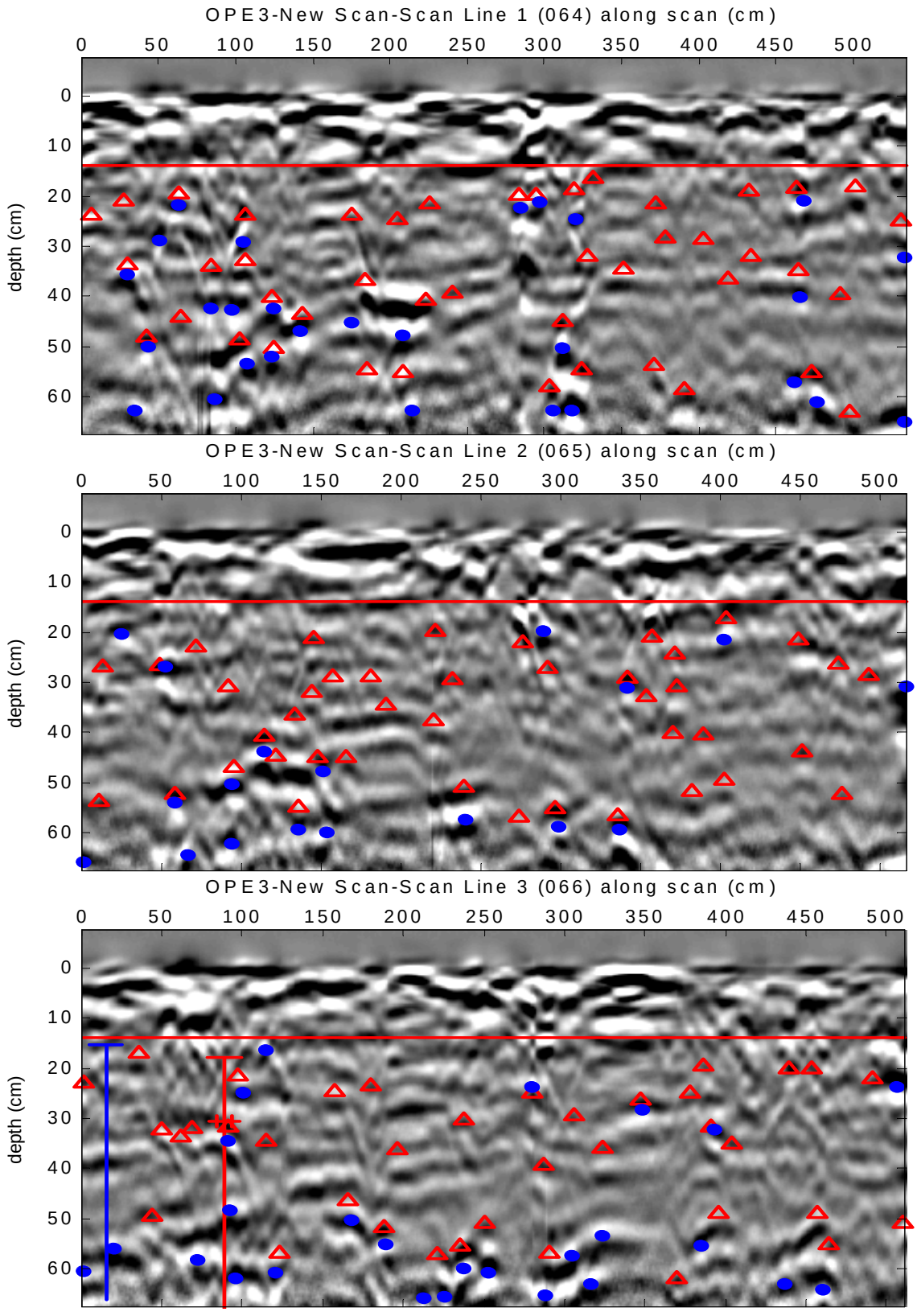

Figure 80. Experiment III scan line data (SL-1 , 2, 3) with truth and predictions.

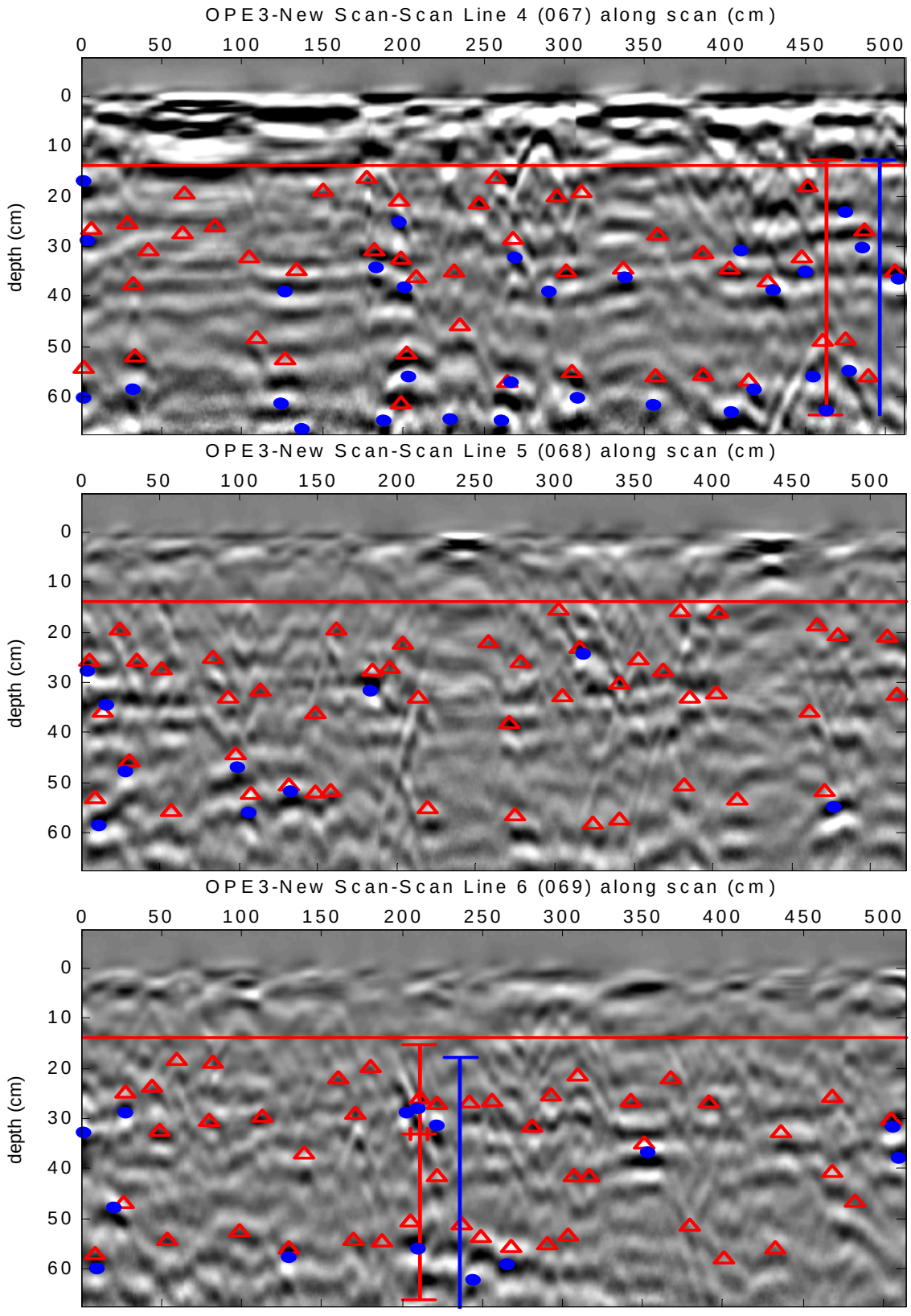

Figure 81. Experiment III scan line data (SL-4, 5, 6) with truth and predictions.

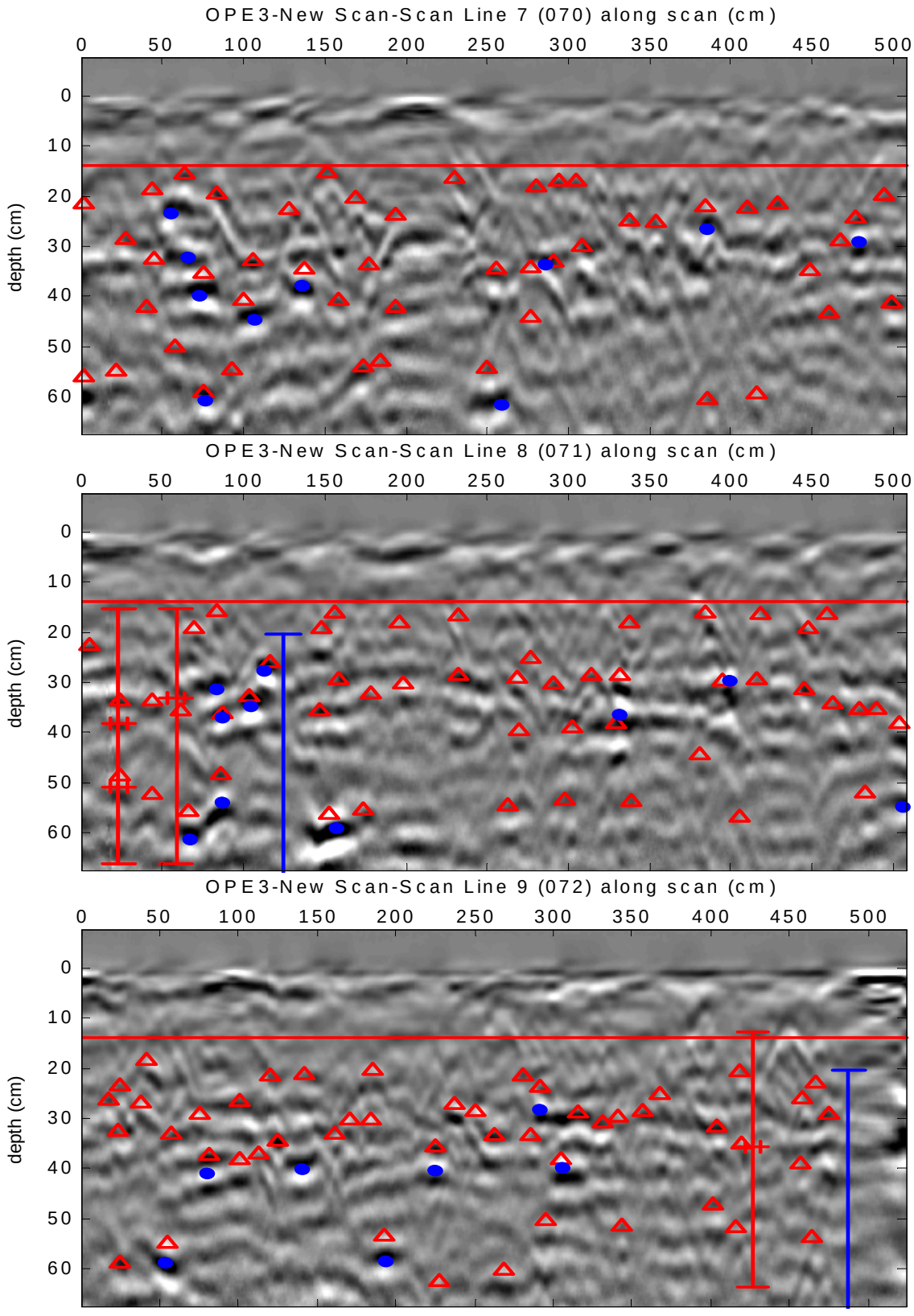

Figure 82. Experiment III scan line data (SL-7, 8, 9) with truth and predictions.

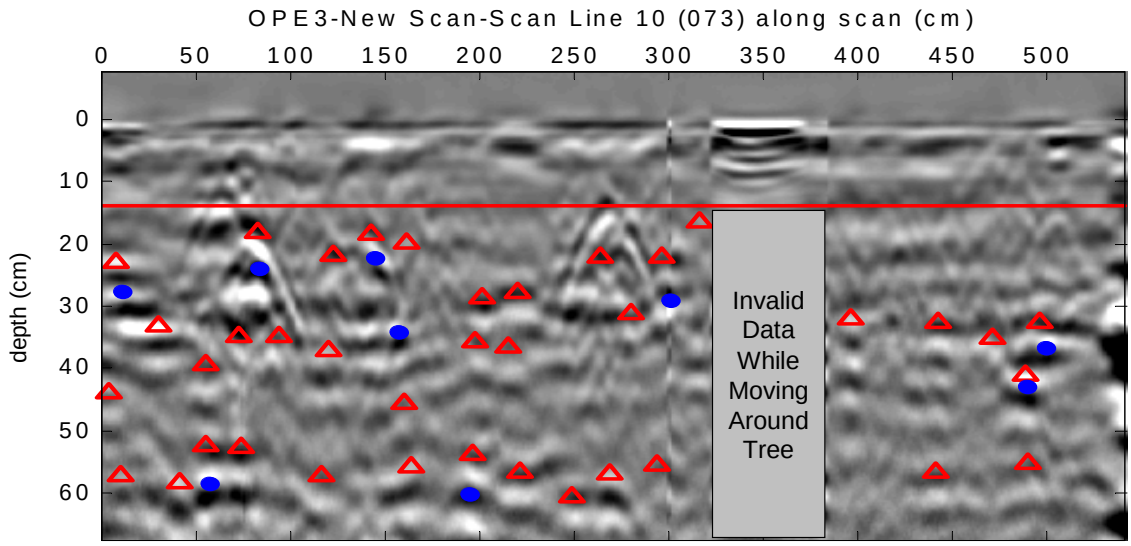

Figure 83. Experiment III scan line data (SL-10) with truth and predictions.

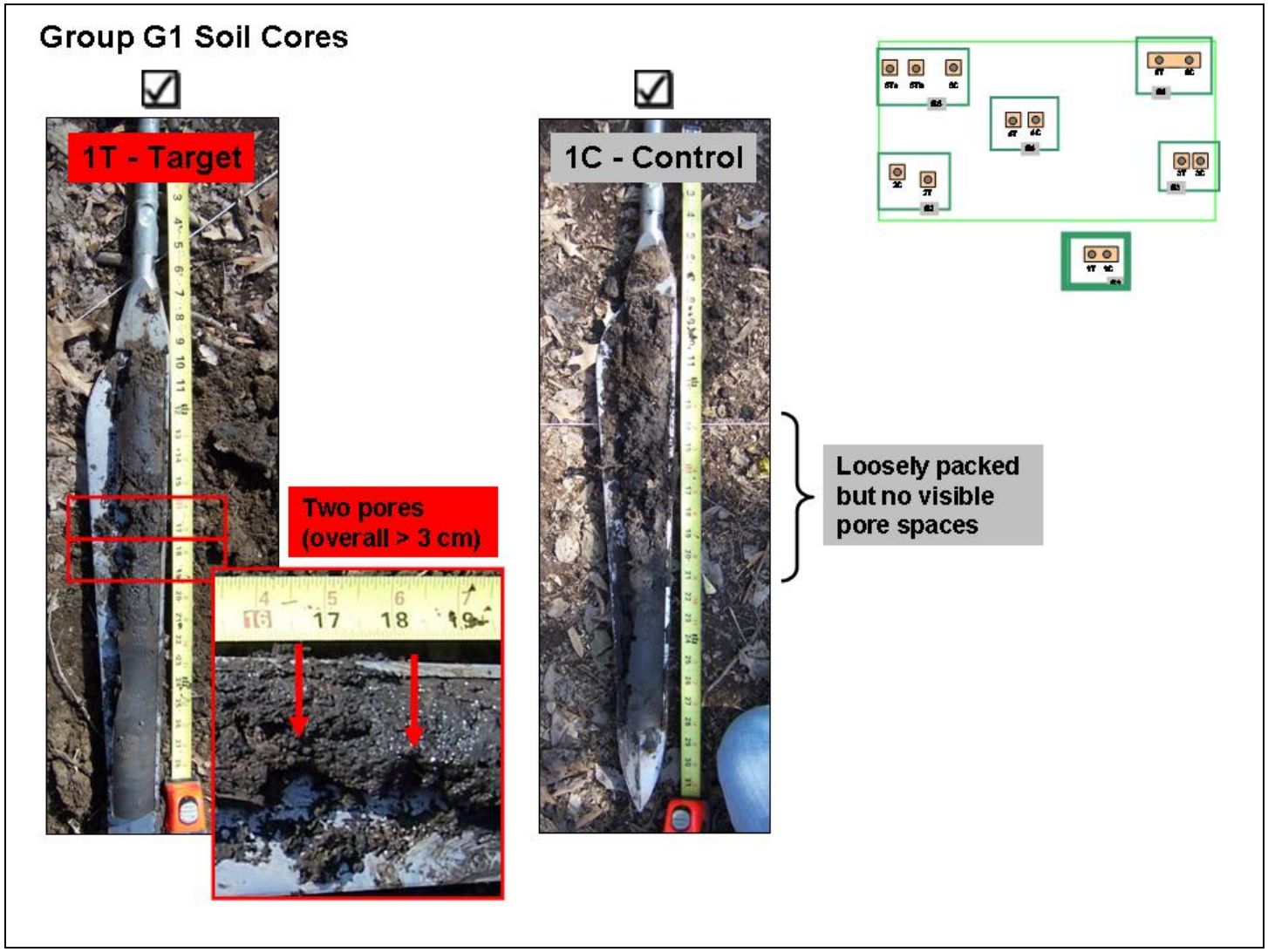

Figure 84. Group G1 target (1T) and control (1C) cores.

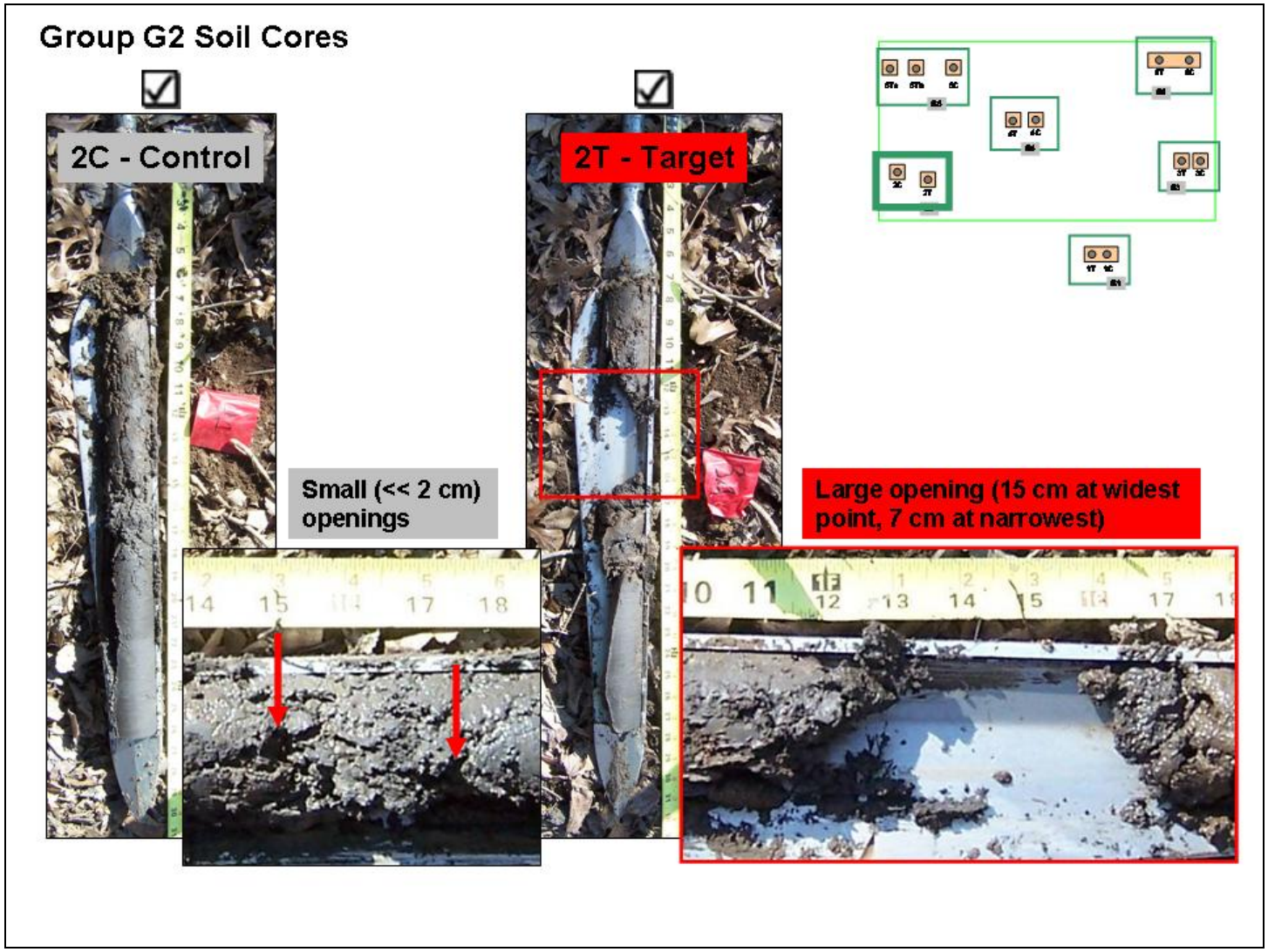

Figure 85. Group G2 control (2C) and target (2T) cores.

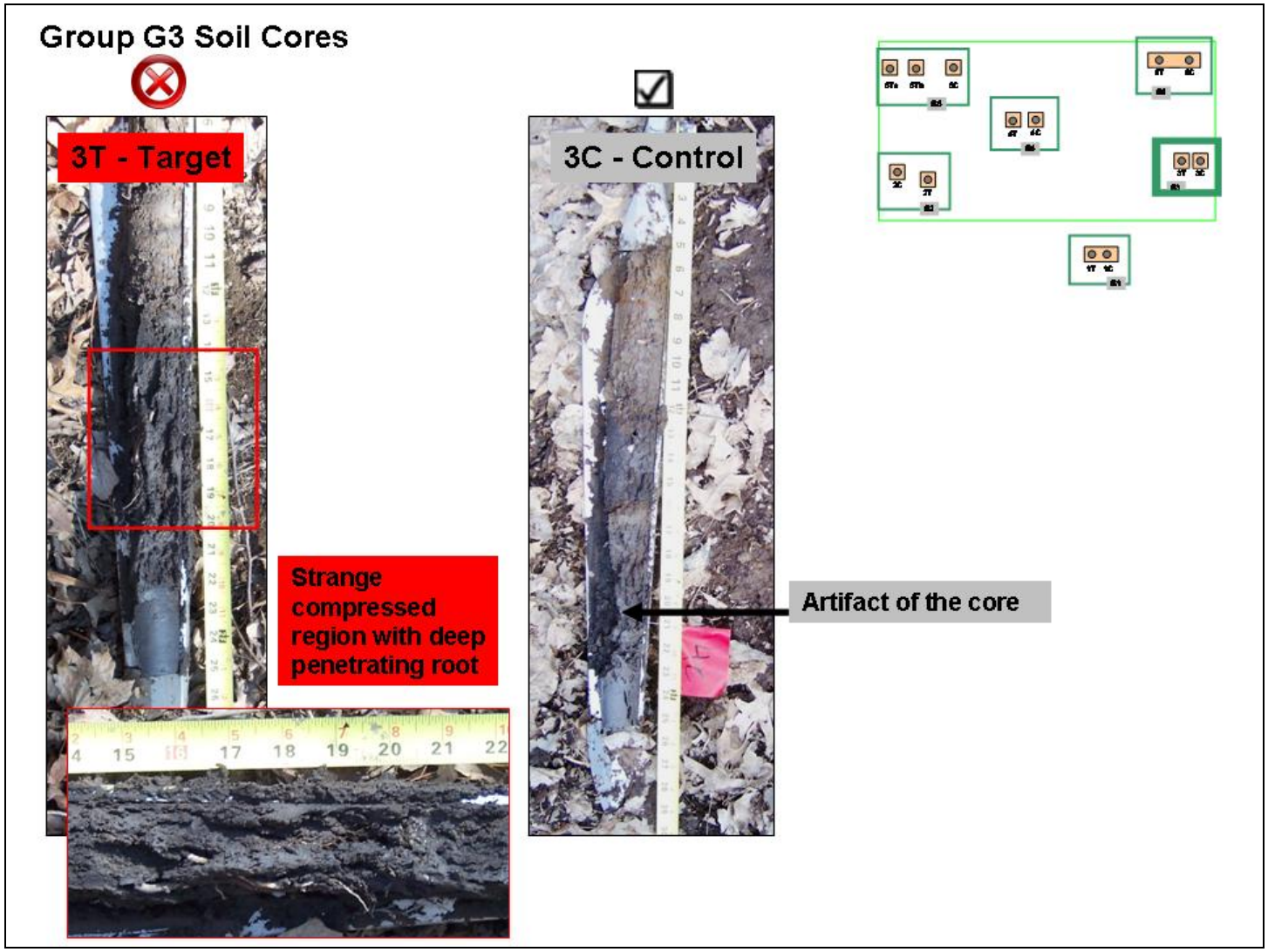

Figure 86. Group G3 target (3T) and control (3C) cores.

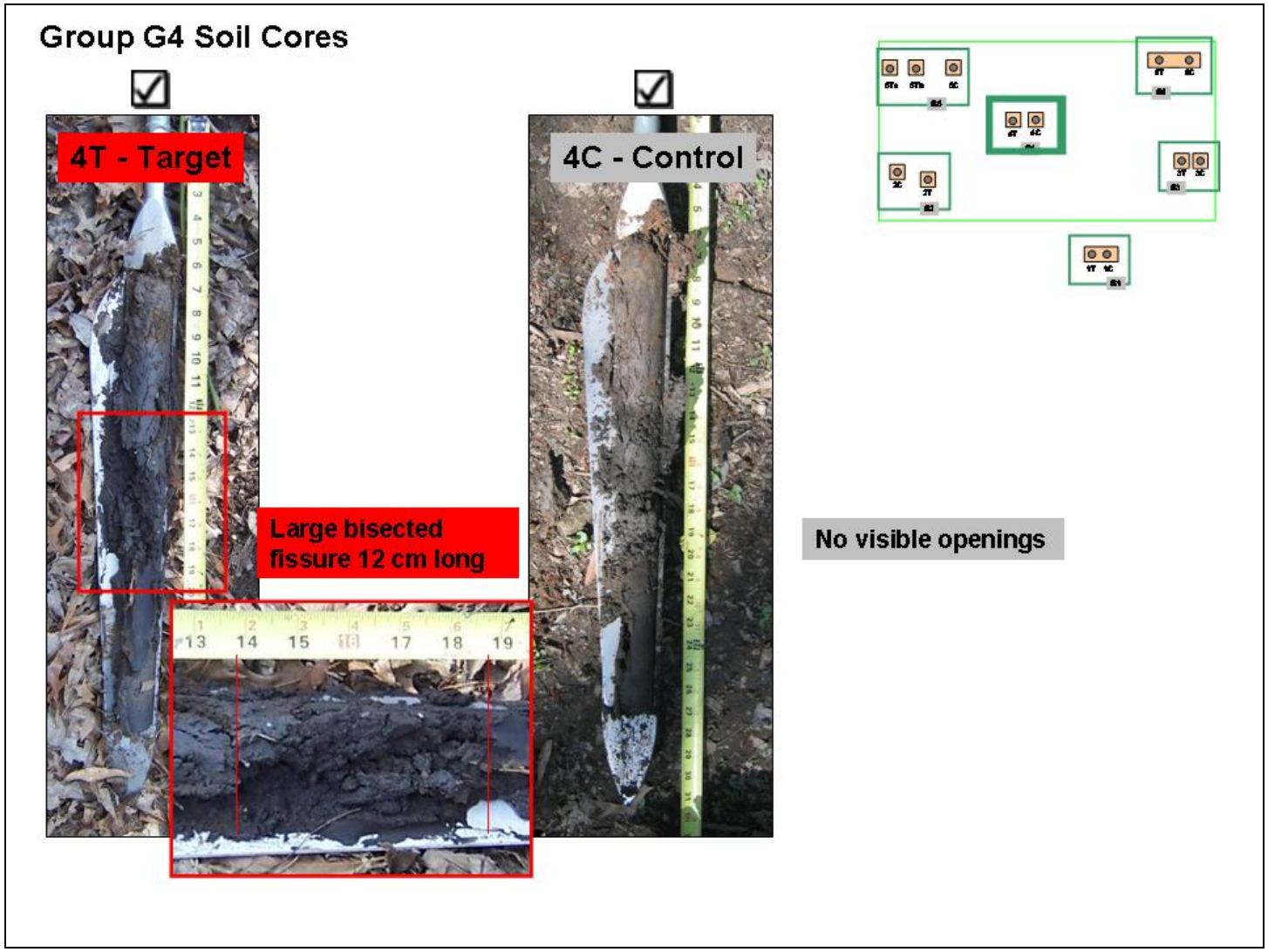

Figure 87. Group G4 target (4T) and control (4C) cores.

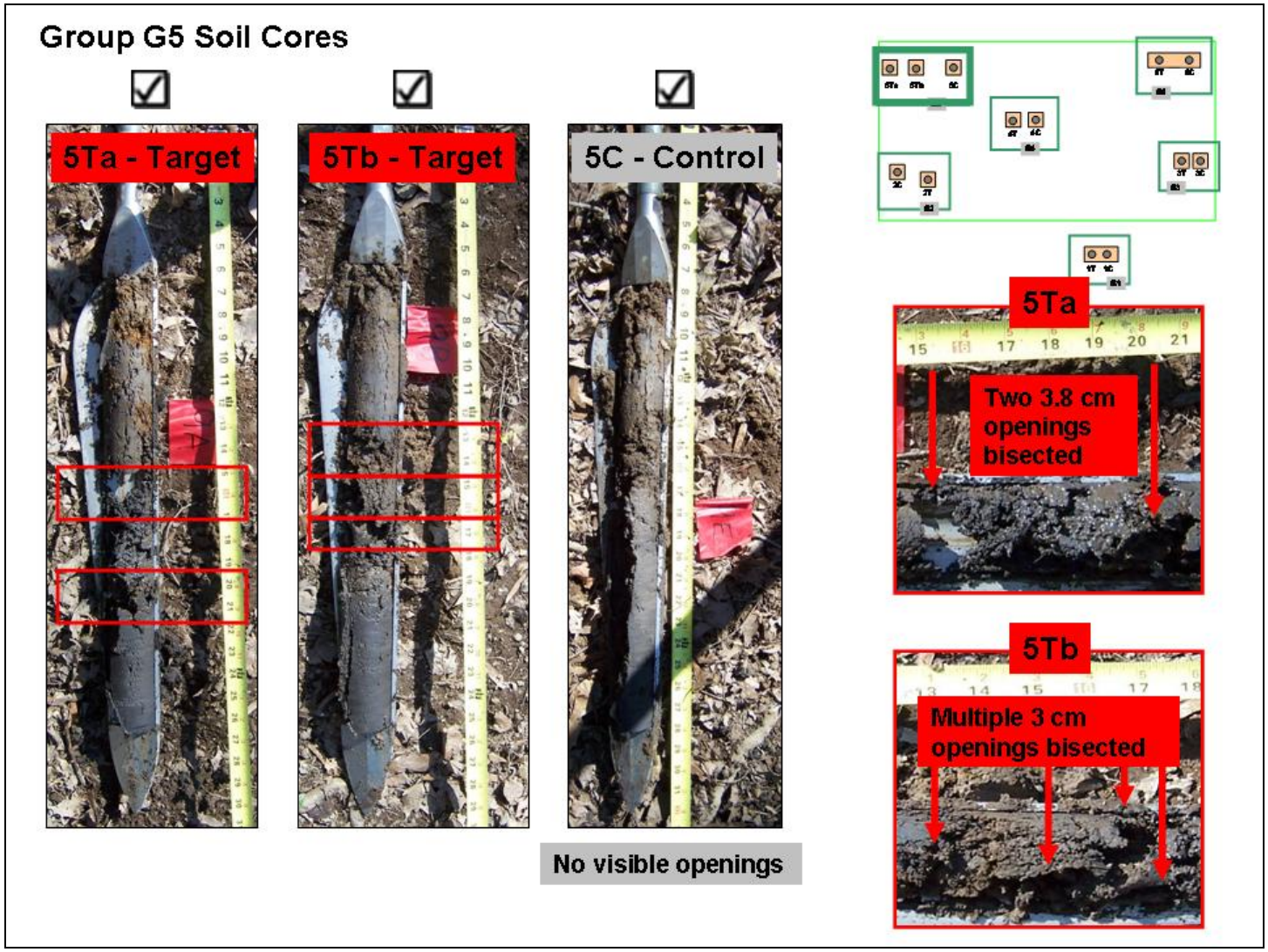

Figure 88. Group G5 target (5Ta, 5Tb) and control (5C) cores.

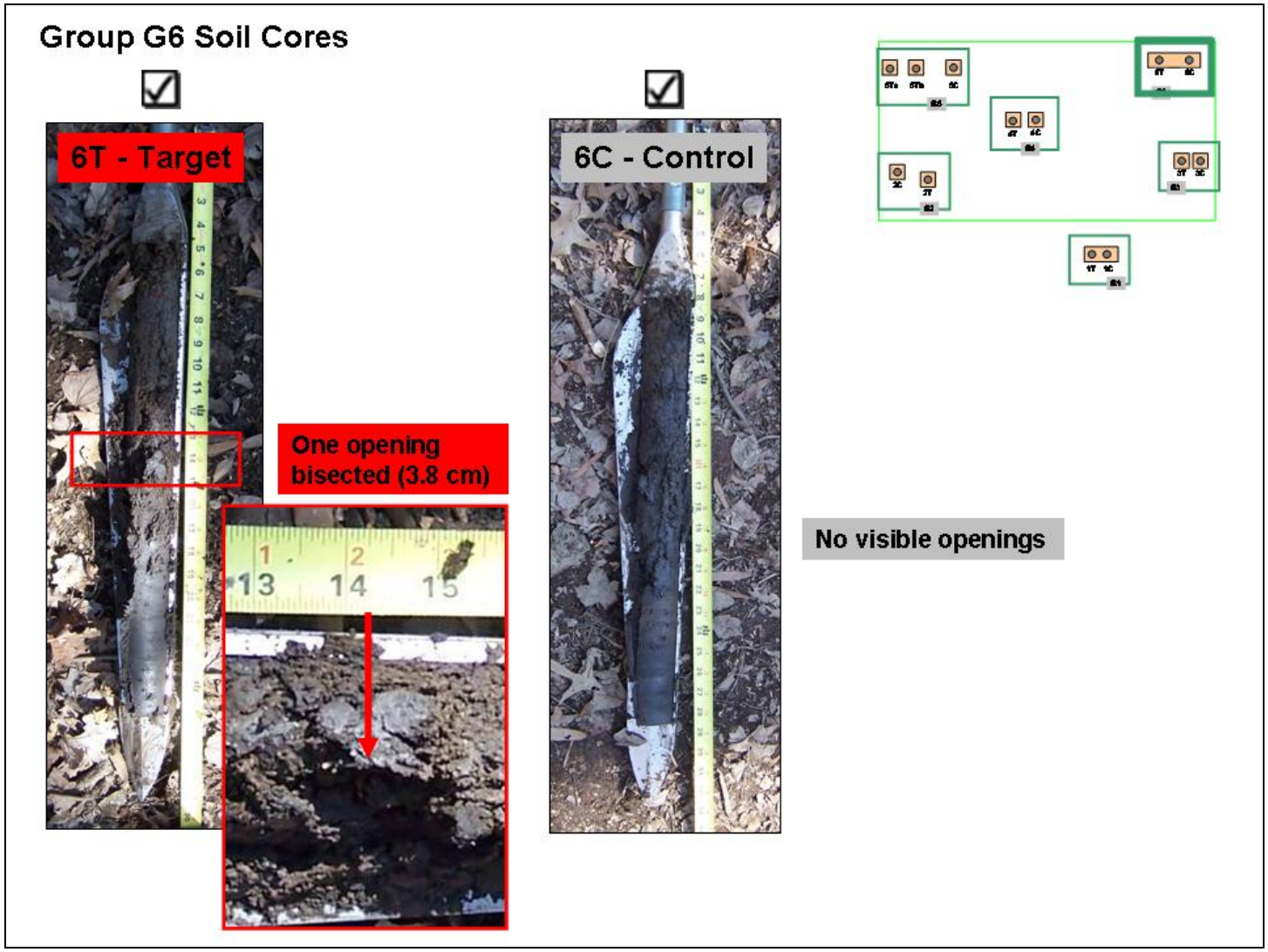

Figure 89. Group G6 target (6T) and control (6C) cores.

Appendix F: OPE^3 Soil Layer Mapping

F.1 Introduction

The Experiment III B-scan data was examined to detect transitions between soil layers in OPE^3, including the "post-settlement" deposit. Soil layer boundaries were detected in the 10 OPE^3 GPR scan lines and the results were verified by comparing the estimates to visual inspections of the soil cores.

F.2 Literature Review

GPR has been used to detect and map soil structures like the water table (Doolittle et al., 2006),(Gish et al., 2002) a clay lens (2005), and various strata and deposits (Adetunji et al., 2008; Bayani Cardenas and Zlotnik, 2003; Bowling et al., 2005; Conyers, 2004; Kung and Lu, 1993; Martinez et al., 1998; Szuch et al., 2006; van Dam et al., 2002). These structures were mapped over large field study sites by identifying constant reflected energy bands in GPR B-scans and correlating the reflections to physical measurement of the depths to the structures (i.e., using soil cores or pits).

F.3 Layer Detection Methods

Soil layer boundaries are planar structures that are roughly parallel to the surface and have a lateral extent far larger than the footprint of the GPR sensor. Therefore, GPR energy is reflected along a scan line at a roughly constant depth and amplitude (Fig. 7 a).

The constant bands of reflected energy were identified two ways: (1) a visual examination of the GPR B-scan image, and (2) using a detector based on the mean amplitude across the scan line. The visual method was described in Chapter 3 for the equivalent problem of detecting the reflections from pipes oriented parallel to the GPR scan line. The detector method (Eq. [F-1]) integrates the scan amplitude for each of the n_s depth samples and applies a threshold (τ) to the result. The mean amplitude was calculated across the n_A A-scans that make up the B-scan (Y). Recall this is the form of the definition for the noise model of the background removal filter (Eq. [3-3]). Integrated versions of the 10 Experiment III scan lines were computed to compare the depths of the band features across the study site.

$$\left| \frac{\sum_{i=1}^{nA} Y_{i,j}}{n_A} \right| > \tau ; \quad j = 1,...,n_s \qquad \text{[F-1]}$$

F.4 Results

Four banding type signals were present in the Experiment III scan data at depths of approximately 0, 10, 30, and 60 cm. The first (depth = 0 cm) was the ground coupling signal from the air/surface interface. The second (depth = 10 cm) likely corresponded to the transition between the unsaturated surface soil layer and first saturated layer; this was observed during field excavations but could not be verified with the soil cores that sampled at a deeper depth range (starting at approximately 15 cm). The last two banding signals (depth = 30, 60 cm) corresponded to changes in the texture, density, and color of the soils seen in the core samples. Scan line 3 is given as an example (Fig. 90).

The depths of the bands trended slightly deeper from the first scan line to the last, consistent with the slope of the study site: the position of Scan Line 10 on the hill slope was slightly higher in elevation than that of Scan Line 1 (Fig. 91).

F.5 Conclusion

GPR can be used to map the depths of soil layers in OPE^3 and other wetland areas. Researchers can use this technique to study soil structures and determine relationships between those soils and site hydrology and biology.

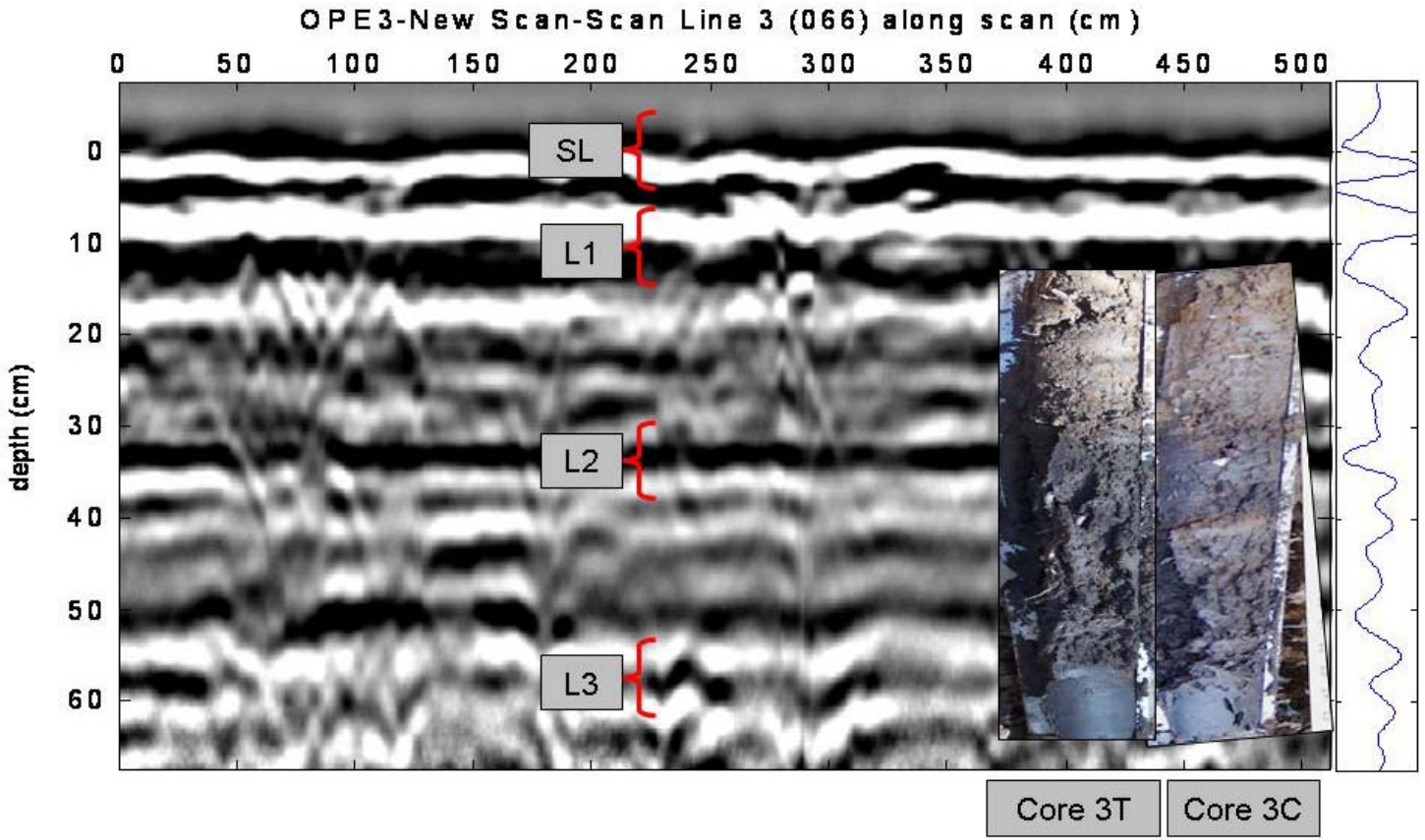

Figure 90. Experiment III B-scan data with annotations of constant reflected energy bands corresponding to soil layer boundaries. The plot on the right is the result of the detector in Eq. [F-1]. SL = air/surface coupling signal, L1 = soil layer boundary 1, L2 = soil layer boundary 2, and L3 = soil layer boundary 3. Core samples (3T, 3C) from this scan line are also shown aligned in depth.

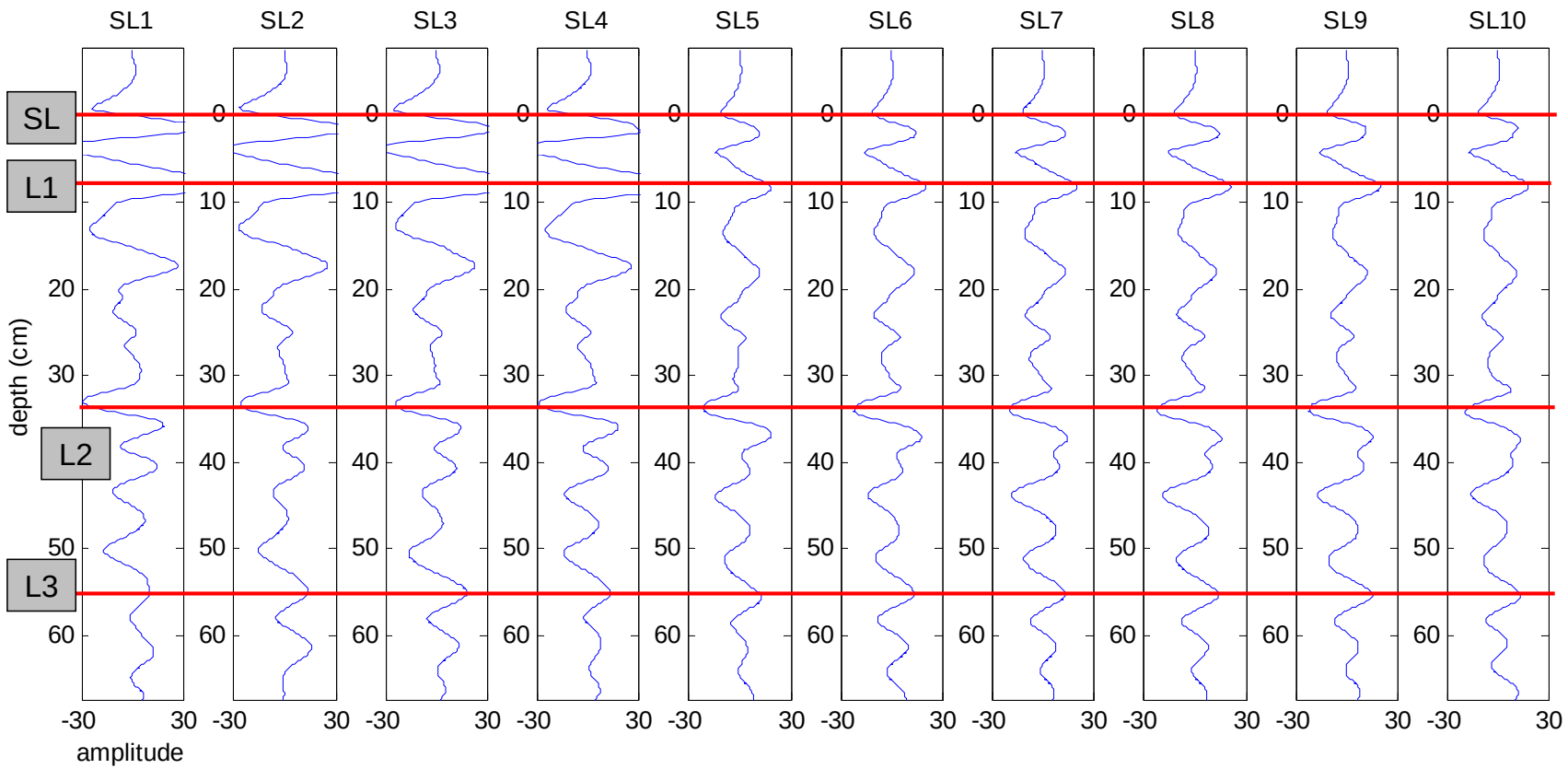

Figure 91. Constant reflected energy bands in depth for each of the Experiment III scan lines (SL1-SL10) calculated according to Eq. [F-1]. SL = air/surface coupling signal, L1 = soil layer boundary 1, L2 = soil layer boundary 2, and L3 = soil layer boundary 3.

References

Adetunji A.Q., Al-Shuhail A. and Korvin G. 2008. Mapping the internal structure of sand dunes with GPR: A case history from the jafurah sand sea of eastern saudi arabia. The Leading Edge 27:1446-1452.

Alliance for the Chesapeake Bay. 2004. Riparian forest buffers: Linking land and water. Chesapeake Bay Program, Annapolis, MD.

Allred B.J., Fausey N.R., Chi-Chih Chen and Peters L. 2004. GPR detection of drainage pipes in farmlands. Ground Penetrating Radar, 2004. GPR 2004. Proceedings of the Tenth International Conference on 1:307-310.

Al-Nuaimy W., Lu H. and Shihab S. 2002. Automatic target detection in GPR data. p. 139-140-143. *In* S. Koppenjan and L. Hua (eds.) Ninth international conference on G.P.R. S.Barbara, CA. May 2002.

Al-Nuaimy W., Shihab S. and Eriksen A. 2004. Data fusion for accurate characterisation of buried cylindrical objects using GPR. Proceedings of the Tenth International Conference on Ground Penetrating Radar 1:359-362.

Angier J.T. and McCarty G.W. 2008. Personal communication.

Angier J.T., McCarty G.W. and Prestegaard K.L. 2005. Hydrology of a first-order riparian zone and stream, mid-atlantic coastal plain, maryland. Journal of Hydrology 309:149-166.

Angier J.T., McCarty G.W., Rice C.P. and Bialek K. 2002. Influence of a riparian wetland on nitrate and herbicides exported from an agricultural field. J. Agric. Food Chem. 50:4424-4429.

Annan A.P. 2001. Ground penetrating radar workshop notes. Sensors & Software Inc., Mississauga, Ontario.

Barton C. and Montagu K. 2004. Detection of tree roots and determination of root diameters by ground penetrating radar under optimal conditions. Tree Physiology 24:1323-1331.

Bayani Cardenas M. and Zlotnik V.A. 2003. Three-dimensional model of modern channel bend deposits. Water Resour. Res. 39:1141.

Bohlke J.K., O'Connell M.E. and Prestegaard K.L. 2007. Ground water stratification and delivery of nitrate to an incised stream under varying flow conditions. J. Environ. Qual. 36:664-680.

Bowling J., Rodriguez A., Harry D. and Zheng C. 2005. Delineating alluvial aquifer heterogeneity using resistivity and GPR data. Ground Water 43:890-903.

Butnor J.R., Doolittle J.A., Kress L., Cohen S. and Johnsen K.H. 2001. Use of ground-penetrating radar to study tree roots in the southeastern united states. Tree Physiology 21:1269-1278.

Butnor J.R., Doolittle J.A., Johnsen K.H., Samuelson L., Stokes T. and Kress L. 2003. Utility of ground-penetrating radar as a root biomass survey tool in forest systems. Soil Sci Soc Am J 67:1607-1615.

Capineri L., Grande P. and Temple J.A.G. 1998. Advanced image-processing technique for real-time interpretation of ground-penetrating radar images. Intl. Journal of Imaging Systems and Technology 9:51-59.

Cermak J., Hruska J., Martinkova M. and Prax A. 2000. Urban tree root systems and their survival near houses analyzed using ground penetrating radar and sap flow techniques. Plant and Soil 219:103-116.

Conyers L.B. 2004. Ground-penetrating radar for archaeology. AltaMira Press, Walnut Creek, Calif.

Cox K.D., Scherm H. and Serman N. 2005. Ground-penetrating radar to detect and quantify residual root fragments following peach orchard clearing. HortTechnology 15:600-607.

Daniels D.J. 2004. Ground penetrating radar. Institution of Electrical Engineers, London.

Dannoura M., Hirano Y., Igarashi T., Ishii M., Aono K., Yamese K. and Kanazawa Y. 2008. Detection of crytomeria japonica roots with ground penetrating radar. Plant Biosystems 142:375-376-380.

Dell'Acqua A., Sarti A., Tubaro S. and Zanzi L. 2004. Detection of linear objects in GPR data. Signal Processing 84:785-786-799.

Department of Defense. 1989. Sampling procedures and tables for inspection by attributes. DoD, Washington, D.C.

Di Iorio A., Lasserre B., Scippa G.S. and Chiatante D. 2005. Root system architecture of quercus pubescens trees growing on different sloping conditions. Ann. Bot. (Lond) 95:351-361.

Dodge H.F. and Romig H.G. 1959. Sampling inspection tables. John Wiley, New York, NY.

Doolittle J.A., Jenkinson B., Hopkins D., Ulmer M. and Tuttle W. 2006. Hydropedological investigations with ground-penetrating radar (GPR): Estimating water-table depths and local ground-water flow pattern in areas of coarse-textured soils. Geoderma 131:317-318-329.

Germann P. and Beven K. 1981. Water flow in soil macropores III. A statistical approach. Eur. J. Soil Sci. 32:31-39.

Gish T.J., Gimenez D. and Rawls W.J. 1998. Impact of roots on ground water quality. Plant and Soil 200:47-54.

Gish T.J., Walthall C.L., Daughtry C.S.T. and Kung K.J.S. 2005. Using soil moisture and spatial yield patterns to identify subsurface flow pathways. Journal of Environmental Quality 34:274-286.

Gish T.J., Dulaney W.P., Kung K.J.S., Daughtry C.S.T., Doolittle J.A. and Miller P.T. 2002. Evaluating use of ground-penetrating radar for identifying subsurface flow pathways. Soil Sci Soc Am J 66:1620-1629.

Goldman A. and Cohen I. 2004. Anomaly detection based on an iterative local statistics approach. Signal Processing 84:1225-1226-1229.

Heeraman D.A., Hopmans J.W. and Clausnitzer V. 1997. Three dimensional imaging of plant roots in situ with X-ray computed tomography. Plant and Soil 189:167-179.

Herman H. and Singh S. 1995. First results in autonomous retrieval of buried objects. Automation in Construction 4:111-112-123.

Holden J. 2005. Piping and woody plants in peatlands: Cause or effect? Water Resources Research 41:1-10.

Holden J. and Burt T.P. 2002. Piping and pipeflow in a deep peat catchment. Catena 48:163-199.

Holden J., Burt T.P. and Vilas M. 2002. Application of ground-penetrating radar to the identification of subsurface piping in blanket peat. Earth Surface Processes and Landforms 27:235-249.

Hruska J. and Cermak J. 1999. Mapping tree root systems with ground-penetrating radar. Tree Physiology 19:125-130.

Kendall C. and McDonnell J.J. (eds.) 1998. Isotope tracers in catchment hydrology. 1.th ed. Elsevier, Amsterdam.

Kiley D. and Schneider R.L. 2005. Riparian roots through time, space and disturbance. Plant and Soil 269:259-260-272.

Kung K.S. and Lu Z. 1993. Using ground penetrating radar to detect layers with abrupt discontinuity in dielectric constant from their surroundings. Soil Science Society of America Journal 57:335-340.

Lawes J.B., Gilbert J.H. and Warington R. 1882. On the amount and composition of the rain and drainage waters collected at rothamsted. The Journal of the Royal Agricultural Society of England XVII:241-242-279.

Lin H.S., McInnes K.J., Wilding L.P. and Hallmark C.T. 1999. Effects of soil morphology on hydraulic properties: I. quantification of soil morphology. Soil Sci Soc Am J 63:948-954.

Lowrance R., Todd R., Fail J., Hendrickson O., Leonard R. and Asmussen L. 1984. Riparian forests as nutrient filters in agricultural watersheds. Bioscience 34:374.

Malik J., Belongie S., Leung T. and Shi J. 2001. Contour and texture analysis for image segmentation. International Journal of Computer Vision 43:7-8-27.

Martinez A., Kruger J.M. and Franseen E.K. 1998. Rep. 59. Kansas Geological Survey, Lawrence, KS.

Mayer P.M., Reynolds S.K., Jr., McCutchen M.D. and Canfield T.J. 2007. Meta-analysis of nitrogen removal in riparian buffers. J. Environ. Qual. 36:1172-1180.

Mitsch W. and Gosselink J. 2000. Wetlands. John Wiley & Sons, Inc., New York.

Morris C. and Mooney S.J. 2004. A high-resolution system for the quantification of preferential flow in undisturbed soil using observations of tracers. Geoderma 118:133-143.

Nagashima Y., Saito H., Kobayashi S. and Masuda J. 1995. Automatic recognition of hyperbolic patterns in underground cross-sectional images. p. 953-954-956. *In* Automatic recognition of hyperbolic patterns in underground cross-sectional images. Proc. of the symposium on the application of geophysics to engineering and environmental problems, Orlando, FL. 23-26 April 1995.

Naiman R.J. and Décamps H. 1997. The ecology of interfaces: Riparian zones. Annu. Rev. Ecol. Syst. 28:621-658.

Niltawach N., Higgins M., Johnson J.T., Chen C.C. and Baertlein B.A. 2002. GPR performance in the presence of buried biomass: Final report. The Ohio State University ElectroScience Laboratory, Columbus, OH.

Nobles M.M., Wilding L.P. and Mclnnes K.J. 2004. Pathways of dye tracer movement through structured soils on a macroscopic scale. Soil Sci. 169:229-242.

Noguchi S., Tsuboyama Y., Sidle R.C. and Hosoda I. 1999. Morphological characteristics of macropores and the distribution of preferential flow pathways in a forested slope segment. Soil Sci Soc Am J 63:1413-1423.

Olhoeft G.R. 1996. Applications of ground penetrating radar. p. 1-4. *In* Applications of ground penetrating radar. 6th international conference on ground penetrating radar, Sendai, Japan. Sept 30-Oct 3 1996.

Otsu N. 1979. A threshold selection method from gray-level histograms. IEEE Transactions on Systems, Man, and Cybernetics SMC-9:62-66.

Pal N.R. and Pal S.K. 1993. A review on image segmentation techniques. Pattern Recognition 26:1277-1294.

Park Y., Kim K., Cho S., Yoo D., Youn D. and Jeong Y. 2003. Development of a UWB GPR system for detecting small objects buried under ground. p. 384-388. *In* Development of a UWB GPR system for detecting small objects buried under ground. 2003.

Perret J., Prasher S.O., Kantzas A. and Langford C. 1999. Three-dimensional quantification of macropore networks in undisturbed soil cores. Soil Sci Soc Am J 63:1530-1543.

Peterjohn W.T. and Correll D.L. 1984. Nutrient dynamics in an agricultural watershed: Observations on the role of A riparian forest. Ecology 65:1466-1475.

Pierret A., Capowiez Y., Belzunces L. and Moran C.J. 2002a. 3D reconstruction and quantification of macropores using X-ray computed tomography and image analysis. Geoderma 106:247-248–271.

Pierret A., Capowiez Y., Belzunces L. and Moran C.J. 2002b. 3D reconstruction and quantification of macropores using X-ray computed tomography and image analysis. Geoderma 106:247-271.

Purbopuspito J. and Van Rees K.C.J. 2002. Root distribution at various distances from clove trees growing in indonesia. Plant and Soil 239:313-320.

Renz J. 2003. Scaling up, calculating, and comparing evapotranspiration rates of a mid-atlantic riparian wetland ecosystem. University of Maryland, College Park.

Shihab S., Al-Nuaimy W., Huang Y. and Eriksen A. 2003. A comparison of segmentation techniques for target extraction in ground penetrating radar data. p.

95-100. *In* A comparison of segmentation techniques for target extraction in ground penetrating radar data. Proceedings of the 2nd international workshop on advanced ground penetrating radar, Deflt, The Netherlands. 14-16 May 2003.

Shipitalo M., Nuutinen V. and Butt K. 2004. Interaction of earthworm burrows and cracks in a clayey, subsurface-drained, soil. Applied Soil Ecology 26:209-217.

Sidle R.C., Noguchi S., Tsuboyama Y. and Laursen K. 2001. A conceptual model of preferential flow systems in forested hillslopes: Evidence of self-organization. Hydrological Processes 15:1675-1692.

Sidle R.C., Tsuboyama Y., Noguchi S., Hosoda I., Fujieda M. and Shimizu T. 2000. Stormflow generation in steep forested headwaters: A linked hydrogeomorphic paradigm. Hydrological Processes 14:369-385.

Snowden P., Eamus D., Gibbons P., Khanna P., Keith H., Raison J. and Kirschbaum M. 2000. Synthesis of allometrics, review of root biomass and design of future woody biomass sampling strategies. Australian Greenhouse Office, Commonwealth of Australia.

Stewart J.B., Moran C.J. and Wood J.T. 1999. Macropore sheath: Quantification of plant root and soil macropore association. Plant and Soil 211:59-67.

Stokes A., Fourcaud T., Hruska J., Cermak J., Nadyezdhina N., Nadyezhdin V. and Praus L. 2002. An evaluation of different methods to investigate root system architecture of urban trees in situ: I. ground-penetrating radar. Journal of Arboriculture 28:2-10.

Stover D., Day F., Butnor J.R. and Drake B.G. 2007. Effect of elevated CO2 on coarse-root biomass in florida scrub detected by ground-penetrating radar. Ecology 88:1328-1334.

Sudmeyer R.A., Speijers J. and Nicholas B.D. 2004. Root distribution of pinus pinaster, P. radiate, eucalyptus globulus and E. kochii and associated soil chemistry in agricultural land adjacent to tree lines. Tree Physiology 24:1333-1346.

Svensson S. 2008. Aspects on the reverse fuzzy distance transform. Pattern Recognition Letters 29:888-896.

Szuch R.P., White J.G., Vepraskas M.J. and Doolittle J.A. 2006. Application of ground penetrating radar to aid restoration planning for a drained carolina bay. Wetlands : The Journal of the Society of the Wetland Scientists 26:205-216.

Terajima T., Sakamoto T. and Shirai T. 2000. Morphology, structure and flow phases in soil pipes developing in forested hillslopes underlain by a quaternary sand-

gravel formation, hokkaido, northern main island in japan. Hydrological Processes 14:713-726.

van Dam R.L., van den Berg E.H., van Heteren S., Kasse C., Kenter J.A.M. and Groen K. 2002. Influence of organic matter in soils on radar-wave reflection: Sedimentological implications. Journal of Sedimentary Research 72:341-352.

Vogel H.-. and Roth K. 2003. Moving through scales of flow and transport in soil. Journal of Hydrology 272:95-106.

Weiler M., Uchida T. and McDonnell J. 2003. Connectivity due to preferential flow controls water flow and solute transport at the hillslope scale. *In* Connectivity due to preferential flow controls water flow and solute transport at the hillslope scale. MODSIM, Townsville, Queensl., Australia. 2003.

Weiler M. 2005. An infiltration model based on flow variability in macropores: Development, sensitivity analysis and applications. Journal of Hydrology 310:294-315.

Weiler M. and Naef F. 2003. Simulating surface and subsurface initiation of macropore flow. Journal of Hydrology 273:139-154.

Wielopolski L., Hendrey G., Daniels J. and McGuigan M. 2002. Imaging tree root systems in situ. p. 58-59-62. *In* S. Koppenjan and L. Hua (eds.) Ninth international conference on G.P.R. S.Barbara, CA. May 2002.

Wynn T.M., Mostaghimi S., Burger J.A., Harpold A.A., Henderson M.B. and Henry L. 2004. Variation in root density along stream banks. J. Environ. Qual. 33:2030-2039.

Yang X.D. and Gupta V. 1993. An improved threshold selection method for image segmentation. p. 531-534. *In* An improved threshold selection method for image segmentation. 1993.

Youn H. and Chen C. 2002. Automatic G.P.R. target detection and clutter reduction using neural network. p. 58-59-62. *In* S. Koppenjan and L. Hua (eds.) Ninth international conference on G.P.R. S.Barbara, CA. May 2002.

Zarkhidze A. and Lemenager E. 2004. Case study - use of 3D GPR technologies for utility mapping in paris. Proceedings of the Tenth International Conference on Ground Penetrating Radar 1:375-378.